Fabrication of Josephson junctions using AFM Nanolithography

by

Akram Abdulasalam Elkaseh

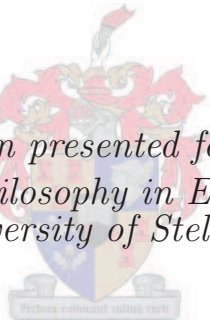

Dissertation presented for the degree of
Doctor of Philosophy in Engineering at the
University of Stellenbosch

Promoter: Prof W J Perold
Co-promoter: Prof V V Srinivasu

Faculty of Engineering
Department of Electrical and Electronic Engineering

December 2010

Declaration

By submitting this dissertation electronically, I declare that the entirety of the work contained therein is my own, original work, and that I have not previously in its entirety or in part submitted it for obtaining any qualification.

December 2010

Abstract

Planar weak link structures, such as micro-bridges, variable thickness bridges and nano-bridges, have always attracted a lot of attention. Their potential to behave as real Josephson elements make them useful devices, with numerous applications.

Powerful techniques, such as focused ion-beam and electron-beam lithography, were successfully used and are well understood in planar weak link structure fabrication. In this dissertation the results of an experimental study on planar weak link structures are presented. For the first time these structures have been successfully fabricated using AFM nanolithography on hard high-temperature superconducting YBCO tracks, where diamond coated silicon tips were used as a ploughing tool.

Superconducting YBCO thin films were deposited on different substrates, using inverted cylindrical magnetron sputtering. The films were used to fabricate micro-bridges, variable thickness bridges and nano-bridges, by using conventional photolithography, argon ion-beam milling and AFM nanolithography.

The measured I-V characteristics of the fabricated micro-bridges (width down to 1.9 μm), variable thickness bridges (thickness down to 15 nm) and nano-bridge (width down to 490 nm) showed well defined DC andAC Josephson effect characteristics.

For better understanding of the behaviour of these types of weak links, critical current versus temperature measurements, and magnetic field modulation of the critical current measurements, were also performed, with the results and discussions given inside the chapters.

The major challenges that were experienced in the laboratory during the fabrication processes and the operation of the fabricated devices are also discussed, with the solutions given where appropriate.

Opsomming

Swak-skakel vlakstrukture, soos mikrobrûe, brûe met veranderlike dikte en nanobrûe, het nog altyd baie aandag getrek. Hul het die potensiaal om soos werklike Josephson-elemente te kan funksioneer en is, as gevolg hiervan, nuttige toestelle met veelvuldige toepassings.

Kragtige tegnieke, soos gefokuste ioonstraal- en elektronstraal litografie, is suksesvol gebruik en word goed verstaan in die vervaardiging van swak-skakel vlakstrukture. In hierdie proefskrif word die resultate van 'n eksperimentele studie van swak-skakel vlakstrukture voorgelê.

Vir die eerste keer is hierdie strukture suksesvol vervaardig, deur gebruik te maak AFM nanolitografie op harde, hoë-temperatuur supergeleier YBCO (Yttrium Barium Koperoksied) spore, waar diamantbedekte silikonpunte gebruik is as ploeginstrument.

'n Dun lagie van supergeleidende YBCO is op verskillende substrate gedeponeer, deur gebruik te maak van omgekeerde silindriese magnetron verstuiwing. Die dun lagies is gebruik in die vervaardiging van mikrobrûe, brûe met veranderlike dikte en nanobrûe, deur die gebruik van gewone fotolitografie, argon-ioonstraal frees en AFM nanolitografie.

Die gemete I-V eienskappe van die vervaardigde mikrobrûe (met breedte so laag as 1.9 μm), veranderlike-dikte brûe (dikte tot 15 nm) en nanobrûe (breedte so min as 490 nm) toon goed gedefinieerde GS en WS eienskappe van die Josephson-effek.

Ten einde die gedrag van hierdie tipes swak-skakels beter te kan verstaan, is metings gedoen van kritieke stroom teenoor temperatuur, asook magnetiese veld modulasie van die kritieke stroom. Hierdie resultate en besprekings daarvan word binne die toepaslike hoofstukke aangebied.

Die grootste uitdagings wat in die laboratorium, sowel as met die toetsing van die vervaardigde toestelle ondervind is, word ook bespreek. Waar moontlik, word toepaslike oplossings voorgestel.

Acknowledgement

At the top of the list, I would like to express my deepest gratitude and appreciation to my supervisor, Professor W. J. Perold, for his supervision, guidance, suggestions, encouragement, and for being such a wonderful advisor. It was a privilege working with him. Equally important, I learned many important lessons from his extreme and unforgettable kindness.

I would also like to extend my thanks and appreciation to Professor V. V. Srinivasu for his conversations, as well as for his valuable advice. I had the privilege of getting a glimpse of his vast knowledge on many topics in superconductivity and physics.

I am indebted to many people at Stellenbosch University, who taught me many things throughout my studies. All the lecturers have contributed to help me learn the basic skills required to complete this dissertation.

I would like to thank Ulrich Büttner for his endless support. I could not have completed my research without his aid. Thanks for sharing your practical knowledge, creativity and encouragement, always smiling.

Many thanks go to my fellow colleagues, and especially Graham, for being so supportive and available to exchange problems and ideas.

Finally and foremost, I would like to give my special thanks to my parents, my wife, my brothers and sisters, whose relentless encouragement, moral support and understanding made this study possible.

Contents

List of Figures

List of Tables

Symbols and Abbreviations

Physical constants:

Planck's constant:	$h = 6.626 \times 10^{-34}$ J.s
Reduced Planck's constant:	$\hbar = \frac{h}{2\pi} = 1.055 \times 10^{-34} J.s$
Magnetic flux quantum:	$\Phi_0 = 2.07 \times 10^{-15}$ T.m^2
Boltzmann's constant:	$k_B = 1.381 \times 10^{-23}$ J.K^{-1}

Josephson junctions:

I-V	Current-voltage
φ	Gauge invariant phase difference
I_c	Critical current
R_n	Normal state resistance
$I_c R_n$	Characteristic voltage
V_g	Gap voltage

Abbreviations

AFM	Atomic force microscope
EBL	Electron beam lithography
FIB	Focused ion-beam
HTS	High-temperature superconductor
ICM	Inverted cylindrical magnetron
LTS	Low-temperature superconductor
RSFQ	Rapid single flux quantum
RSJ	Resistively shunted junction
SQUID	Superconducting quantum interference device
VTB	Variable thickness bridge
YBCO	Yttrium barium copper oxide ($YBa_2Cu_3O_{7-x}$)

Chapter 1

Introduction

1.1 Motivation

Since the theoretical prediction of the Josephson effect by Brian Josephson [6] and its first experimental observation by Anderson and Rowell [7] in the 60's, Josephson junctions have constantly received a lot of attention from both scientists and engineers, due to their fascinating properties and their potential use in a wide variety of scientific and commercial applications.

Josephson junctions form the basis for superconducting electronic circuits. Due to the extremely high switching speed of the junctions, and the very low power dissipation of the active elements, they can be used to make digital logic gates and devices much faster, smaller, and more efficient. Digital logic devices, such as Complementary Output Switching Logic (COSL) [8] and Rapid Single Flux Quantum (RSFQ) circuits [9], which have Josephson junctions as essential elements, are the fastest logic circuits on earth. RSFQ circuits have been reported to operate up to 770 GHz [10].

Sensitivity to magnetic fields is another important property of Josephson junctions, and it is utilised widely at present. Josephson junctions are used to make ultra-sensitive magnetometers, such as Superconducting Quantum Interference Devices (SQUIDs). SQUID magnetometers and gradiometers are the most sensitive devices to detect magnetic flux that are currently available. These devices have the ability to measure down to femtotesla (10^{-15} T) scale, which make them useful in physical, biological and medical applications.

The only obstacle preventing a wider commercial acceptance of Josephson junction technology is the cost, because junctions need to be cooled down to very low temperatures and need a suitable cryogenic environment for operation. Low temperature Josephson junctions, for example, usually operate at 4.2 K, and need liquid helium or an expensive cryocooler to reach the operating temperature.

However, since the discovery of high-temperature superconductors, superconductivity became a rapidly emerging technology, with application in numerous fields. It also stimulated intensive research on Josephson junction technology made from these materials. The discovery reduced the cost of cooling systems and simplified the Josephson junction testing setup. $YBCO$, the high-T_c superconductor used in this dissertation, becomes superconducting at 92 K, allowing the use of cheap liquid nitrogen to cool devices made from this material.

To date, several high-T_c junction topologies have been demonstrated, such as bi-crystal, step-edge, bi-epitaxial, ramp-edge, and obviously planar Josephson junctions, each with their own inherent production difficulties and performance limitations.

1.2 Project Aims and Objectives

The fabrication of a planar weak link, such as micro- and nano-bridges, are very attractive on both low-temperature superconductor- (LTS) and high-temperature superconductor (HTS) materials, and the Josephson effect has been demonstrated on these novel structures. Weak link planar bridges have many advantages, such as the flexibility to be fabricated at any place on the substrate, the low capacitance value of the bridge, and the small dimensions when compared with other types of weak links.

In order to fabricate bridges with micron- and nano-sized dimensions, suitable nanostructure techniques are needed. Bridges with dimensions down to a few nanometers were successfully fabricated and tested in many laboratories worldwide, using focused ion beam- (FIB) and electron beam lithography (EBL) techniques [11–13].

The aim of the work described in this dissertation is to use a novel Atomic Force Microscope (AFM) nanolithography technique to fabricate planar weak link structures, such as micro- and nano-bridges, on $YBCO$ as the HTS material, and to test these structures for true Josephson behaviour. Apart from the nanolithography challenges, successful fabrication of high-T_c Josephson junctions itself also presents severe challenges with regard to chemical processing and cryogenic cooling.

The use of AFM lithography is a promising tool for material structuring and patterning, with nanometer precision. The aim is to use diamond coated AFM tips as a cutting tool for HTS thin film materials. The loading force should be enough to scratch or remove the hard $YBCO$ layers. This technique was previously used to fabricate nano-plough junctions on aluminium, as well as to fabricate variable thickness bridges on MgB_2 [14; 15]. However, this technique has never been used on $YBCO$, as is envisaged in this dissertation.

The advantage of the AFM lithography technique, compared to FIB and EBL techniques is that its lower operating cost and the fact that it does not need extra multi-step processes. However, the drawbacks of the AFM technique are the wear and degradation of the tips after they have been used for some cycles, and the time required for the fabrication process

of multi-junctions.

The present work also involves exploration of several underlying processes, such as thin film deposition, photolithography and etching. Because the fabrication of HTS Josephson junctions is non-trivial, most of the practical challenges, and equipment problems that were encountered during the fabrication processes, will also be discussed in the dissertation.

1.3 Dissertation Overview

This dissertation is organised in the following manner:

- Chapter 2 introduces Josephson junctions and the Josephson effect. The most common and fascinating properties of the Josephson junction is also introduced.
- Chapter 3 provides a theoretical discussion of superconducting weak links. Weak links such as planar micro-bridges, variable thickness bridges and nano-bridges are presented in this chapter.
- Chapter 4 discusses the experimental methods used in this dissertation, including thin film deposition, photolithography and sample characterisation.
- Chapter 5 presents measured results of the fabricated high-temperature micro-bridge junctions. Measurements such as the observation of Shapiro-steps, and the effect of magnetic field on critical current, are presented here. The practical challenges inside the cleanroom are also discussed, as well as possible solutions.
- Chapter 6 presents measurements of the AC Josephson effect and the critical current behaviour of variable-thickness bridges made by AFM nanolithography in an applied magnetic field.
- Chapter 7 investigates the fabricated high-temperature nano-bridges. Measurements of the Josephson effect in these structures are presented.
- Chapter 8 provides a conclusive summary of this work, as well as a description of future work.

Chapter 2

Josephson Junctions

In this chapter the Josephson effect and the derivation of the Josephson relations are given. Basic lumped junctions, generalised Josephson junctions and the resistively shunted junction (RSJ) model are then discussed. The internal dynamics of Josephson junctions, such as Shapiro-steps and magnetic field modulation of the critical current, are then reviewed. The chapter ends with a brief overview of high-temperature Josephson junctions.

2.1 The Josephson Effect

If two metals are brought in close proximity, only separated by a small gap, quantum mechanics predict that the electrons can theoretically tunnel through the insulating layer. If a potential is applied across the gap, a current can thus flow from one metal to the other, even with the insulating layer between them.

Brian Josephson [6] used the same fundamentals to describe the quantum mechanical tunnelling of Cooper pairs between two superconductors. He predicted that it would be possible for Cooper pairs to tunnel through a thin insulating barrier placed between two superconductors. Cooper pairs consist of two electrons that pair together to form superelectrons. When all the electrons have formed Cooper pairs, they condense into the same quantum state. This quantum state can be described by a single macroscopic wave function, with a specific amplitude and phase.

An elegant derivation of the Josephson relations for an arbitrary location in the plane of the junction is given by Feynman [16]. Consider two equivalent superconductors, separated by a thin insulating barrier, as shown in Figure 2.1.

The time dependent coupled wave functions can be described by

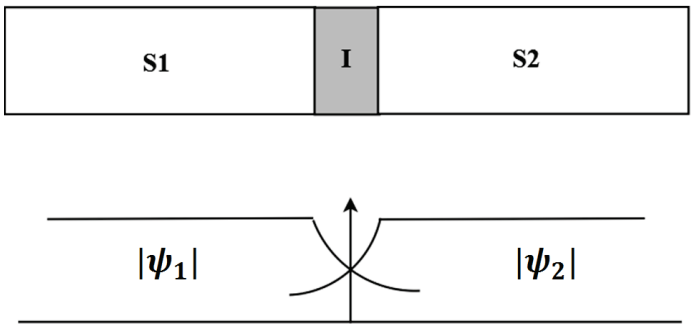

Figure 2.1: Two superconductors separated by a thin insulating barrier. The wave function represents the tunnelling of the Cooper pairs through the thin barrier.

$$i\hbar\frac{\partial\psi_1}{\partial t} = U_1\psi_1 + K\psi_2 \tag{2.1}$$

$$i\hbar\frac{\partial\psi_2}{\partial t} = U_2\psi_2 + K\psi_1 \tag{2.2}$$

where U_1 and U_2 represent the energies of the respective wave functions, $\hbar$ is the reduced Planck constant, and K is the coupling constant for the wave functions across the barrier.

Now, assume that a voltage bias is applied across the barrier such that $U_2 - U_1 = -2eV$. If the zero potential is assumed to occur in the middle of the barrier between the two superconductors, (2.1) and (2.2) become

$$i\hbar\frac{\partial\psi_1}{\partial t} = (-1eV)\psi_1 + K\psi_2 \tag{2.3}$$

$$i\hbar\frac{\partial\psi_2}{\partial t} = (1eV)\psi_2 + K\psi_1. \tag{2.4}$$

The wave functions of the individual superconductors can be expressed as

$$\psi_1 = \sqrt{n_1^*}e^{i\theta_1}, \psi_2 = \sqrt{n_2^*}e^{i\theta_2} \tag{2.5}$$

where n_1^* and n_2^* are the respective densities of Cooper pairs in the two superconductors. Substituting (2.5) into (2.3) and (2.4), letting $\varphi = \theta_2 - \theta_1$ for the gauge invariant phase difference, and separating real and imaginary parts, we get the following equations:

$$\frac{\partial n_1^*}{\partial t} = \frac{K}{\hbar}\sqrt{n_1^* n_2^*}\sin\varphi \tag{2.6}$$

$$\frac{\partial n_2^*}{\partial t} = -\frac{K}{\hbar}\sqrt{n_1^* n_2^*}\sin\varphi \tag{2.7}$$

$$\frac{\partial\theta_1}{\partial t} = -\frac{K}{\hbar}\sqrt{\frac{n_2^*}{n_1^*}}\cos\varphi + \frac{(1eV)}{\hbar} \tag{2.8}$$

$$\frac{\partial\theta_2}{\partial t} = -\frac{K}{\hbar}\sqrt{\frac{n_1^*}{n_2^*}}\cos\varphi - \frac{(1eV)}{\hbar}. \tag{2.9}$$

From (2.6) and (2.7), the supercurrent through the contact is proportional to $\frac{\partial n_1^*}{\partial t} = -\frac{\partial n_2^*}{\partial t}$, or

$$J = -2e\frac{\partial n_1^*}{\partial t} = \frac{2eK}{\hbar}\sqrt{n_1^* n_2^*}\sin\varphi = J_c\sin\varphi \tag{2.10}$$

where J_c is the maximum supercurrent density that the structure can sustain before entering the voltage state.

By subtracting (2.8) from (2.9) and setting $n_1^* = n_2^*$, the time evolution of the gauge invariant phase difference across the structure can be obtained as

$$\frac{\partial\varphi}{\partial t} = \frac{2e}{\hbar}V. \tag{2.11}$$

Equations (2.10) and (2.11) are called the Josephson relations and they are the basic equations for the tunnelling behaviour of Cooper pairs.

2.2 Basic Lumped Junctions

The structures in which Josephson effects can be observed are called Josephson junctions or weak links. The tunnel junction is the simplest example of a Josephson junction. The junction consists of two superconductors separated by a thin insulating layer (see Figure 2.2).

By assuming that the contact areas of the superconductors with the insulator are small enough, the gauge invariant phase difference and the current density across the contact areas can be considered to be uniform. Such a junction can be described as a basic lumped junction.

The behaviour of the basic lumped junction can be described by two mathematical relationships [17], the Josephson current-phase relationship

$$i = I_c\sin\varphi(t), \tag{2.12}$$

and the Josephson voltage-phase relationship

$$\frac{\partial \varphi}{\partial t} = \frac{2\pi}{\Phi_0} V, \tag{2.13}$$

where $\varphi(t)$ is the gauge invariant phase difference and, from (2.11), $\Phi_0 = \frac{h}{2e}$, the so-called fluxon. The gauge invariant phase difference is defined as

$$\varphi(t) = \theta_1(t) - \theta_2(t) - \frac{2\pi}{\Phi_0} \int_1^2 A(r,t) .dl. \tag{2.14}$$

The magnitude of the critical current, which can be derived from the microscopic theory [18], is given by

$$I_c = \frac{\pi \Delta(T)}{2eR_n} \tanh\left(\frac{\Delta(T)}{2k_B T}\right) \tag{2.15}$$

where k_B is the Boltzmann constant and R_n is the normal resistance of the junction.

At temperatures where $T \ll T_c$, (2.15) can be written as

$$I_c = \frac{\pi \Delta(0)}{2eR_n}. \tag{2.16}$$

The temperature dependence of the critical current I_c can be expressed as

$$I_c(T) = K\left(1 - \frac{T}{T_c}\right)^N \tag{2.17}$$

where K is a constant, and N is a fitting parameter which characterises the type of the weak link.

Figure 2.3 shows the symbol for a basic lumped Josephson junction, with the appropriate current and voltage sign conventions.

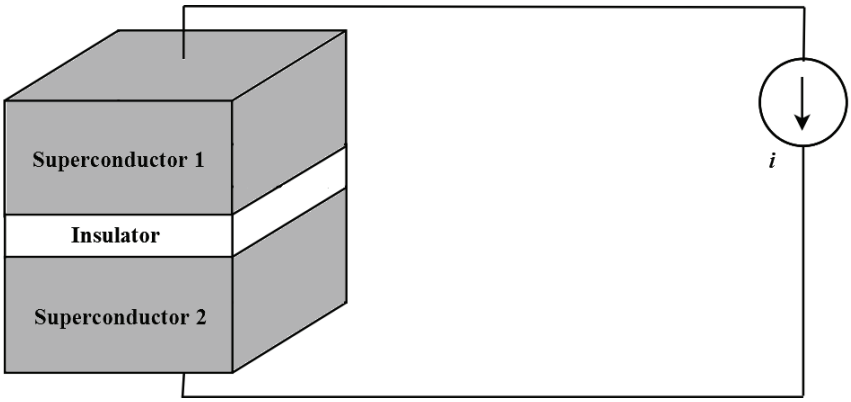

Figure 2.2: Tunnel junction driven by a current source.

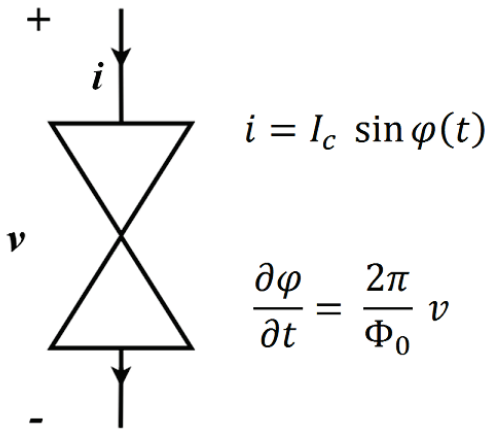

Figure 2.3: Symbol of a basic lumped junction.

2.3 Generalised Josephson Junctions

In a basic lumped junction the current through the junction is always restricted to be less than the critical current (I_c), the maximum current that the junction can support.

In cases where the current exceeds the critical current, the generalised Josephson junction model is used to provide a complete description of the Josephson junction's behaviour. Two additional parallel channels are added to the basic lumped junction, namely a resistive and a capacitive channel.

According to the two-fluid model, normal electrons will exist in a superconductor at temperatures above T=0 K. Some of these normal electrons will tunnel through the barrier so that resistive behaviour is apparent, even at voltages less than the gap voltage $V_g = 2\Delta/e$, where 2Δ is the energy required to break up Cooper pairs. This voltage dependent conductance channel can be generalised to give

$$G(v) = \begin{cases} \frac{1}{R_{sg}(T)} & \text{if } |v| < 2\Delta(T)/e \\ \frac{1}{R_n} & \text{Otherwise} \end{cases} \tag{2.18}$$

where R_{sg} is known as the subgap resistance, and a function of temperature as well. Above the gap voltage all the Cooper pairs become unbounded single electrons and a normal resistance (R_n) is observed due to the tunnelling of normal electrons through the barrier across the junction.

The junction capacitance is in essence a parallel plate capacitor. The insulator is considered as ideal with a permittivity ϵ, cross section A, and thickness d. The value of the junction capacitance is thus given by

$$C = \frac{\epsilon A}{d}. \tag{2.19}$$

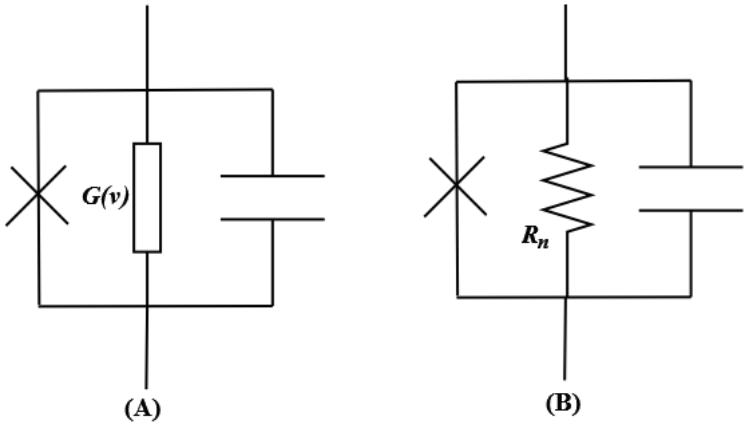

Figure 2.4: Generalised Josephson junction models. (a) NRSJ model and (b) RSJ model.

The mentioned model is called the non-linear resistively shunted junction (NRSJ) model. To simplify the model, the non-linear conductance can be replaced by a constant resistance R_n. The simplified model is called the resistively shunted junction (RSJ) model. The RSJ model is widely used to analyse Josephson junction characteristics. Figure 2.4 gives a graphical representation of the NRSJ- and RSJ model.

2.4 The Resistively Shunted Junction (RSJ) Model

The resistively shunted junction model is the most widely used model to study the dynamics of practical Josephson junctions. The model was first introduced by McCumber [19] and Stewart [20].

If a *DC* current is applied, using the model shown in Figure 2.4(b), the applied driving current can be written as the sum of the current in each branch. The applied current can thus be expressed as

$$i = I_c \sin\varphi + \frac{v}{R_n} + C\frac{dv}{dt}. \tag{2.20}$$

The voltage across the model is the same voltage as in (2.13), and by substitution of (2.13) into (2.20), one can obtain the second order differential equation

$$i = I_c \sin\varphi + \frac{1}{R_n}\frac{\Phi_0}{2\pi}\frac{d\varphi}{dt} + C\frac{\Phi_0}{2\pi}\frac{d^2\varphi}{dt^2}. \tag{2.21}$$

This current equation can no longer be solved analytically. However, it can be written as a dimensionless equation

$$\frac{i}{I_c} = \sin\varphi + \frac{d\varphi}{d\tau'} + \beta_c \frac{d^2\varphi}{d(\tau')^2} \tag{2.22}$$

where

$$\tau' = \frac{t}{\tau_J}, \tau_J = \frac{\Phi_0}{2\pi}\frac{1}{I_c R_n} \tag{2.23}$$

and

$$\beta_c = \frac{R_n C}{\tau_J} = \frac{2\pi I_c R_n^2 C}{\Phi_0}. \tag{2.24}$$

The parameter β_c is known as the Stewart-McCumber parameter. It is the ratio of the two characteristic time constants of the system, i.e. the RC time constant and the time constant associated with the dynamics of the Josephson junction itself. The Stewart-McCumber parameter is a measure of the influence of the junction capacitance.

When $\beta_c \ll 1$, the capacitance of the junction is negligible, and the model is considered to be a parallel connection of a basic lumped Josephson junction and a resistor.

The average voltage across the junction can be written as

$$\langle v(t)\rangle = iR\sqrt{1-(\frac{I_c}{i})^2} \qquad \text{for } i \geq I_c. \tag{2.25}$$

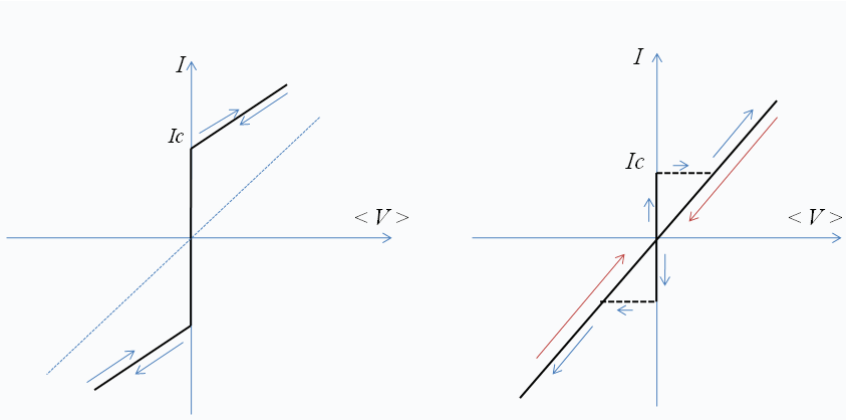

Figure 2.5: Typical I-V curve for (a) an overdamped junction ($\beta_c \ll 1$) and (b) a lightly damped junction ($\beta_c \approx 1$).

When the shunt capacitance is negligible ($\beta_c \ll 1$), and the applied current exceeds the critical current I_c, part of the current is shunted through the resistive channel, which generates a voltage, causing the current to oscillate at the Josephson frequency. The IV characteristic

is non-hysteretic, as is shown in Figure 2.5(a). Junctions with $\beta_c \ll 1$ are referred to as *overdamped*.

When $\beta_c \gg 1$, the capacitance of the junction is not negligible and plays a part in the dynamics of the Josephson junction. When the applied current is increased from zero to I_c, it flows through the junction and no voltage will be created across it. When the current exceeds the critical current I_c, a finite voltage will appear across the junction, as part of the current goes through the resistive channel, while the shunt capacitance is also being charged. However, if the current is decreased below the critical current there is still some charge stored in the capacitive channel, and the junction will stay in a finite voltage state for longer. The IV characteristic becomes hysteretic, as is shown in Figure 2.5(b). Junctions with $\beta_c \gg 1$ are referred to as *underdamped*.

2.5 Shapiro Steps

Josephson junctions respond to high frequency radiation in an interesting way. Let us assume a Josephson junction with negligible capacitance ($\beta_c \ll 1$), and defined by the RSJ model.

Assume that an RF voltage source is applied across the mentioned Josephson junction, and that the applied voltage is given by

$$V(t) = V_0 + V_s cos(\omega_s t). \tag{2.26}$$

If the resistive part of the model is ignored, the current through the junction can be written as

$$\begin{aligned} I &= I_c sin\left(\frac{2e}{\hbar}\int V dt + \varphi_0\right) \\ &= I_c sin\left(\frac{2e}{\hbar}\int_0^t (V_0 + V_s cos\omega_s t)dt + \varphi_0\right) \\ &= I_c sin\left[\frac{2e}{\hbar}V_0 t + \frac{2eV_s}{\hbar\omega_s} sin\omega_s t + \varphi_0\right]. \end{aligned} \tag{2.27}$$

It can be shown [21] that the current $I(t)$ through the Josephson junction can be written as an infinite series of products of Bessel functions (J_n) and sine waves,

$$I(t) = I_c \sum_{n=-\infty}^{n=+\infty} (-1)^n J_n\left(\frac{2eV_s}{\hbar\omega_s}\right) sin\left[(\omega_J - n\omega_s)t + \varphi(0)\right], \tag{2.28}$$

where $\omega_J = 2eV/\hbar$, the Josephson oscillation frequency.

Since the IV characteristic is drawn for the average current, $I \approx \langle I(t) \rangle$, and since the sine term averages to zero unless $\omega_J = n\omega_s$, there are spikes appearing on the slope of the resistive channel in the IV curve for all voltages equal to

$$V_n = n\left(\frac{\hbar\omega_s}{2e}\right). \tag{2.29}$$

The IV characteristics for this case is shown in Figure 2.6 on the left hand side.

However, if the junction is driven by an RF current source similar to the voltage source that was defined in (2.26), the IV characteristics will follow a staircase pattern, as is shown in Figure 2.6, on the right.

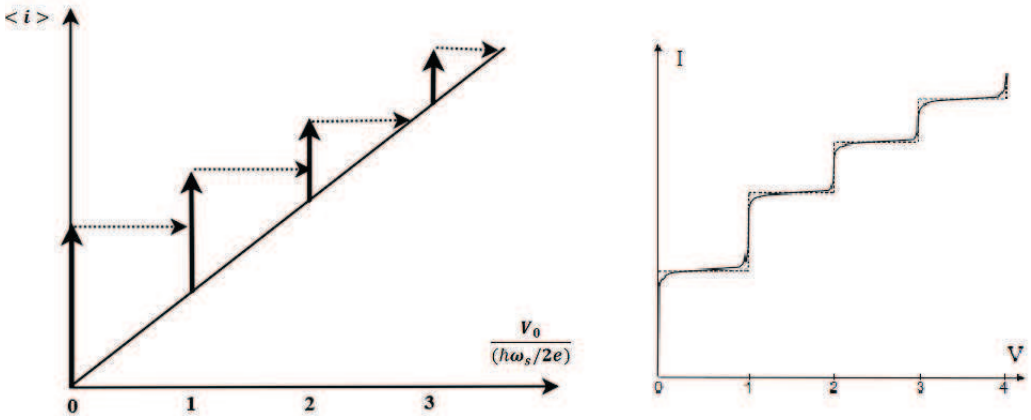

Figure 2.6: Left: IV characteristics for a Josephson junction driven by an RF voltage source. Right: Typical Shapiro steps for a Josephson junction driven by an RF current source.

This phenomenon is known as Shapiro steps, as it was measured for the first time by Shapiro in 1964 [22]. The presence of Shapiro steps in IV characteristics is widely used as a verification of the Josephson effect.

2.6 Magnetic Field Effects on Josephson Junctions

It is important to understand what the effect of an applied magnetic field threading a Josephson junction will have on the characteristic behaviour of such a junction. The sensitivity of a Josephson junction to externally applied magnetic fields is also important to gain insight into the behaviour of SQUID magnetometers.

An externally applied magnetic field causes the critical current of the Josephson junction to modulate. In a short Josephson junction, where the magnetic field created by the current

flowing through the junction is negligible, the phase difference between the superconducting electrodes is uniform and the current is uniformly distributed across its width at zero applied field.

However, as soon as a magnetic field is applied, this is no longer the case. The magnetic field now penetrates the barrier and also a distance, known as the Josephson penetration depth, into the respective superconducting electrodes. The phase difference thus varies with distance along the junction. The supercurrent is also no longer uniform, but it is spatially modulated across the junction's width.

Now, consider the effect of a magnetic field applied to the junction along the y-direction, as is shown in Figure 2.7. The two superconductors L and R are separated by a thin insulating barrier of thickness t.

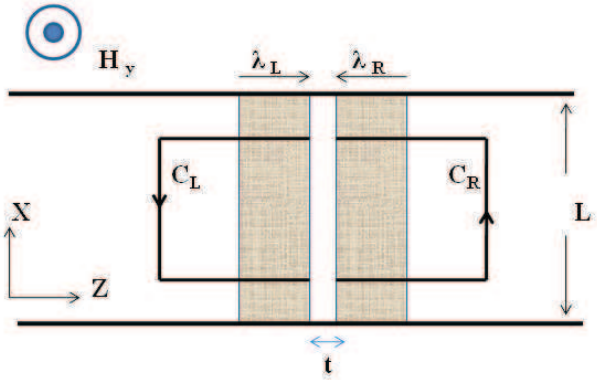

Figure 2.7: Path of integration around a junction with a small barrier, to determine the phase difference across the junction.

The applied magnetic field penetrates the superconductors with a distance λ_L and λ_R, respectively. The phase difference can now be calculated [17] as

$$\frac{d\varphi}{dx} = \frac{2e}{\hbar}(\lambda_L + \lambda_R + t)H_y. \tag{2.30}$$

By integrating (2.30) and substitution of the result into (2.10), the dependency of the supercurrent density on the applied magnetic field is obtained as

$$J = J_c \sin\left(\frac{2e}{\hbar} d H_y x + \varphi_0\right), \tag{2.31}$$

where $d = (\lambda_L + \lambda_R + t)$ is the magnetic penetration. The critical current I_c at any given value of the applied magnetic field can be found by integration of (2.31) with respect to x, which yields

$$I_c(\Phi) = I_c(0)\left|\frac{\sin(\pi\frac{\Phi}{\Phi_0})}{\pi\frac{\Phi}{\Phi_0}}\right|, \tag{2.32}$$

where $\Phi = HLd$ and $\Phi_0 = h/2e$, the flux quantum (2.07×10^{-15} Wb). As can be seen, the critical current I_c varies as a sinc-function modulus, which is often referred to as a Fraunhofer-like diffraction pattern. A plot of the function is shown in Figure 2.8. It is clear that minima of I_c occur where an integer number of flux quanta are introduced into the junction barrier.

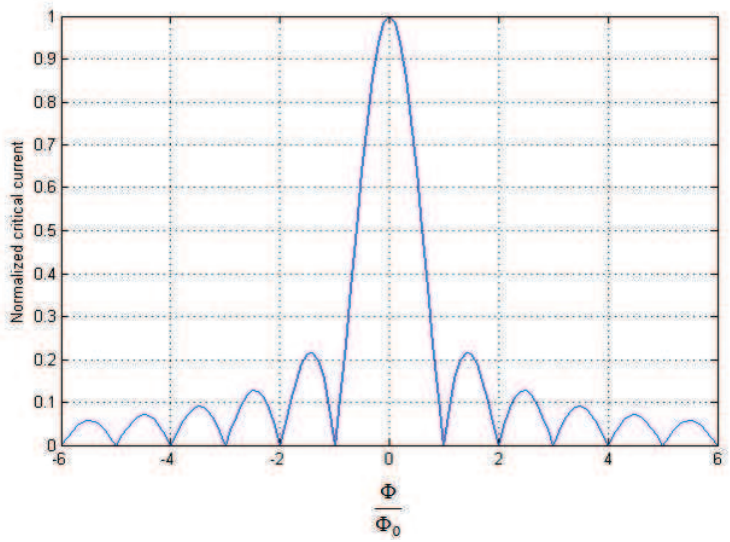

Figure 2.8: Maximum zero-voltage current as a function of the magnetic flux.

For the analysis above, it was assumed that the Josephson junction was short. Such a junction has uniform current distribution, since self-induced magnetic fields can be neglected.

However, for a long junction, the field produced by the junction's own current cannot be neglected. The critical current is no longer proportional to the junction area, as current flow becomes confined to the edges of the junction. At a given value of applied magnetic field, there may be several possible solutions for the critical current, corresponding to different numbers of flux vortices trapped in the junction. This leads to a triangular $I_c(\Phi)$ pattern, with incomplete suppression of the critical current at the minima and also an irregular period.

The length scale over which the two classes of junctions can be identified is the temperature dependent Josephson penetration depth, λ_J, defined by

$$\lambda_J = \sqrt{\frac{\Phi_0}{2\pi\mu_0 J_c(2\lambda + d)}}, \tag{2.33}$$

where d is the thickness of the insulating barrier, J_c is the critical current density and Φ_0 the magnetic flux quantum. More details can be found in [5].

2.7 Thermal Fluctuation Effect on Current-Voltage Curve

Thermal fluctuations can diffuse the coupling of the phases of the wave functions across a junction, and hence, the IV curve can strongly deviate from the classical IV characteristic. Thermal fluctuations result in a rounding of the IV characteristic, as well as a suppression and eventually an elimination of hysteresis in underdamped Josephson junctions [23].

Ambergaokar and Halperin [1] addressed the effect of thermal noise on the DC Josephson effect. They found that, below the critical current, there is always a finite resistance, due to the thermally activated phase difference changes of the wave functions. They included a thermal noise current as an additional term in the RSJ equation (2.20). The noise-rounded IV curve can be expressed as

$$v = 2(1-x^2)^{1/2} exp\left\{-\gamma\left[(1-x^2)^{1/2} + x\sin^{-1}x\right]\right\}\sinh(\frac{\pi\gamma x}{2}), \tag{2.34}$$

where $x = i/I_c(T)$, $x \ll 1$, $v = V/I_c R_n$, and γ is a dimensionless parameter, defined by

$$\gamma = \frac{\hbar I_c(T)}{ekT}. \tag{2.35}$$

Figure 2.9 shows the simulated IV characteristics of a Josephson junction in the presence of thermal fluctuations, using Ambergaokar and Halperin's analysis.

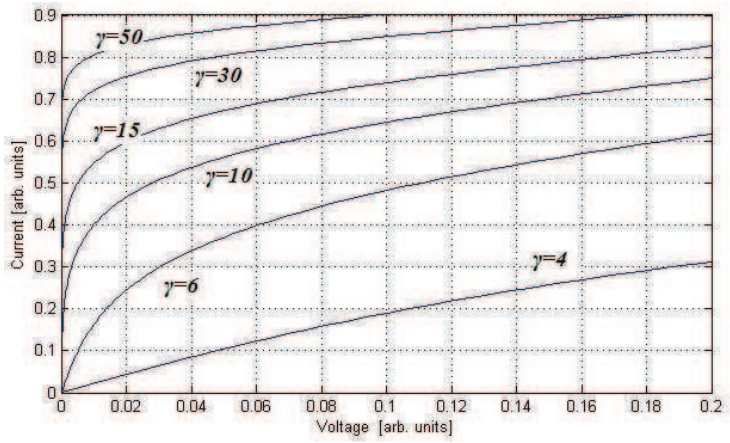

Figure 2.9: Simulated IV characteristics, using Ambergaokar and Halperin's analysis [1].

In high-speed superconducting electronic circuits, such as Rapid Single Flux Quantum (RSFQ) logic circuits, thermal fluctuations can cause spontaneous switching of junctions, introducing unwanted switching errors. In pulse jitter, for instance, fluctuations cause uncertainty in the arrival time of data pulses [24].

2.8 High-Temperature Josephson Junctions

The fabrication of low-temperature superconductor Josephson junctions, with properties such as non-hysteretic IV characteristics, high I_cR_n-products, controllable and reproducible parameters (I_c, R_n, C) and high stability is a relatively simple task. Unfortunately, this is not true for high-temperature superconductors (HTS). The preparation of SIS tunnel junctions in HTS is extremely difficult. The preparation is complicated by the requirement of a full epitaxial layer structure, the short coherence length of the Cooper pairs, and the sensitivity of the HTS to structural and chemical changes (surface instability).

Basically there are two kinds of natural Josephson junctions that manifest in high-temperature superconductors, namely intrinsic Josephson junctions and grain boundary junctions. Intrinsic Josephson junctions occur naturally between successive CuO_2 layers. They have been observed in both single crystals and thin films of highly anisotropic materials. Grain boundary junctions occur when two adjacent grains are not perfectly aligned [25].

There are various types of HTS Josephson junctions that can be fabricated by using artificial grain boundaries. Figure 2.10 illustrates some of the HTS Josephson junction options. Below is a brief description of the most popular HTS Josephson junction topologies:

- *Natural Grain Boundary Junctions:* The earliest natural grain boundary junctions were produced by fabricating a thin section on a superconductor polycrystalline film. The thin section is on one or more naturally occurring grain boundaries. These grains are randomly orientated and meet at grain boundaries with varying misorientation angles, as illustrated in Figure 2.10(a). It is possible to use natural grain boundary (NGB) junctions in RF SQUIDs, because only one junction is required. The fabrication of NGB DC SQUIDs, however, has not been very reproducible, because the characteristics of NGB junctions vary from one grain boundary to the other [26].

- *Bi-crystal Junctions:* Bi-crystal grain boundary junctions (Figure 2.10(b)) are fabricated by growing an epitaxial HTS film on a bi-crystal substrate. The bi-crystal substrate is made by gluing two single-crystal substrates, with different grain orientations, together. A grain boundary forms accordingly in the HTS film at the interface. The critical current density decreases sharply across the interface. This exponential degradation of the critical current is a function of the misalignment angle between the two substrates [25].

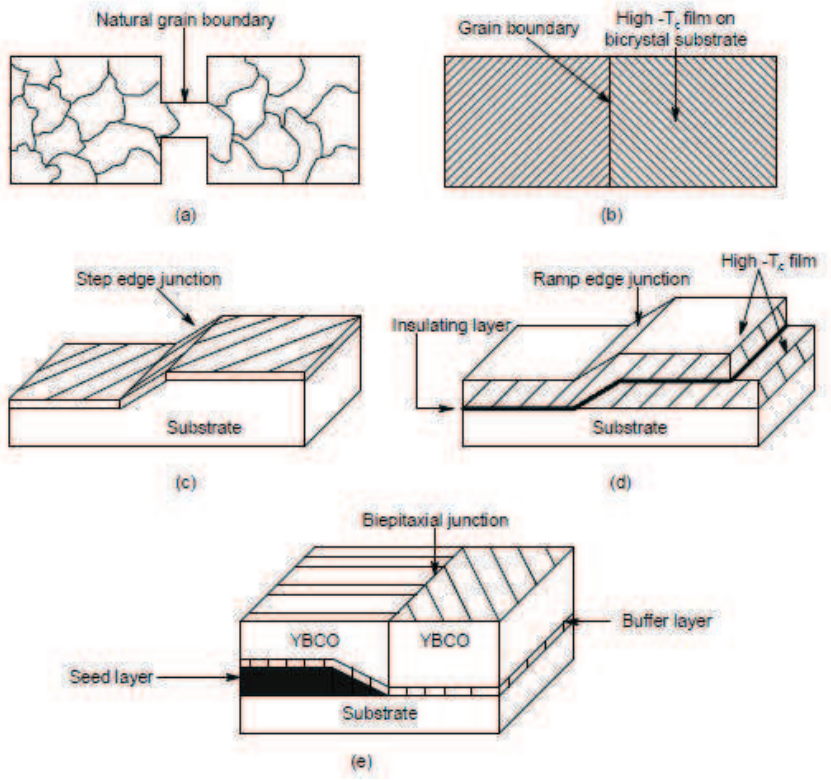

Figure 2.10: Various types of high-temperature Josephson junctions. (a) Natural grain boundary, (b) bi-crystal junction, (c) step-edge junction, (d) multilayer ramp-edge junction and (e) bi-epitaxial junction.

- *Step-edge Junctions:* Figure 2.10(c) shows an HTS step-edge junction. The idea was first proposed by Daly *et al* [27]. The junction is formed by growing a thin HTS epitaxial film on a substrate with a step. A sharp step on a single-crystal substrate is created by photolithography or electron-beam lithography and ion-beam milling. The transport properties of a junction greatly dependent on the film thickness and the step profile, such as height, step angle and the sharpness of the corners [28]. Step-edge junctions can be manufactured on a variety of large-area substrates and junctions can be placed anywhere on the substrate. These junctions, however, are more complicated to manufacture than their bi-crystal counterparts.

- *Ramp-edge junctions:* These junctions are fabricated in a multi-layer process. An HTS layer is deposited onto a substrate, and then a ramp-edge is created on this layer by using lithography and an etching process. A thin insulating layer and a second thin HTS layer are then deposited on the ramp-edge. These junctions are the most promising for HTS digital circuits, because the multi-layer process makes it easy to introduce a ground plane. A ramp-edge junction is shown in Figure 2.10(d).

- *Bi-epitaxial grain boundary junctions:* This type of junction is illustrated in Figure

2.10(e). A thin $'seedlayer'$ is deposited over a part of the substrate to produce a new surface, with a different growth pattern. The subsequently deposited epitaxial buffer layers, as well as the epitaxial HTS thin film, grow with different orientations, separated by a grain boundary with a specific angle [29].

- *Electron-beam junctions:* These junctions are produced by suppressing superconducting properties in a narrow region. Different sources of irradiation have been used, such as ion- and electron beams. Irradiation causes damage to CuO-planes and introduces oxygen defects, which lower the critical temperature. The irradiation region acts as a barrier.

Gross *et al* [25] classified HTS Josephson junctions into three basic categories:

- *Junctions with intrinsic interfaces, which are naturally formed.* Bi-epitaxial-, step-edge- and bi-crystal grain boundary junctions all fall in this class.
- *Junctions with extrinsic interfaces.* These junctions are formed where two superconducting electrodes are separated by an artificial layer. This layer can be an insulator (I), a semiconductor (Se), a normal metal (N), or another superconductor with a different critical temperature ($S^{'}$).
- *Junctions without an interface.* These junctions are created by weakened superconductive structures. Constriction type junctions, such as micro-bridges are examples. The weak coupling is achieved by degrading the superconducting properties with focused electron- or ion-beam irradiation.

2.9 Summary

This chapter provided a simple framework for the analysis of Josephson junctions. The RSJ model was introduced and used to give insight into the I-V characteristics of Josephson junctions. Next, the behaviour of Josephson junctions, when irradiated with magnetic fields at microwave frequencies, were discussed. The chapter ended with an overview of the popular HTS Josephson junction geometries and their general properties.

Chapter 3

Superconducting Weak Links

In this chapter Josephson effects in superconducting weak link structures are introduced. Planar HTS bridges such as micro-brides, variable thickness bridges and nano-bridges are also discussed in detail, including the theory behind the structures' behaviour and the techniques used to fabricate these novel structures.

3.1 Introduction

In Chapter 2 Brian Josephson's predictions about the existence of two fascinating effects were discussed. The first was that a tunnel junction should be able to sustain a supercurrent without the application of a voltage. The second effect was that, if the supercurrent exceeds its critical value, the junction will start to generate electromagnetic waves. Both effects were soon verified experimentally [30; 31] and are currently well established phenomena in superconducting tunnel junctions.

In fact, these Josephson effects are not limited to classical tunnel junctions alone. They can take place in any kind of inhomogeneous structure where the superconductivity is suppressed [32]. Different superconducting structures, called weak links, exhibit similar Josephson effects when the dimensions of such weak links are sufficiently small. Numerous ways of structuring such weak links have been explored for both low-temperature superconductors (LTS) and high-temperature superconductors (HTS).

The term *weak link* describes the conducting junction between two superconducting electrodes. The critical current through the junction is less than in the electrode itself [33]. The classical tunnel junction is limited to SIS structures, but weak links are found in a variety of weakly coupled superconducting structures, such as SNS junctions, micro-bridges, variable thickness bridges, ion-implanted bridges and point contacts, as illustrated in Figure 3.1. The main advantage of these structures over tunnel junctions is that the junction capacitance is

significantly lower [32].

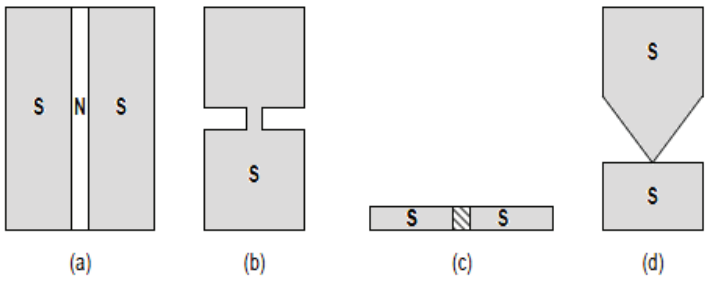

Figure 3.1: Different types of structures where the Josephson effect can be observed. (*a*) SNS junction, (*b*) micro-bridge, (*c*) ion-implanted bridge, and (*d*) point contact.

In 1964 the Josephson effect was observed in weak link structures by several researchers. The use of weak link structures for practical purposes, however, only began in 1966.

In Figure 3.1(a) a thin layer of a normal metal, that is placed between two superconducting electrodes, is shown. Such a structure is called an *SNS sandwich* junction.

When a normal metal and a superconducting metal are brought into good electrical contact, some Cooper pairs will penetrate into the normal metal from the superconductor side, causing a finite supercurrent to flow through such a junction. This is known as the *proximity effect*. The same effect will be observed if the normal layer is replaced by a semiconductor or another superconductor.

Various semiconducting materials have been employed as a barrier. The critical current in SSeS junctions is much higher than in SIS junctions. Nevertheless, the performance and applications of semiconducting barrier junctions are limited due to the occurrence of a few problems, such as interdiffusion at the barrier boundaries, the amorphous polycrystalline structure, the presence of pinholes, and the low normal resistance [5].

The micro-bridge shown in Figure 3.1(b) is created by narrowing a small section in a continuous superconducting strip. This small section reduces the critical current of the superconducting strip, such that the critical current at that point is much smaller than it is in the superconducting strip itself, thereby causing the superconductor to convert into a normal conductive state in the constriction [33].

A structure that closely resembles the sandwich structure is the ion-implanted bridge, shown in Figure 3.1(c). A section with a low critical current is created in a narrow strip of superconducting film by implantation of ions into that region. The damaged area can either be created on a substrate before the deposition of the superconducting film [34], or by implementing the damage straight onto the superconducting region [35].

A more complicated weak link geometry is the point contact junction, shown in Figure 3.1(d). The electrical contact is created by two weakly touching superconductive electrodes. When

pressure is applied to the electrodes, the oxide layer is interrupted at many places, thereby forming several metallic connections between the electrodes. The significant disadvantage of the point contact junction lies in its poorly defined geometry and its irreproducibility [32].

3.2 Planar Josephson Micro-Bridges

The micro-bridge is one of most successful low temperature superconducting structures where the Josephson effect has been demonstrated. The bridge was first investigated by Anderson and Dayem in 1964 [36]. The planar structure is a single thin superconducting film into which large superconducting electrodes are linked by a narrow constriction bridge. Josephson effects are demonstrated in a micro-bridge whenever the maximum dimensions of the bridge are smaller than, or comparable to, the temperature dependent coherence length of the superconductive material $\xi(T)$.

In their *AL theory* Aslamazov and Larkin [37] proposed the basic principles of the existence of the Josephson effect in structures such as micro-bridges. They explained the weak link behaviour in micro-bridges, using the Ginzburg-Landau (GL) theory, from which the relationship between the current density and phase difference across the weak link was derived.

Consider a superconductor with the geometry displayed in Figure 3.2. The constricted region has the length l, which is much smaller than the coherence length ξ [17].

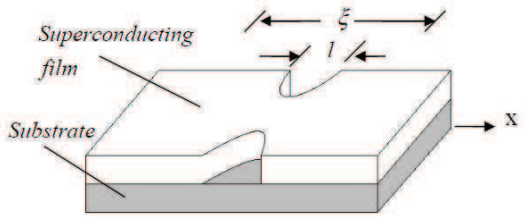

Figure 3.2: Superconducting thin film with a narrow constricted micro-bridge.

In the absence of an external magnetic field, the first Ginzburg-Landau equation for such a bridge can be written in the form

$$\xi^2 \nabla^2 \mathcal{F} + \mathcal{F} - \mathcal{F} |\mathcal{F}|^2 = 0, \tag{3.1}$$

where $\mathcal{F}$ is a dimensionless order parameter.

The order parameter in a short bridge varies substantially over the length of the bridge. Thus, $\nabla^2 \mathcal{F}$ can be estimated as $\nabla^2 \mathcal{F} \sim \mathcal{F}/l^2$. On the other hand, the amplitude of the order parameter is $|\mathcal{F}| \sim 1$.

Therefore, the dominant term in (3.1) is the derivative term, since $\xi^2/l^2 \gg 1$, while all other terms are of the order 1. Hence, (3.1) can be simplified to

$$\xi^2 \nabla^2 \mathcal{F} = 0. \tag{3.2}$$

Far from the constricted region the order parameter can be assumed to be constant and we thus have that

$$\mathcal{F}(r) = \begin{cases} |\mathcal{F}_1| e^{i\theta_1} & \text{as } x \to -\infty \\ |\mathcal{F}_2| e^{i\theta_2} & \text{as } x \to +\infty. \end{cases} \tag{3.3}$$

The other boundary condition on $\mathcal{F}(r)$ is that the normal component of the current density must be zero at the surface of the micro-bridge. The boundary condition will thus be satisfied if $n.\nabla\mathcal{F} = 0$, where n is a unit vector normal to the surface.

From GL theory, the supercurrent equation is given by [17]

$$J_s = -\frac{\Phi_0}{2\pi\Lambda} Re \left\{ \frac{1}{i} \mathcal{F} * \nabla\mathcal{F} \right\}, \tag{3.4}$$

where *Lambda* is London coefficient. Aslamazov and Larkin proposed a unique expression, which can be written in the form

$$\mathcal{F}(r) = |\mathcal{F}_1| e^{i\theta_1} \mathcal{G}(r) + |\mathcal{F}_2| e^{i\theta_2} [1 - \mathcal{G}(r)], \tag{3.5}$$

where $\mathcal{G}(r)$ is a real function of the coordinates satisfying the boundary value problem $\nabla^2 \mathcal{G}(r) = 0$, $n.\nabla\mathcal{G} = 0$, and

$$\mathcal{G}(r) = \begin{cases} 1 & \text{as } x \to -\infty \\ 0 & \text{as } x \to +\infty. \end{cases} \tag{3.6}$$

Using (3.5), the supercurrent through the micro-bridge (3.4) can be calculated to be

$$J_s = J_c(r) \sin(\theta_1 - \theta_2), \tag{3.7}$$

where

$$J_c = \frac{\Phi_0 |\mathcal{F}_1| |\mathcal{F}_2|}{2\pi\Lambda} \nabla\mathcal{G}. \tag{3.8}$$

The supercurrent expression has the same form as the one for the classical Josephson effect. The total current is proportional to $\sin(\theta_1 - \theta_2)$, which shows that the micro-bridge will

exhibit the Josephson effect if the order parameter is made to change over a distance similar to the coherence length.

For the case where the dimensions of a bridge are much larger than the coherence length, the AL theory is patently inapplicable. However, that does not mean that such bridges will not exhibit the Josephson effect.

The coherence length in cuprate high-temperature superconducting materials is very short. Therefore, fabrication of micro-bridges with dimensions smaller than the coherence length is an impossible task. Nevertheless, micro-bridges have been fabricated on these materials that have exhibited well defined Josephson effects.

Some of the techniques that are used to fabricate planar micro-bridge structures on HTS superconductors are listed below:

- *Standard photolithography:* Dayem-bridges were fabricated on YBCO thin films using photolithography, followed by a razor cutting technique [38], chemical wet etching [39], dry etching [40], and lift-off [41]. The widths of the junctions varied from 1 μm to 100 μm. These junctions have demonstrated the Josephson effect, and devices based on these micro-bridges, such as SQUID magnetometers, were fabricated successfully [42; 43].

- *Laser-beam ablation:* This maskless process is used for patterning micro-bridges on YBCO thin films [44]. Well defined microwave-induced Josephson effects in 1 μm YBCO Dayem-bridges have been demonstrated [45]. The authors used a pulsed Xe laser to pattern the small bridge structures. Büttner *et al* [46] have used a laser writing system to reduce the width of the YBCO lines. Precision control of the laser spot size allowed them to fabricate micro-bridges with widths smaller than 1 μm.

- *Ion- and electron-beam irradiation:* Josephson junctions were successfully fabricated by using a focused ion-beam technique, changing the width of striplines on superconducting thin films [47]. Different types of charged particles have been used for processing, such as oxygen- and argon ions, as well as neutrons. The junction properties depend on the amount of damage caused by the irradiation of the ion-beam [48]. Kahlmann [49] used an oxygen ion-implantation into an YBCO thin film to form a weak link. The behaviour of the structure had a strong dependency on the implantation dose.
  Electron-beams are also used to produce planar Josephson junctions on HTS thin films. A focused electron-beam writing method was used by many authors to produce HTS Josephson junctions [50]. Typically the constricted region of the micro-bridge is exposed to a focused electron-beam with a spot size of 2 nm, from a high field-emission source. The surface damage alters the superconductive properties of the material under the spot [51].

Another way to fabricate planar micro-bridges is by the deposition of HTS thin films on mechanically and chemically polished substrates [52], which will lead to the formation of

high-angle tilt boundaries (HATB), causing weak links to form. The cracks that were caused by the c-axis shrinkage associated with the tetragonal-to-orthorombic phase transition during the cooling process [53], can be used as Josephson elements.

Josephson effects have been demonstrated in HTS micro-bridge structures for a long time. The main reasons for the behaviour are listed below:

- Natural grain boundaries in HTS superconductors can behave like Josephson junctions [26]. Micro-bridge type Josephson junctions may have one or a few grain boundaries in the bridge regions, which act as Josephson elements.
- Some HTS micro-bridges exhibit the Josephson effect due to localisation and disordering effects. HTS superconducting properties are very sensitive to defects [54]. Irradiation, for instance, causes displacement defects, which act as scattering centres in Cu-O planes and are primarily chain or plane oxygen displacements. Decreasing the carrier concentration, which is done by removing or displacing chain oxygen decreases the doping level, which lowers the critical temperature [55]. The degree of the damage and the suppression of superconducting properties due to irradiation depend on the energy and the fluence of the irradiation beam used. The properties of the irradiated area varies from normal metal characteristics to superconductive.
- Likharev [56] conducted a theoretical study on superconducting bridges. He showed that Josephson effects in the bridges can also occur when the bridge lengths are greater than the coherence length. He attributed that to the existence of coherence motion of Abrikosov vortices in the bridges. Another study by Aslamazov and Larkin [57] showed that, in wide bridges ($a \gg \xi$), Josephson behaviour occured due to the periodic motion of quantum vortices at the narrowest point of the bridge. More details on vortice motion in bridges will be discussed in Section 3.4.

3.3 Variable Thickness Bridges

A variable-thickness bridge (VTB) consists of a thin, narrow link joining two much thicker bulk films. VTB bridges can be realised by reduction of the film thickness in the link region, or by both a thickness and width constriction. These bridges were first discussed in 1971 and experimentally tested in 1973 [32]. Figure 3.3 shows possible geometries for VTB bridge-type junctions.

The bridge region in the VTB structure can either be a normal metal (SNS link) or a superconducting metal (SS'S link), with a critical temperature smaller than the critical temperature of the electrodes.

Numerous groups have shown that VTB structures, made from either LTS or HTS superconductors, exhibit the Josephson effect. The current-phase difference relationship is attributed to the formation and coherent motion of vortices in a direction perpendicular to the trans-

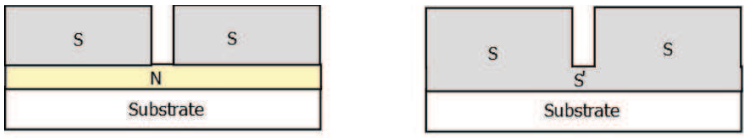

Figure 3.3: Schematic view of a VTB geometry: (a) SNS-type junction, and (b) SS'S-type junction.

port current in the superconducting bridges [58; 59]. However, it can also be caused by proximity effects in coplanar structures (Figure 3.3(a)).

There are many techniques and materials reported for the fabrication of VTB bridges, of which most have been successfully used in high-frequency applications and devices.

Yeh and Buhrman [60] investigated superconducting lead VTB structures. They fabricated the bridges by using a glass fiber, 0.5-1 μm in diameter, which served as the mask for the gap between the two electrodes. Bridge thicknesses ranged from 60 nm to 100 nm, and the electrode thicknesses from 200 nm to 500 nm.

Wolf *et al* [61] used niobium VTB bridges in a weak link granular thin film SQUID. Photolithography and ion-milling were used to sculpture a 20-40 μm wide bridge into the film. A short section of the bridge was then thinned by anodisation.

A group of researchers [62] have used an electron-beam lithography technique to form an indium VTB structure. The weak link region thickness was 50 nm, while the thickness of the electrodes was 700 nm. The bridges were tested for the microwave power spectra, and the results were found to be in good agreement with the RSJ model.

Bouchiat *et al* [63] presented a method for the fabrication of Josephson junctions and SQUIDs from niobium. The method was based on the oxidation of a niobium layer under the voltage-biased tip of an Atomic Force Microscope (AFM). Bridges with sizes comparable to the coherence length have been fabricated.

Hahn *et al* [64] obtained niobium VTB bridges by a mechanical surface modification technique, using a Scanning Force Microscope (SFM) with a diamond probe tip. By moving the diamond tip with a correct loading force and speed over the stripline, about 70-80% of the material was removed, leaving a very thin VTB structure.

AFM nanolithography is also used for VTB bridge preparation. Gregor *et al* [15] prepared VTB bridges on MgB_2 by AFM nanolithography. They scratched the surface and reduced the thickness of the bridge by applying a strong loading force on the tip. Two years later [65], with almost the same group, they prepared an RF SQUID based on VTB bridges, using the same scratching technique on the photoresist.

VTB bridges, and devices based on them, have been successfully fabricated on YBCO material by different techniques, such as aluminium slant evaporation and argon ion-beam etching [66], focused ion-beam [67], aqueous etchants such as ethylenediaminetetraacetic

acid (EDTA) and nitric acid, and non-aqueous etchants such as bromide in isopropyl [68].

The properties of coplanar junctions in the VTB geometry, made of bilayer structures, were investigated by Barholz [69]. YBCO layers act as the superconducting electrodes, and the barrier materials were semiconducting, like PBCO or superconducting oxide such as YPrBaCuO. Small trenches, with sizes from 30-70 nm, in YBCO micro-bridges were fabricated by ion-beam milling.

3.4 Weak Links in Nano-Bridges

Superconducting thin film nano-bridges have shown the Josephson effect, caused by periodic vortex motion across the bridge when the width and length are less than a few times the coherence length [56]. However, they also show Josephson behaviour when the size of the bridge is smaller than, or comparable to, the effective London penetration length λ_{eff} [57; 70], given by

$$\lambda_{eff} = \lambda_L \coth(d/2\lambda_L) \approx 2\lambda/d, \tag{3.9}$$

where d is the thickness of the film.

In a magnetic field between the lower critical magnetic field H_{c1} and the upper critical magnetic field H_{c2}, the magnetic flux is able to penetrate the superconductor in the form of tubes, called *vortices*. Abrikosov [71] observed the vortices for the first time in 1957. Each vortex has a normal core with a radius equal to the coherence length ξ.

The magnetic field inside the superconductor is strong at the normal core of the vortices, and decreases in an approximately exponential manner as one moves away from the core. The value of the flux in each vortex was experimentally found to be a single flux quantum.

The vortex is held in place in the superconductor by a pinning force F_P. However, when a transport current J_{TR} is present, the Lorentz force $J_{TR} \times \Phi_0 > F_P$ acts to unpin the vortex and induces the core of the vortex to move [17].

Vortices can enter the nano-bridges either from externally applied magnetic fields, or from a transport current passing through the bridge. The order parameter of the superconductor, along the vortex axis, is zero. The order parameter increases until it reaches its maximum value at a distance comparable to the coherent length ($\sim \xi$) and thus will form a normal core region of the size of the coherent length radius. Formation of Abrikosov vortices, with normal core regions acting like weak links, could show Josephson effects.

The forces acting on the vortices in a nano-bridge are schematically illustrated in Figure 3.4. A transport current passing through the bridge will induce a magnetic field across it. Two vortices with opposite orientation will be created simultaneously at the edge of the bridge. The pinning force F_{pin} at the edges will act on the vortices. When the transport current is

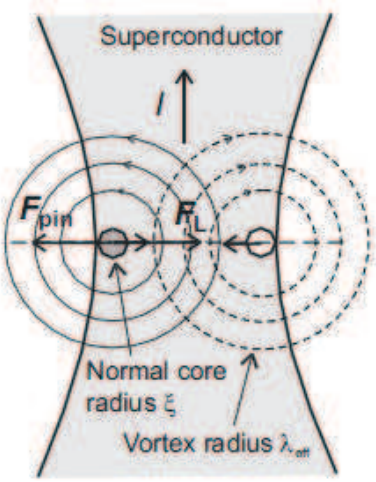

Figure 3.4: Forces acting on two Abrikosov vortices in a superconducting thin film nano-bridge.

increased, the Lorentz force F_L acting on the vortex will overcome this pinning force. If the transport current density exceeds the critical current density of the bridge, these vortex-antivortex pairs will move perpendicular to the direction of the driving current, towards the centre of the bridge, where they finally annihilate [72].

Abrikosov vortex motion can be coherent due to the strong interaction between the vortices, causing periodical oscillations in the electrical and magnetic field emitted by the bridge. Several publications on low-temperature superconductor (LTS) SQUIDs, based on nano-bridges were published [73; 74]. Nano-bridges have also been used in high-temperature superconductor devices, such as superconducting flux-flow transistors [75], and SQUIDs. D. H. Blank *et al* were the first to demonstrated HTS SQUIDs based on nano-bridges [76].

Novel techniques, such as focused ion-beam [11], electron-beam lithography [13], and nano-ploughing using AFM [14], are successfully utilised to fabricate weak links, such as micro-bridges, VTB, and nano-bridge structures.

3.5 Summary

This chapter discussed the Josephson effects in superconducting weak links. A literature overview on superconducting weak link structures such as microbridges, variable-thickness bridges and nanobridges was introduced. Some of well known techniques which used to fabricate these weak link structures were also highlighted.

In this dissertation, however, the very interesting and promising AFM nanolithography method will be used to fabricate the mentioned weak link structures. It will be shown how to scratch and modify the YBCO thin films to form the bridges.

Chapter 4

Experimental Methods

In this chapter the YBCO crystal structure, thin film growth synthesis and film deposition is discussed, as well as the lithography and milling that is required to form micro-scale geometries. This is followed by details of thin film characterisation techniques, such as X-ray diffraction and AFM. The chapter ends with a study of AFM nanolithography, the method that will be used in this dissertation to create planar devices.

4.1 Crystal Structure of YBCO

The discovery of superconductivity in a layered copper oxide (cuprate) in 1986 was revolutionary, not only because of the record transition temperatures (T_c) at that time, but also because these materials are poor conductors in the normal state. Indeed, the parent compounds of superconducting cuprates are antiferromagnetic Mott insulators.

Cuprates are variants of the crystal type known as *perovskites*. Perovskites are minerals whose chemical formula is ABX_3 or AB_2X_3. Thus, perovskites contain three elements A, B, X in the proportion 1:1:3 or 1:2:3.

The simplest copper oxide perovskites are insulators. In order to become superconducting they have to be doped by charge carriers. The effect of the doping has the most profound influence on the superconducting properties of the cuprates.

All cuprate superconductors are layered perovskites containing CuO_2 layers, alternated by intermediate building blocks. In general, they are basically tetragonal, and they have one or more CuO_2 planes. Superconductivity in cuprates occur in the copper oxide planes. The CuO_2 layers are always separated by layers of other atoms such as Bi, O, Y, Ba, La, etc., which provide the charge carriers in the CuO_2 planes. These layers are called *charge reservoirs* [77].

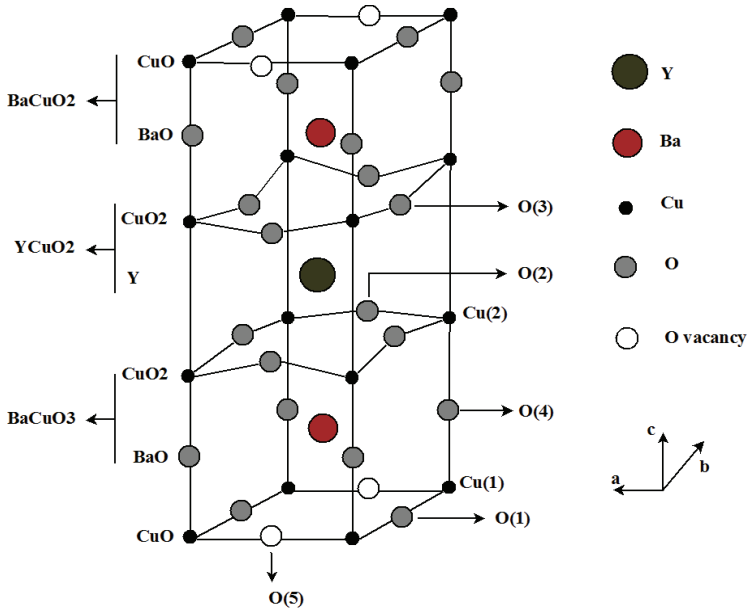

Figure 4.1: A unit cell of YBCO

The compound $YBa_2Cu_3O_{7-x}$ (YBCO) is the most known example of high-T_c superconductors. It was first discovered by Wu *et al* in 1987 [78]. The crystal structure of YBCO consists of three perovskite units $BaCuO_3$, $YCuO_2$ and $BaCuO_2$, stacked on top of each other.

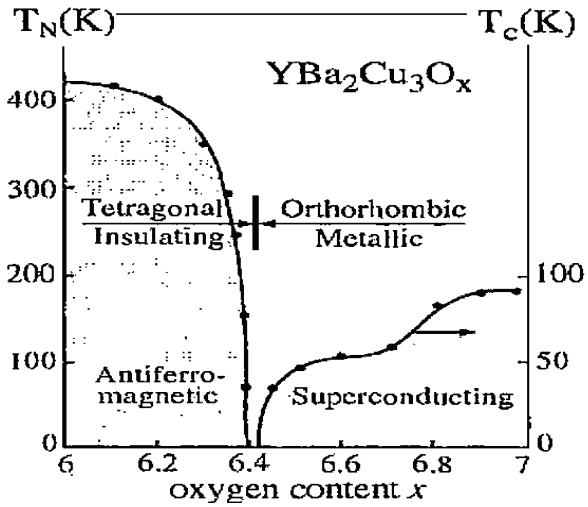

Figure 4.2: The oxygen doping phase diagram for YBCO [2]

The unit cell of YBCO is shown in Figure 4.1. The lattice constants of the orthorhombic crystal structure are $a = 3.83\mathring{A}$, $b = 3.88\mathring{A}$ and $c = 11.68\mathring{A}$. The central Y atom is

sandwiched between two CuO_2 planes. These planes are separated from the top and bottom CuO basal layers by a BaO block.

The Cu atoms in the basal layers are called Cu(1), while the Cu in the CuO_2 layers is labeled Cu(2). The oxygen atoms in the CuO_2 planes are referred to as O(2) and O(3), whereas the O atoms in the BaO layer are denoted as O(4). Two positions O(1) along the b-axis and O(5) along the a-axis are known in the basal CuO plane. In the orthorhombic phase, O(5) is destroyed and oxygen atoms are located in the O(1) positions. Thus, the basal layers have a partial filling with oxygen and the total number of O atoms in a unit cell varies from 6 to 7. For $YBa_2Cu_3O_6$, the basal planes contain no O atoms and the structure is called tetragonal.

The crystal structure and the lattice constants change with the oxygen deficiency x, as well as the superconducting critical temperature (see Figure 4.2). The oxygen content can be systematically changed from x=1 to zero, resulting in a change from an antiferromagnetic insulator to an underdoped superconductor at x=0.7. Optimally doped superconducting $YBa_2Cu_3O_{7-x}$ is orthorhombic and has a critical temperature $T_c \approx 93$ K, with $x \approx 0.03$.

4.2 Thin Film Growth

Epitaxial HTS thin films have attracted the attention of researchers and engineers, due to their often superior properties over polycrystalline thin films. Electronic devices based on epitaxial thin films have shown better performance and extended life than those based on polycrystalline films.

Formation of a thin film takes place via nucleation and growth processes. The general picture of the step-by-step growth process can be presented as follows [79]:

- The unit species, on impacting the substrate, lose their velocity component and are physically adsorbed on the substrate surface.
- The adsorbed species are not in thermal equilibrium with the substrate and move over the substrate surface. They interact among themselves, resulting in the formation of bigger clusters.
- The clusters are thermodynamically unstable, and they start growing in size. After reaching a certain critical size, the cluster becomes stable. This step is called the *nucleation stage*.
- The nucleation density and the average nucleus size depend on a number of parameters, such as the energy of the impinging species, thermal diffusion, the temperature, topography and the chemical nature of the substrate. A nucleus can grow parallel to the substrate by surface diffusion of the adsorbed species, and also perpendicular to it by direct impingement of the incident species. At this stage, the rate of the parallel

growth is much higher than the perpendicular growth. The grown clusters are called *islands*.

- The small islands start coalescing with each other in an attempt to reduce the substrate surface area. This is called the *coalescence stage*. The formation of bigger islands is enhanced by increasing the surface mobility of the adsorbed species, by, for example, increasing the substrate temperature.
- Larger islands grow together, leaving channels and holes of uncovered substrate. The structure of the films at this stage changes from a discontinuous island type to a porous network type. Filling of the channels and holes forms a completely continuous film.

In general, epitaxial growth can be the result of any of the following three modes of growth, namely layer-by-layer (Frank van der Merwe) growth, island growth (Volmer-Weber) and mixed growth (Stranski-Krastanov) [80].

Usually the highest crystalline quality thin film is obtained in the layer-by-layer growth mode. Film atoms are more strongly bound to the substrate than to each other. This growth mode is schematically illustrated in Figure 4.3(a).

Substrates are not atomically flat. Substrate surfaces have steps, kinks and other kinds of defects, which are preferred sites for nucleation. One of the layer-by-layer growth mechanisms, known as step-flow growth, occurs when the surface migration length, λ, of an atom is greater than the length of the terraces formed by the step-edges on the substrate, l. Step-flow growth occurs due to the attachment of the atoms to the edges of the terraces on the substrate.

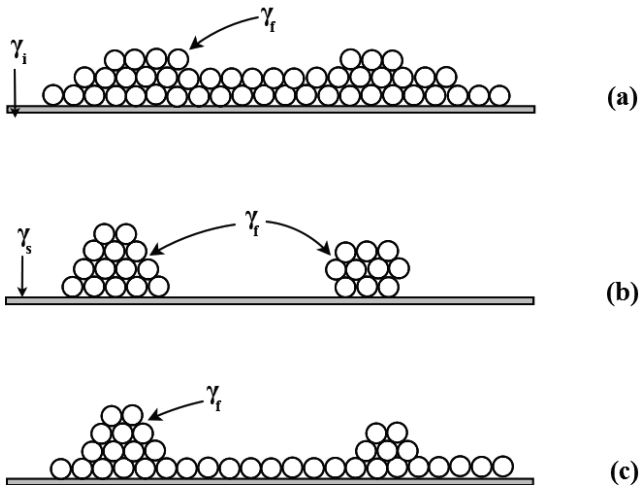

Figure 4.3: Film growth modes: (a) Layer-by-layer (Frank van der Merwe), (b) Island (Volmer-Weber), and (c) Mixed (Stranski-Krastanov).

Island growth can be observed by the formation of three-dimensional islands. This growth

mode is schematically shown in Figure 4.3(b). The reason for such a type of growth is that the film atoms are more strongly bound to each other, than to the substrate. However, the slow atom diffusion on the substrate surface during thin film growth helps to form this growth mode [81].

In mixed growth, shown in Figure 4.3(c), the growth first proceeds in a layer-by-layer fashion, and at a certain thickness changes to island formation due to changes in the surface energies.

In heteroepitaxial growth, the lattice parameters of the film and the substrate are not the same, resulting in a strained film. The strain energy will increase as the film thickness increases, and at a certain point it will become favourable to introduce defects in the film. The defects can be either dislocations, twin domains, surface roughness or a combination of them, and will finally result in the formation of islands [82].

The growth stage of thin films is governed by the surface energy of the films, γ_f, the surface energy of the substrate,γ_s, and the interfacial energy between thin film and substrate,γ_i. Layer-by-layer growth will be predominant at $\gamma_i+\gamma_f \leq \gamma_s$, and island growth at $\gamma_i+\gamma_f > \gamma_s$.

4.3 Substrates for YBCO Thin Films

Substrate choice is essential for the production of good quality thin film electronic devices.

For epitaxial growth, the substrate should be single crystalline without inhomogeneities and with atomic smoothness over large distances. Additionally, the lattice parameters of the substrate must be matched or close to those of YBCO. To maintain the lattice match, the thermal expansion coefficients of substrate and YBCO must be comparable over a wide temperature range, to avoid loss of adhesion or film cracking during thermal cycling.

Chemical compatibility between YBCO and the substrate is important and there should not be any chemical reactions between the two. Chemical reactions will result in a deviation from the desired phase growth [83]. In addition, adhesion of YBCO thin films to a substrate is strongly dependent on the chemical nature, cleanliness and the microscopic topography of the substrate surface.

Many materials have been used as substrates for HTS thin films. Some of these materials have a perovskite crystal structure, while others have a non-perovskite oxide structure.

Perovskite substrates are most suitable for high quality epitaxial HTS thin films. They have good lattice matching with YBCO due to the similarity in the crystal structure. However, perovskite substrates are quite expensive and relatively scarce. In addition, their high dielectric constant makes some of them unsuitable substrate materials for high frequency applications.

Considerable research has been devoted to YBCO thin film deposition on conventional crystalline (non-perovskite) substrate materials, like MgO and ZrO_2 (YSZ). Although the

lattice mismatch of these materials is worse than the perovskite substrates, YBCO thin films can successfully be deposited on them. Nonetheless, YBCO thin films on MgO have a consistently reduced critical temperature T_c and critical current density, when compared to the optimum values obtained on perovskite substrates.

The properties of common substrate materials used for YBCO thin film deposition are listed in Table 4-I.

Table 4-I: Substrates used for the growth of epitaxial YBCO thin films.

Substrate	**$SrTiO_3$**	**$LaAlO_3$**	**MgO**	**Al_2O_3**	**YSZ**	**CeO_2**
Dielectric constant (ϵ)	277	23	9.65	9.34	25	17
tan δ	6×10^{-2}	3×10^{-5}	5×10^{-4}	3×10^{-5}	8×10^{-3}	5×10^{-4}
Lattice mismatch %	2	3	9	11.2	5.8	4.9

4.4 Thin Film Growth Techniques

There are two categories of growth techniques, namely *in-situ* and *ex-situ* film growth. Both are used to deposit thin films of HTS materials on a wide variety of substrates. *In-situ* thin films are superconductive when they are removed from the growth chamber. On the other hand, *ex-situ* films are amorphous and non-superconductive after growth, and they need additional post-anneal treatment in an oxygen rich environment to become superconductive. In both categories, high-vacuum deposition systems are required.

Numerous film deposition techniques have been investigated for the epitaxial growth of HTS films. Almost all of the deposition techniques can be broadly divided into two categories:

1. *Physical Vapour Deposition (PVD) Techniques*: These techniques are atomistic deposition processes, in which material is vaporised from a solid or liquid source in the form of atoms or molecules, transported through a vacuum or low pressure gaseous environment to the substrate, where it condenses. PVD techniques include some high-energy ion- or electron bombardment of the target to release the material for deposition onto the substrate. Techniques such as co-evaporation, molecular beam epitaxy (MBE), pulsed laser deposition (PLD) and sputtering fall under this category, as is shown in Figure 4.4.

2. *Chemical Vapour Deposition (CVD)*: CVD entails the deposition of atoms by the high-temperature reduction or decomposition of a chemical vapour of molecules, which contain the material to be deposited, in a reactor. CVD includes metal-organic decomposition (MOD), metal-organic chemical vapour deposition (MOCVD) and liquid phase epitaxy (LPE).

Two popular methods of thin film growth that have been applied to HTS materials, and especially YBCO, are PLD and sputtering. High quality superconducting thin films, with

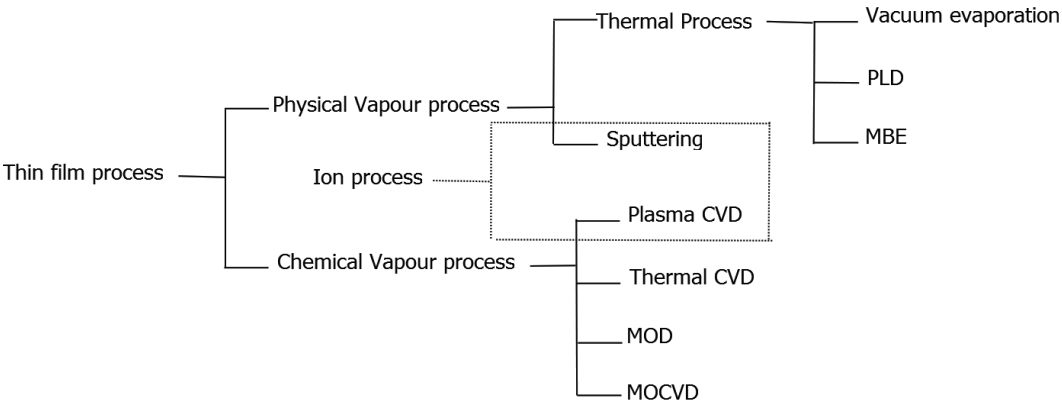

Figure 4.4: Thin film deposition processes.

atomic thickness control, can be achieved. A DC Inverted Cylindrical Magnetron (ICM) sputtering technique was used throughout to deposit the YBCO thin films that were used in this dissertation.

4.4.1 Inverted Cylindrical Magnetron Sputtering

One of the methods that is successfully applied to produce HTS thin films, is sputter deposition. It allows for the production of stoichiometric films over a large area.

In a sputter deposition process, the target atoms are physically ejected by the bombardment of energetic particles, such as accelerated gas ions. The sputtered atoms travel through the plasma and undergo multiple collisions with the plasma species and subsequently deposit on a substrate.

There are many advantages for using sputtering, such as an excellent film uniformity, surface smoothness and thickness control, deposition of films with nearly bulk-like properties, good adhesion, and high deposition rates.

The growth of epitaxial thin films by sputtering depends on many deposition conditions, including the substrate temperature, the O_2/Ar gas pressure ratio, the total gas pressure, the substrate-to-target distance, sputter power, and the deposition rate [84; 85].

Th sputtering process can either employ direct current (DC) or radio frequency (RF) power, depending on the electrical conductivity of the target. DC power can be used only for conducting targets, while RF power can be used for both conducting and insulating targets. A magnetron sputtering process uses a magnetron source, where a magnetic field is employed to enhance the sputter efficiency.

Several sputtering systems were tested for the purpose of thin film deposition. These systems include DC diode sputtering, RF diode sputtering, planar- and cylindrical magnetron sputtering, and ion-beam sputtering.

The ICM sputtering system used to deposit YBCO thin films is schematically shown in Figure 4.5. The permanent rare earth magnets are placed parallel to the YBCO cylindrical target, so that the magnetic field is superposed on the cathode and glow discharge, which is parallel to the cathode surface. A water cooling system is used to protect the target and the magnets from damage, which may be caused by the generated heat in the chamber. An ultra-high background vacuum can be achieved in the chamber by using roughing- and diffusion pumps. The target-to-substrate distance was designed to be 31mm.

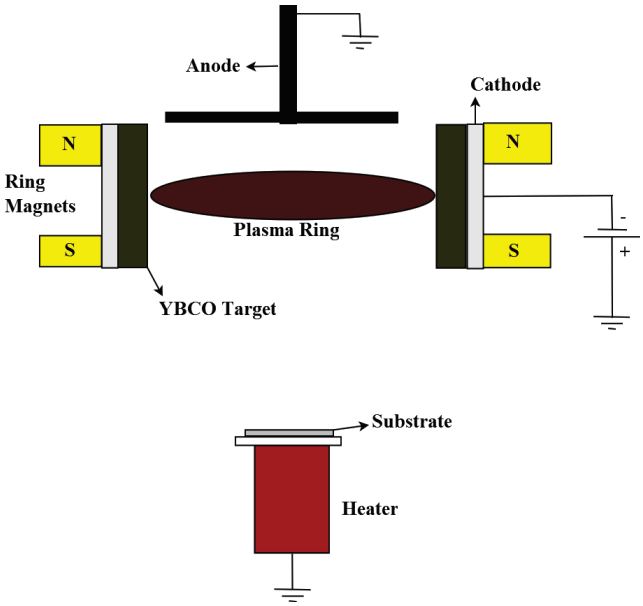

Figure 4.5: Schematic diagram of an Inverted Cylindrical Magnetron (ICM) sputtering system.

The operation of a DC magnetron sputtering process is based on the creation of a plasma discharge in the vicinity of a target, and the acceleration of the ions from the plasma to the target surface, to sputter the desired materials. The cathode, to which the target material is attached, is held at a large negative voltage relative to the substrate and walls of the chamber. Positively charged argon ions will accelerate towards the cathode, dislodging atoms from the target and leading to the build-up of a thin film on the substrate. An argon plasma is ignited in the chamber by field emission of electrons from the cathode.

The secondary electrons in the plasma discharge, which are emitted from the cathode due to ion-bombardment, show cycloidal motion perpendicular to both the electrical field E (normal to the surface) and the magnetic field (B). The centre of the orbit drifts in the direction of $E \times B$. The magnetic field is oriented such that these drift paths for electrons form closed loops parallel to the cathode surface [79]. These secondary electrons lose their kinetic energy due to collisions with gas atoms (ionisation), and the net result is an extremely

dense plasma in this drift ring at the cathode, which effectively increases the sputtering rate at the target surface.

The resputtering of the grown film by negative ions and reflected neutrals is a major problem that is encountered in the sputtering of oxide materials. It leads to morphological changes, such as pits, ripples and cones on film surfaces. The ICM configuration can significantly minimise this undesired effect.

4.5 Photolithography

Photolithography is a multistep pattern transfer process. The required pattern is first formed on photomasks and then transferred onto the surface layers of substrates through the photomasking steps.

The transfer takes place in two steps, as is shown in Figure 4.6. First, the pattern on the mask is transferred onto a layer of light-sensitive material, called photoresist. Exposure to light causes changes in its properties and therefore changes the photoresist to soften or to harden. For a positive photoresist, the exposed region, which corresponds to the transparent pattern region on the mask, becomes soluble in a chemical solution (developer). Removal of the soft portion with chemical solvents, leaves tracks in the resist layer that correspond to the opaque pattern on the mask.

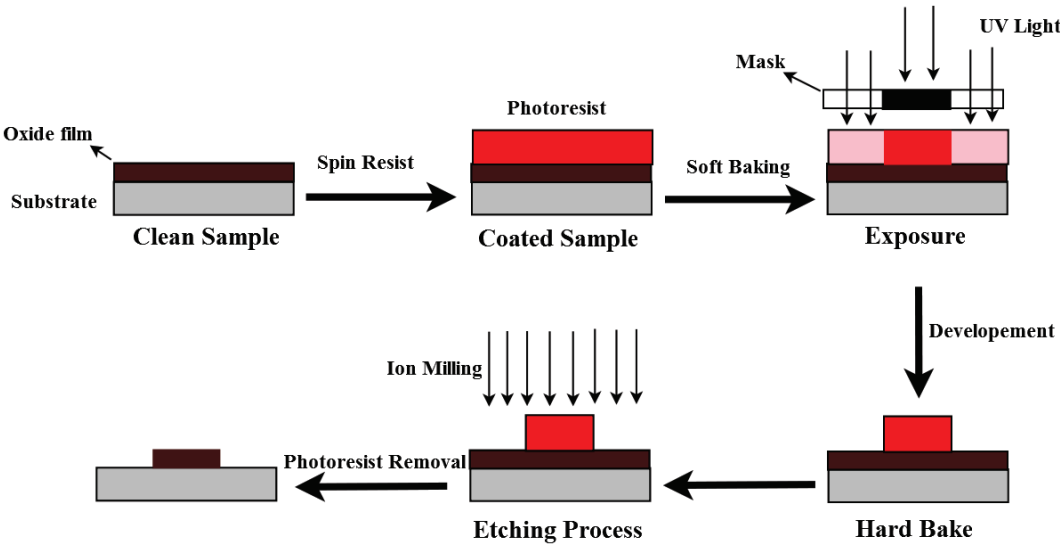

Figure 4.6: Schematic diagram of a photolithography process and the pattern transfer steps.

The second transfer process takes place from the photoresist layer onto the substrate surface layer. The transfer occurs when etchants remove the area of the substrate that is not covered by the photoresist. This can be done by chemical etching solutions or ion-milling.

The entire process of photolithography can be summarised in the following steps:

- *Substrate cleaning*: The sample surface must be cleaned extremely well. Any dust or contaminants on the surface can affect the photolithography process. The substrates should be cleaned in acetone or ethanol in an ultrasonic bath, and dried with nitrogen gas thereafter. Resist-substrate adhesion is mainly affected by water vapour. Accordingly, heating the substrate above 100°C on a hotplate evaporates any excess water.
- *Photoresist spinning*: The sample is coated with a uniform layer of photoresist. This is achieved by covering the whole sample with photoresist, and then spinning it at high speed, using a spinning machine. The spin speed, time of spinning and the viscosity of the resist are important factors influencing the final resist thickness.
- *Pre-exposure bake*: The coated sample is baked, either on a hotplate or in an oven. This step is used to evaporate the solvent from the resist, and thus hardening it. This is a critical step, because the pre-exposure bake, or soft bake, affects the photoresist properties. Baking for a short time will lead to insufficient removal of the solvent of the resist, which will affect the resist profile. Over-baking can destroy the photoactive compound of the resist and reduce its light sensitivity. Baking temperature and time can be chosen according to the photoresist datasheet.
- *Exposure*: The coated sample is baked and cooled down to room temperature. It is then placed under a chrome contact mask, in a mask aligner. The mask is aligned with the sample by micrometer adjustment screws in the alignment machine. The alignment can be verified by a microscope. The substrate is held down by a vacuum and then lifted up until it is in physical contact with the mask. The UV light source in the exposure machine illuminates through the mask onto the sample. The exposure time depends on several factors, such as the resist film thickness and the UV light intensity.
- *Development*: The sample is immersed in the chemical solvent (developer) immediately after the exposure step. The developer dissolves the exposed regions of the photoresist. The development is stopped by dipping the sample in de-ionised (DI) water.
- *Post-exposure bake*: Hard-baking is used to improve the adhesion between the resist and the substrate. It is used to increase the photoresist's wet and dry etch resistance, by hardening it. The samples are hard-baked on the hotplate. In both the soft- and hard-bake procedure the baking temperature should not exceed 130°C, which is the glass transition temperature of the photoresist.

With these steps, photoresist lines with different sidewall angles are manufactured on the sample. The sidewall angle in the resist can be optimised by controlling factors such as the baking-, exposure- and development conditions.

Every type of photoresist is designed to have high contrast over a particular wavelength

range. If the resist is exposed to light that has an inappropriate wavelength, the sidewall profile will be sloped, due to the higher absorption in the resist. A sidewall slope is, however, always observed, even at the appropriate wavelength.

4.6 Etching

Etching is the process where a photoresist pattern is permanently transferred onto the surface layers of a sample. The top layers of a sample are removed from the surface through the openings in the resist pattern.

A high-resolution pattern transfer profile (i.e. low undercutting, edge profile control, low contamination of the etched surface and a highly uniform etch rate over the sample area) is dependent on two main factors, namely selectivity and directionality. Selectivity is the degree to which the etchant can differentiate between the masking layer and the layer to be etched. Directionality has to do with the etch profile under the mask. In an isotropic etch, the etchant removes the material in all directions at the same rate, creating a semicircular profile under the mask. In an anisotropic etch, the dissolution rate depends on specific directions, and straight sidewall profiles can be obtained.

Etching procedures can be classified as either a wet- or a dry etching process. Although both categories have been successfully used to pattern YBCO thin films down to sub-micrometer dimensions [86], some factors must be taken into account. One immediate problem is that contact of YBCO with water, or water soluble chemical etchants, will deteriorate the superconducting properties. Secondly, the use of dry etching techniques in a vacuum, such as argon ion-milling, can lead to heating of the sample and thus to oxygen loss from the YBCO composition.

4.6.1 Wet Etching

The traditional method of etching has been by immersion of the sample, using wet etchants. Samples are immersed in a liquid chemical etchant for a specific period of time, transferred to a rinse bath for acid removal, and thereafter, transferred for a spin-dry step.

Etching uniformity and process control are enhanced by the addition of heaters and agitation devices, such as ultrasonic waves for the immersion tanks.

Wet etchants for YBCO are chemically selected for their ability to uniformly remove the top layers of samples without attacking the underlying material. The etchants must only react with the YBCO and leave the substrate and the resist intact.

The most common wet etchants are bromine in methanol, ethylenediaminetetracetic acid (EDTA) [87], dilute sulphuric acid [88], nitric acid and citric acid [89]. Although structure sizes down to micron feature sizes are possible, chemical wet etching causes problems in

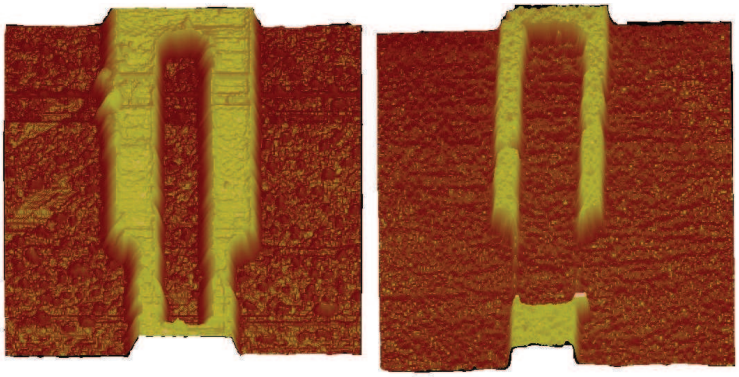

Figure 4.7: The undercut problem of the wet etching technique.

providing smooth side walls by undercutting the photoresist stencils, as is shown in Figure 4.7. Another problem is that the water in aqueous solutions reacts with YBCO and degrades the superconducting properties.

Ethylenediaminetetracetic acid (EDTA) and citric acid were used to etch the YBCO thin films in this work. The chemical solutions were diluted in DI water. The sample was then immersed in the acid in an ultrasonic bath. The etching time was dependent on the thickness of the YBCO film. Most of the YBCO samples were etched within 40-70 seconds. When the substrate under the YBCO layer became visible, the sample was removed from the solution, rinsed in DI water, and checked under the microscope.

The utilisation of wet etching may be limited by a number of considerations, such as the pattern sizes ($\sim 3\mu$m or bigger), the isotropic etching process resulting in sloped sidewalls, the requirement for rinse and dry steps, and the toxicity of wet chemicals.

4.6.2 Dry Etching

Most dry etching techniques are plasma-based. They have several advantages when compared with wet etching. These include smaller dimensions, smaller undercut, low etching rates, and higher anisotropicity. The three basic dry etching techniques are chemical dry etching, ion-milling and reactive ion-etching (RIE).

Ion-milling is a purely physical process. Atoms on a solid surface are removed under irradiation by energetic ions. The ion-milling process is governed by collisions between the irradiated atoms and the surface atoms of the sample. A confined plasma from argon gas is used in a vacuum chamber to generate ions. The ions are accelerated by a high potential to create a collimated beam, which bombards the sample surface.

The schematic diagram of the ion-mill system at Stellenbosch University is shown in Figure 4.8. The system consists of a vacuum system, an RF multicusp ion source, a neutraliser and a water cooled sample stage. The vacuum system contains a stainless steel vacuum chamber

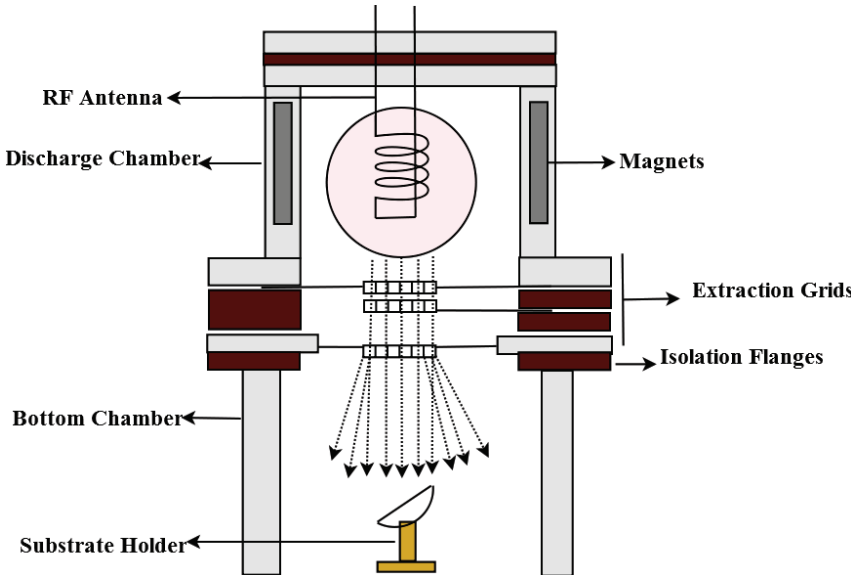

Figure 4.8: Schematic diagram of the ion-mill system at Stellenbosch University.

that is pumped by roughing and diffusion pumps. The chamber has a glass window that allows observation of the progress of the milling process.

The sample is placed on a holder in the bottom chamber, and a stream of argon gas is introduced into the discharge chamber. An RF antenna, fed by a 50 W RF source, operating at a frequency of 13.56 MHz, initiates and sustains the ionisation of the argon gas. The sample is held on a negatively grounded holder, which attracts the ionised argon atoms. As the argon atoms travel to the bottom chamber, they accelerate, picking up energy. At the sample surface, they crash into the exposed sample layer and literally blast small amounts from the sample surface.

Ion-mill systems have many features, i.e. samples are not in the plasma region, the incident angle of ions is controllable (etching rate is controllable), the ion energy is controlled independent of the working pressure, and the ion current density is controlled by either the ion energy or the gas pressure. More details about the ion-mill system at Stellenbosch University are available in [28].

4.7 Thin Film Characterisation

High-quality epitaxial thin films are required for superconducting electronic devices and applications. YBCO thin films are mainly characterised for their surface smoothness and -roughness, correct grain orientation and correct phase of the material, and for their superconductive properties.

This section provides an overview of the analysis techniques utilised to characterise the film

quality. X-ray diffraction, Atomic Force Microscopy (AFM), and resistivity- and susceptibility tests were used to characterise the film quality in this dissertation.

4.7.1 X-Ray Diffraction (XRD)

X-rays were discovered in 1895 by the German physicist Wilhelm Conrad Röntgen. In 1912, another German physicist, Max von Laue, suggested that crystals may act as diffraction gratings for X-rays. Von Laue developed the theory to explain X-ray diffraction and won the Nobel Prize in 1914.

Soon after Henry and Laurence Bragg found that diffracted X-rays can be reflected by sets of parallel planes of atoms. The condition for diffraction from a set of parallel planes of interlayer spacing d is given by

$$\sin\theta = \frac{n\lambda}{2d}, \tag{4.1}$$

where θ is the incident angle of the X-rays on the planes and λ is the X-ray wavelength.

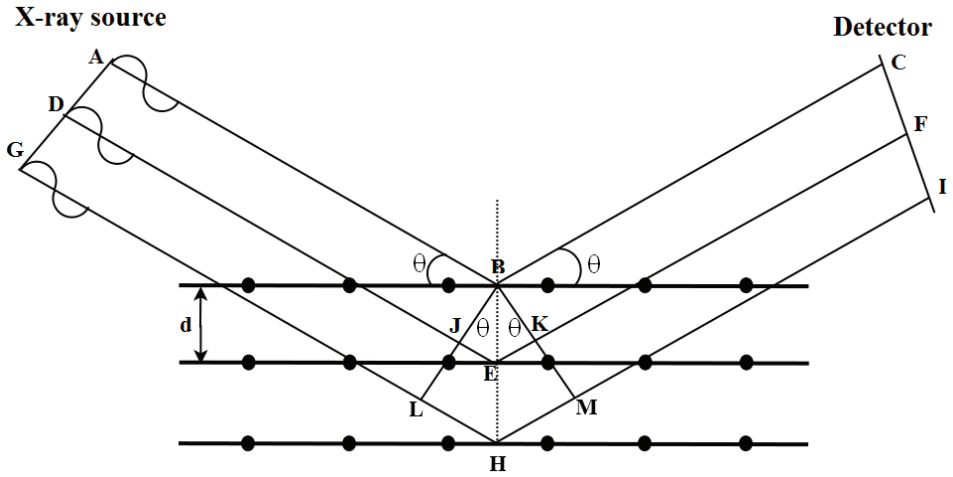

Figure 4.9: Illustration of Bragg reflection from a set of parallel planes of atoms (Adapted from [3])

All the wavelets of the X-ray beam leave the source with the same phase. As the wavelets enter the crystal, they travel longer distances than the wavelets reflected from the surface. These distances are dependent on the interlayer spacing, d. The path length difference between the wavelets ABC and DEF is JE+EK and for wavelet GHI it is LH+HM. The condition for diffraction is that the wavelets be in phase at BKM. However, this requires that the distance JE+EK=nλ, which is an integral number of wavelengths.

If JE+EK=λ, then LH+HM=2λ, and all the layers in the stack scatter in phase and thus the intensity of diffracted photons is increased and is recorded by the detector. A schematic drawing of the Bragg reflection family of planes is shown in Figure 4.9.

X-ray powder diffraction is widely used throughout industry, academia or wherever knowledge of solids is required. Although there are many manufacturers of powder diffractometers, the majority of commercial systems employ the Bragg-Brentano parafocusing geometry.

A *Bruker AXS D8 Advance* diffractometer was used to perform X-ray powder diffraction on all the YBCO thin films during this work. The machine uses a θ:θ vertical measurement configuration, which gives information on the phase, orientation and lattice parameters of the films. Both the X-ray tube and the detector are moving, so that the same angle θ is maintained by both devices relative to the film under test.

Table 4-II: Calculated 2θ of the first six C(001)-axis peaks of an orthorhombic YBCO thin film XRD pattern.

Peak number (l)	1^{st}	2^{nd}	3^{rd}	4^{th}	5^{th}	6^{th}
Inter-planar spacing (d_{00l})	11.68$\mathring{A}$	5.84$\mathring{A}$	3.894$\mathring{A}$	2.92$\mathring{A}$	2.336$\mathring{A}$	1.947$\mathring{A}$
Angle 2θ	7.57°	15.17°	22.84°	30.61°	38.54°	46.66°

The diffractometer scans the required 2θ range in discrete steps. At each step, the diffractometer remains in position for a period of time, recording the photon intensity. A powder diffraction pattern is produced when these measured intensities are plotted against 2θ. The pattern manifests as a series of peaks, each peak being associated with some set of crystal planes, with spacing defined by (4.1).

A typical X-ray powder diffraction pattern of an epitaxial YBCO thin film, with a single orthorhombic phase and *c*-axis orientation, should only illustrate the presence of (001) peaks. The *c*-axis lattice parameter is c=11.68 Å. The distance between successive planes for the orthorhombic phase can be expressed by [3]

$$\frac{1}{d^2} = \frac{h^2}{a^2} + \frac{k^2}{b^2} + \frac{l^2}{c^2}. \tag{4.2}$$

The copper radiation of the X-ray tube has a wavelength of $\lambda = 1.54$ Å. By using these values one can predict where the (001) peaks for YBCO will be in the pattern. Table 4-II shows the calculated 2θ values for the first 6 *c*-axis peaks.

4.7.2 Atomic Force Microscopy (AFM)

AFM is a member of the scanning probe microscope (SPM) family. It was invented in 1986 by G. Binning *et al* [90].

AFM is used to image surface topography and it can measure electrical, chemical and mechanical properties of conductive and nonconductive materials on a molecular scale. It detects the forces interacting between the sharp tip and the sample surface, from which a topography profile can be derived [91].

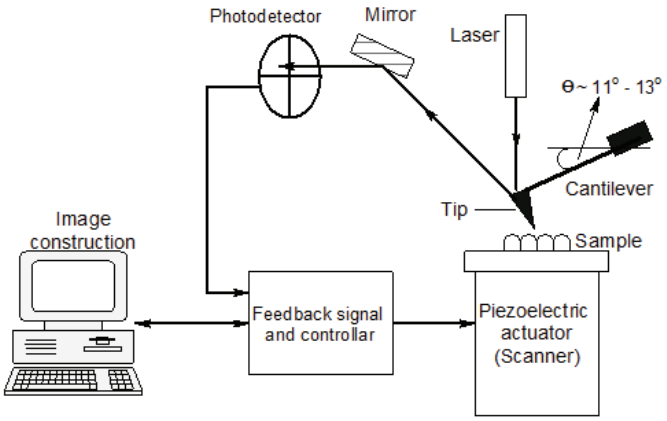

Figure 4.10: Block diagram of the essential components of an AFM in contact mode operation.

The basic operation of an AFM is illustrated in Figure 4.10. The tip touches the sample surface, as it is raster scanned across the surface. A laser beam, focused on the back of the cantilever, is reflected into a mirror, where it is reflected again onto a multi-segmented photodetector. Sample features, with varying height, deflect the cantilever, and with it the laser beam. This deflection results in a different reading at the photodetector [91].

The output of the photodetector is fed into the controller to maintain a constant value of force by means of a piezoelectric actuator. The voltage necessary to maintain a constant force on each scan point in the image results in a topographical image with nanometer resolution.

The tips are manufactured from silicon (Si). The tip is mounted at the end of a flexible micro-cantilever, which bends easily in response to the interacting forces between the tip and the sample surface.

The AFM can work in three scanning modes, namely contact-, non-contact- and tapping mode. Each mode has its advantages, which depend on the application and the sample type and surface.

Contact Mode

In contact mode, the tip makes soft physical contact with the sample surface. As the scanner traces the tip across the sample surface, the cantilever is deflected by the contact force to

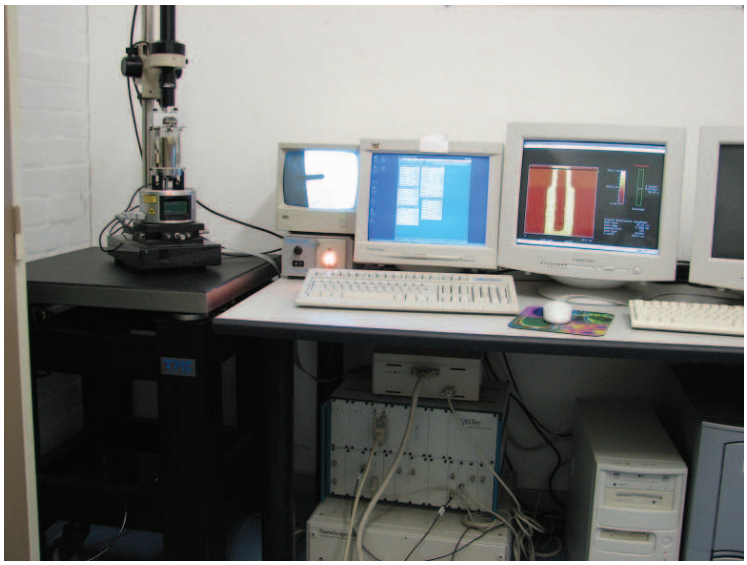

Figure 4.11: AFM instrument (*NanoScope II Digital Instruments*) at Stellenbosch University. The sample image is displayed on the second monitor.

accommodate changes in topography. The cantilever deflection is maintained at constant level by the feedback control system, by applying a voltage to the piezoelectric actuator. The voltage causes the scanner to move up or down in vertical direction with a distance proportional to the voltage magnitude. The applied voltage can be converted into height information to create images. Frictional force is the main disadvantage of the contact mode, as it may cause damage to the sample.

Tapping Mode

To overcome the frictional force problem, tapping mode is used to image surfaces. The tip is oscillated above the sample and contacts the sample surface once in each oscillation cycle. In tapping mode the tip and the sample surface are separated by a small distance. The amplitude and the resonant frequency of the cantilever's oscillation changes as the tip-sample distance changes.

As the probe is scanned over the sample's surface, the topography may change, and this change results in a change in the oscillation amplitude or in the resonant frequency, which is detected by the control unit. The system then applies a voltage to the piezoelectric actuator to maintain the set amplitude or resonant frequency. Due to the larger distance between the probe and the sample, the resolution is not as good as in contact mode. More information about the AFM can be found in [92].

Figure 4.11 shows the AFM instrument at Stellenbosch University at the Polymer Science Institute, which was used for the work in this project.

4.7.3 AC Susceptibility Measurements

The superconducting properties of samples can be measured with a susceptibility test. This widely used method entails the generation of a harmonically varying magnetic field to probe the sample and then recording the magnetic response of the sample. The AC susceptibility measurement will yield the critical temperature, T_c, and illustrate the width of the superconducting transition (ΔT) of the sample under test.

In the test setup the sample is mounted between two small coils situated inside the cold finger of the cryocooler. The primary coil is driven by a 1 MHz AC current, which induces a magnetic field perpendicular to the film surface. The secondary (pick-up) coil, which can detect the magnetic response of the sample, will return the induced voltage to the controller, indicating a percentage of susceptibility reading.

The magnetic field will penetrate the whole sample when the temperature is above T_c. The induced voltage across the secondary coil will thus be a maximum and the controller will show a 100% susceptibility reading. However, when the transition to the superconductive state occurs, the magnetisation of the sample changes due to flux exclusion. Below the critical temperature the sample will thus expel any magnetic fields and no induced voltage will therefore be measured over the secondary coil. The susceptibility reading of the controller will thus drop to a very low value.

During the cooling process the temperature and the corresponding susceptibility percentage reading are sampled and recorded to a computer, where the results are displayed.

4.8 AFM Nanolithography

The fabrication of nanoscale structures and devices on semi- and superconducting materials has been the subject of intense interest and study in the last couple of years. Major advances in nanoscience and nanotechnology have enabled the development of techniques and new tools for fabricating and characterising nanostructured materials.

Conventional techniques for nanofabrication are based on various lithographical methods, including X-ray lithography, electron-beam lithography and focused ion-beam lithography. The applicability of these techniques is often limited by their high operating cost, and multi-step processes. However, several novel methods and techniques have been developed recently to offer flexible alternatives for nanoscale patterning and fabrication.

Amongst these newer techniques, AFM nanolithography has proved to be a unique and novel tool for material structuring and patterning with nanometer precision [93]. The technique has been used for patterning of a wide range of materials, including polymers, metals, compounds, semiconductors and superconductors [94].

The working principle of AFM nanolithography is based on the interaction between the tip

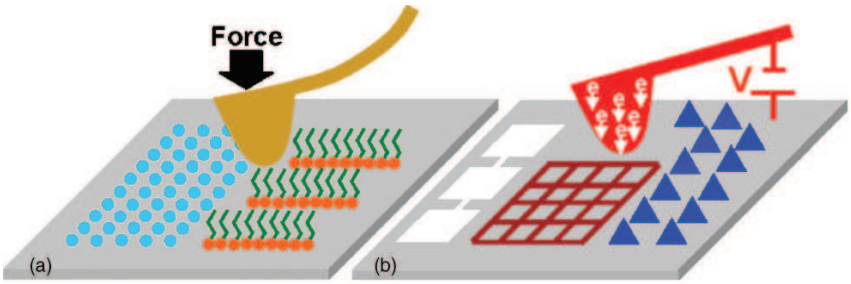

Figure 4.12: Illustration of (a) force-assisted, and (b) bias-assisted AFM nanolithography (Adapted from [4])

and the sample. When suitable forces are exerted, or external fields applied, the tip can induce various physical and chemical processes on the sample surface. AFM lithography techniques can be classified into two groups in terms of their operational principles [4]:

- *Bias-assisted AFM nanolithography:* The tip is biased to create a localised electric field, and the tip acts as a nanoscale electrode for current injection. Under such a high localised field, electrostatic processes can be initiated to facilitate pattern formation. A degree of humidity and a conductive sample are required to employ this method. Depending on the magnitude of the tip bias and the sample material, the application of a tip voltage can lead to anodic oxidation, electrochemical deposition, electrostatic attraction and nanoscale explosion.

- *Force-assisted AFM nanolithography:* A large force is applied to the tip for pattern fabrication, and the tip-surface interaction is mainly mechanical. Tip indentation, static ploughing and dynamic ploughing are three typical methods used in this group. Tip indentation is used for single structure formation in which the tip is immobilised at a specific surface spot. A large force is then applied to the tip to indent the surface. In static ploughing the tip is operated in contact mode, and is scanned with a large loading force on the sample surface to form trenchlike structures. Atoms and nanomaterials are removed from the sample surface with each scan cycle. Dynamic ploughing involves scratching the surface with a vibrating tip in tapping scan mode. The force of the tip is modulated by adjusting the amplitude of the cantilever oscillations. When the tip approaches the sample surface, structures are formed by elastic and plastic deformations on the sample. Figure 4.12 illustrates the two main groups of AFM nanolithography.

Several authors have successfully demonstrated the fabrication of Josephson junctions and SQUIDs on LTS and HTS superconductors, using AFM nanolithography techniques. Bouchiat *et al* [63] used the bias-assisted method to fabricate SQUIDs. The fabrication of the nanodevices was based on the local oxidation of the niobium surfaces, while Insang *et al* [95] used the same method to fabricate Josephson junctions from YBCO material. The force-assisted method (ploughing) was also used to fabricate Josephson junction structures

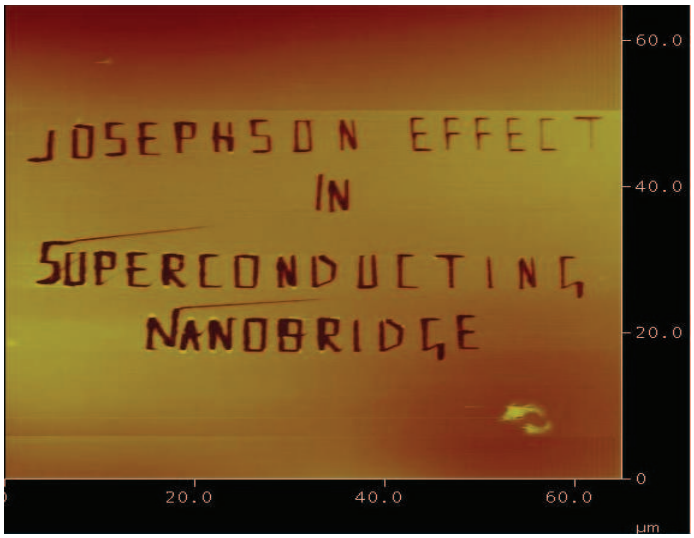

Figure 4.13: A silicon tip was used to write words on a photoresist coated substrate. All the tip movements were controlled and the words predefined with a small script code.

from LTS [64] and intrinsic Josephson junctions from YBCO thin films [96].

In this dissertation static ploughing AFM nanolithography will be used to fabricate Josephson junction structures. Such structures will be created by directly scratching the YBCO strip surface with an AFM probe. Although silicon tips can be used for lithography, diamond tips are preferable for hard surfaces. The diamond tip is actually a silicon tip coated with a diamond layer, which makes it much harder than a typical silicon tip. By repeated scanning of the tip along a predefined pattern at a high loading force, mechanically induced etching will be observed on atomic scale.

An additional lithography program allows for the microscope to be used to inscribe lines on material surfaces by controlling the diamond tip movements, and thus using the tip as a mechanical tool (see Figure 4.13 as an example). The lithography program uses the *C* programming language, along with *Nanoscript*™ macro litho functions to manipulate the tip relative to the sample surface.

4.9 Summary

This chapter discussed the basic principles of thin film growth and thin film deposition techniques (including the ICM technique, which was used in this research). Important aspects, such as the YBCO crystal structure and substrate issues, were presented. Concepts regarding photolithography and etching processes were highlighted. Next, a few characterisation techniques to analyse thin film growth and its properties, were discussed. The chapter concluded with a discussion of AFM nanolithography.

Chapter 5

Planar Micro-Bridge Type Josephson Junctions: Fabrication and Characterisation

In this chapter all the required process steps for the fabrication of micro-bridges will be discussed in detail. The steps include HTS thin film deposition and analysis, photolithography, etching, pad deposition and AFM nanolithography. The second part of this chapter will show the experimental results in order to confirm the Josephson behaviour of the junctions.

5.1 Fabrication process

5.1.1 YBCO Thin Film deposition

In order for high-T_c superconductor materials to show their interesting properties for device applications, they should be grown in an epitaxial manner and in the correct phase. This can be obtained by deposition of the materials at high temperatures on an appropriate substrate, and cooling them down in a high oxygen pressure environment. This cooling process will result in an orthorhombic phase being formed in the YBCO, with an optimal oxygen content in the crystal.

YBCO thin films were deposited on MgO substrates that were polished on the one side, using Inverted Cylindrical Magnetron (ICM) sputtering. The size of the substrates that were used were 5×10 mm and 10×10 mm. The substrates were cleaned with acetone in

an ultrasonic bath and then blown dry with nitrogen gas, as substrates with degraded or contaminated surfaces will reduce the film critical current density [97]. The substrates were then glued onto a heater plate by silver paste to ensure good thermal contact.

Figure 5.1 illustrates the deposition temperature profile that was used for the YBCO thin films. Pre-sputtering was applied for 15 minutes to eliminate any contamination on the surface of the target. Details of the ICM sputtering operational procedures can be found in Appendix A.

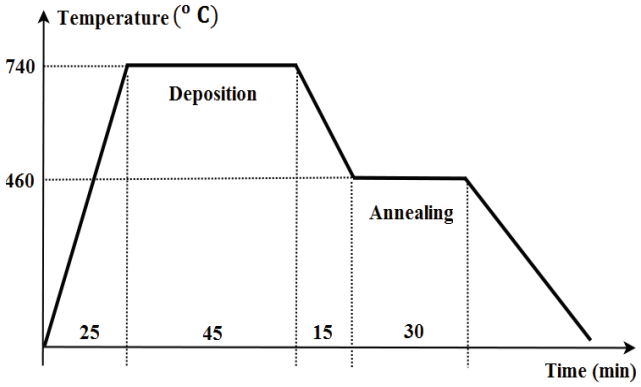

Figure 5.1: Temperature profile that was used to grow the YBCO thin films, using ICM sputtering

The system parameters that were used during the deposition process are listed in Table 5-I. Initially, we started with the same parameters that was used by Vainan [28]. However, due to voltage arcing and difficulty to ignite the plasma, some of the parameters were optimised for better deposition conditions.

Table 5-I: Deposition parameters for YBCO thin film deposition using ICM sputtering

Parameter	**Value**
Deposition	Off-axis DC magnetron sputtering
Substrate temperature (T_{sub})	740 °C
Argon-oxygen pressure ratio	1:1
Total pressure (P_{TOT})	225 μHg
DC sputtering power	72 W (I=400mA and V=180V)
Deposition rate	2.7 nm/min
Annealing temperature	460 °C
Film thickness	100nm - 120nm

5.1.2 YBCO Thin Film Characterisation

Surface- and thin film analyses can generally be performed using many different types of techniques, such as X-ray photoelectron spectroscopy (XPS) (based on electron detection),

secondary ion-mass spectrometry (based on ion detection), Rutherford backscattering spectroscopy (RBS) (based on ion-scattering), and scanning probe microscopy, such as AFM. However, our prepared samples were characterised by AFM, X-ray diffraction analyses, and susceptibility- and resistivity measurements.

Surface analyses have been performed with AFM in order to study the morphological properties of the films. The surface roughness image of one of the deposited YBCO films is shown in Figure 5.2. The AFM images show very smooth surfaces with 4-6 nm roughness, and without any micron-sized particles and droplets on the surfaces. However, a few outgrowths with small sizes can be observed on the surface.

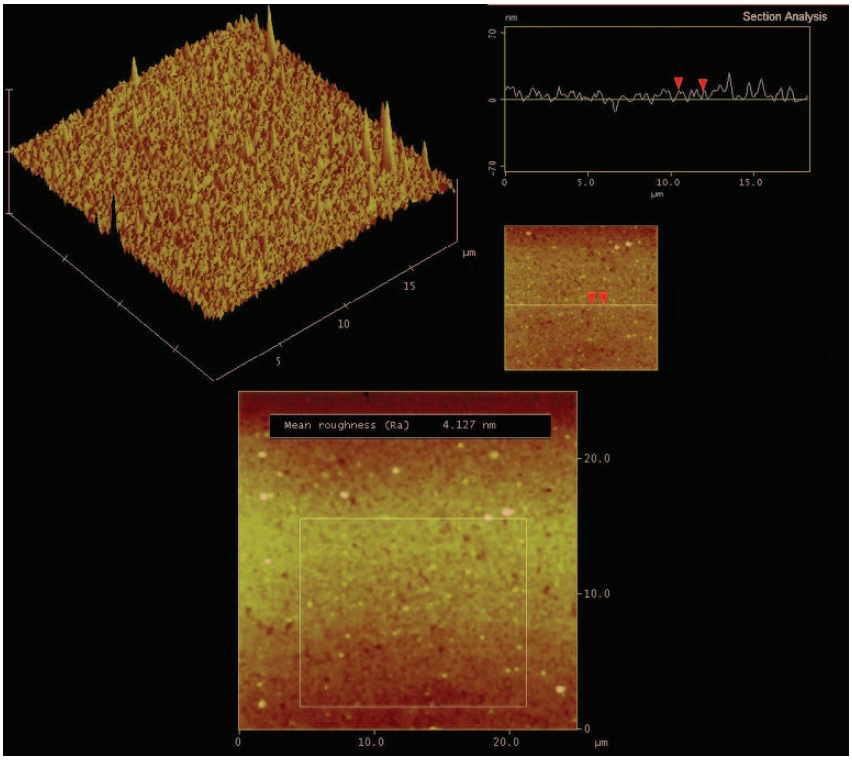

Figure 5.2: An AFM image illustrating the surface roughness measured on a deposited YBCO film.

X-ray diffraction (XRD) was employed to characterise the epitaxial growth, and to detect the presence of any unusual phases. X-ray diffraction results of a 100 nm YBCO thin film, grown on an MgO substrate, is shown in Figure 5.3. The grown films are highly *c*-axis oriented, strong and weak (001) peaks of the superconducting YBCO phases were observed, as well as a few peaks of impurities. The amplitudes of the impurity peaks are much smaller and weaker than the amplitudes of the peaks of the superconducting YBCO phases.

The quality of the as-deposited YBCO thin films was checked by measuring the superconducting transition temperature by AC susceptibility measurements. Figure 5.4 shows the

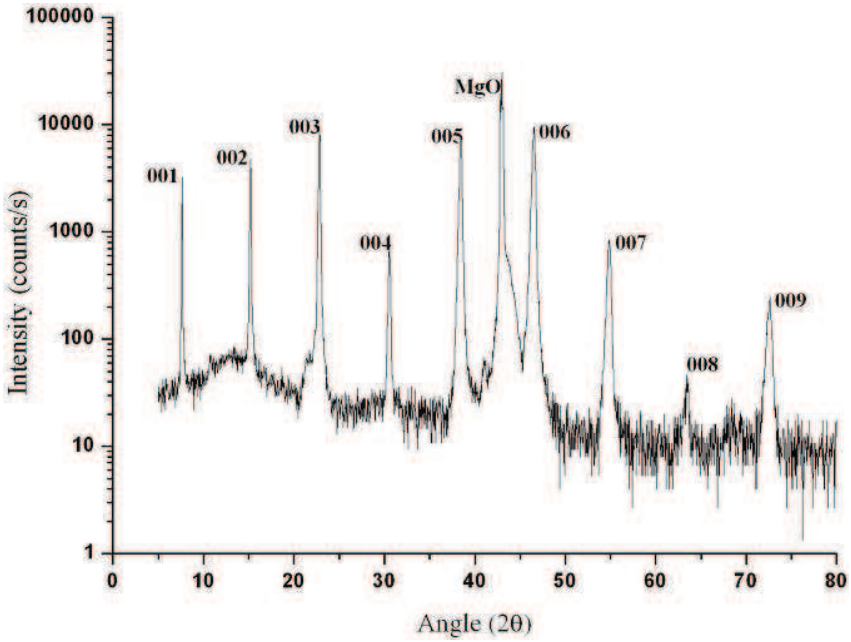

Figure 5.3: XRD spectra of a 100 nm thick YBCO film deposited on an MgO substrate.

transition temperature (T_c) for a deposited YBCO thin film. The onset T_c for the sample (∼89.5 K) is almost the same as those reported by a number of groups. The sample also had a sharp transition with a transition width of less than 1.5 K.

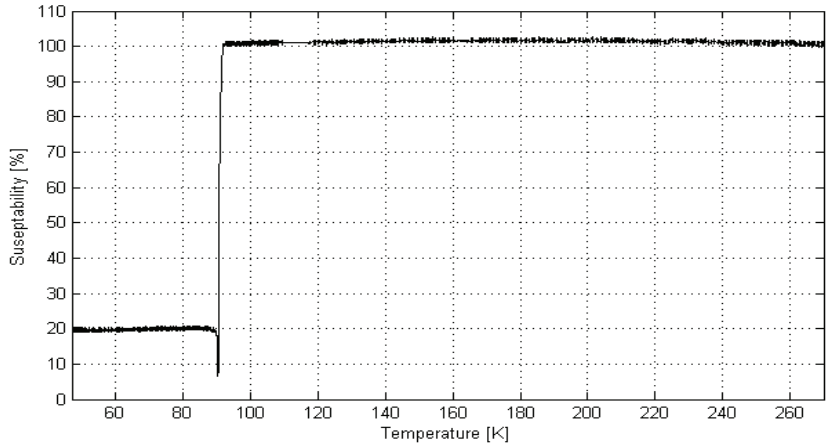

Figure 5.4: Susceptibility test result for a 100 nm thick YBCO film deposited on an MgO substrate.

Four-point probe (resistivity) measurements have also been performed. The measurement gives the DC resistance of the YBCO thin film, but requires the deposition of novel metal pads and wire bonding (see Section 5.1.4 for pad deposition procedures).

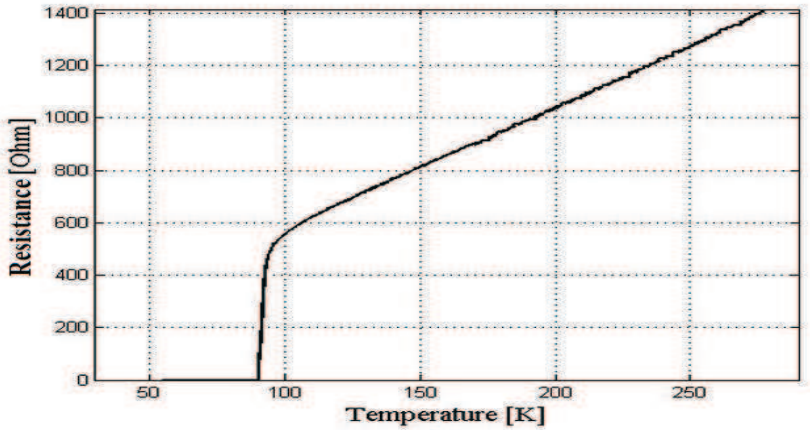

Figure 5.5: Measured resistance versus temperature characteristics for a 100 nm thick YBCO film deposited on an MgO substrate.

The temperature dependence of the electrical resistance is shown in Figure 5.5. The film showed metallic-like resistive behaviour in the normal state and had a sharp superconducting transition. The residual resistance ratio $R(300)/R(100)$ was 2.83. The zero-resistance temperature (T_{c0}) was 90.2 K with a superconducting transition width of less than 1.5 K.

These results emphatically confirmed that the films had good superconducting properties.

5.1.3 Photolithography

All films were processed using standard photolithography procedures. All the 5×10 mm substrates were patterned into five YBCO thin film tracks, 8-10 μm wide, while the 10×10 mm substrates were patterned into ten YBCO tracks and a ground plane. Three different positive photoresists were used during the course of this dissertation. Table 5-II lists the parameters for each resist.

Table 5-II: Photoresist parameters.

Resist	**Microposit S1818**	**SPR700**	**ma-P 1225**
Spin speed (rpm)	4500	4600	4000
Spin time (s)	60	50	40
Soft bake	115 °C/120 sec	115 °C/90 sec	100 °C/10 min
Exposure time (sec)	15	25	25
Developer & Developer time	MF320 for 45 sec	MF 24A for 30 sec	ma-D 331 for 50 sec
Hard bake	90 °C/20 min	95 °C/5 min	110 °C/30 min
Resist thickness (μm)	1.6	1.9	2

The pre-defined mask was successfully transferred to the photoresist layer. Figure 5.6 shows AFM and optical microscopy images of patterned resist on top of the YBCO films. The

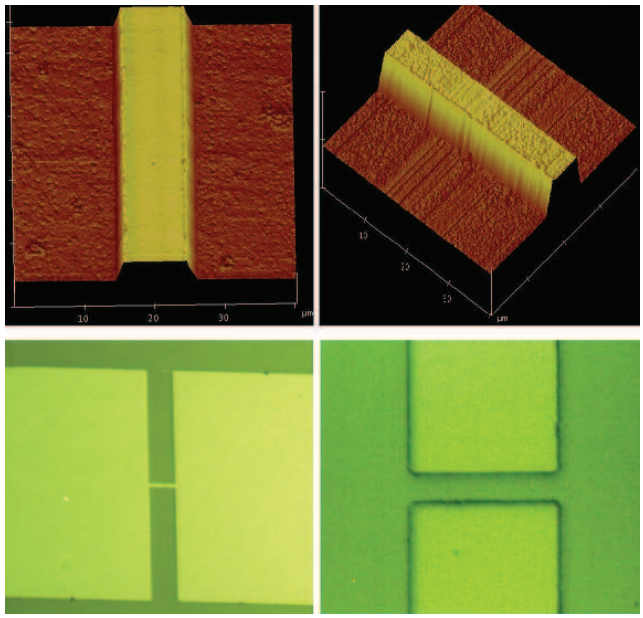

Figure 5.6: AFM images (top) and optical microscope (OM) images (bottom) of a patterned resist layer on top of an YBCO thin film.

light colour in the right optical microscope image and the dark colour in the left optical microscope image are the patterned photoresist layers.

5.1.4 Etching and Pad Deposition

Two methods of etching were used for our samples. The first is a wet etching process, in which acid-based chemical solutions are used to etch away the unwanted YBCO. A 0.1 mol solution of citric acid or ethylinediaminetetraacetic acid (EDTA) was used to etch the YBCO films.

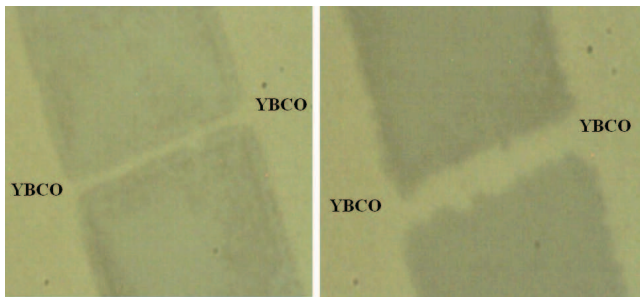

Figure 5.7: Optical microscopy images of YBCO tracks with undercut from chemical wet etching.

However, disadvantages such as underetching and the degradation of superconducting prop-

erties of the etched films were observed. The images in Figure 5.7 show some results of the wet etching process.

Secondly, a dry etching process was used, in which accelerated ions to etched away the YBCO layers. Dry etching was performed using argon ion-milling with an ion-beam incidence angle of 45 ° to the film surface, an RF power of 50 W, an argon gas pressure of 0.3×10^{-3} mbar, and the voltages of the electrodes at 750 V.

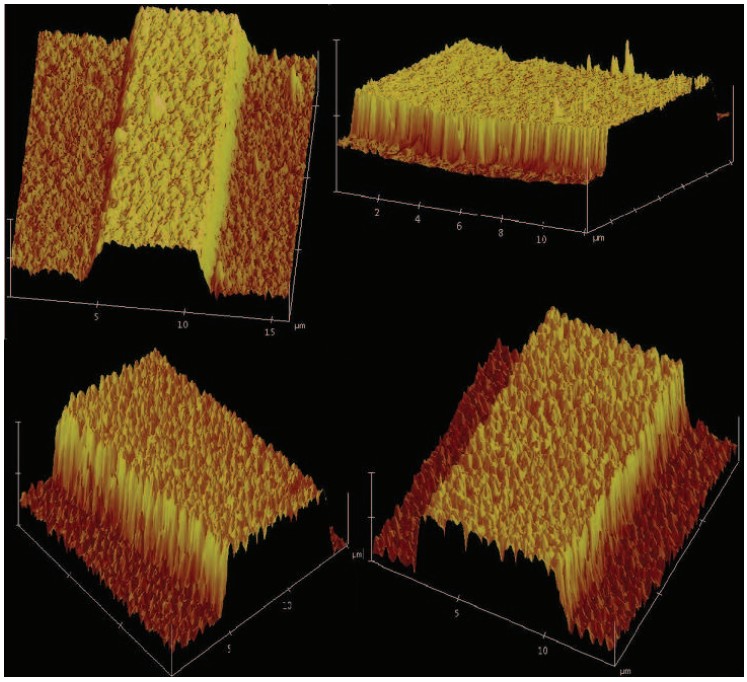

Figure 5.8: AFM images of 8 μm wide YBCO lines etched by ion-beam milling.

In order to minimise the loss of oxygen from the superconducting layers during the milling process, the film was mounted on a water-cooled copper sample holder with thermal paste. However, we made an additional modification to the system by adding a small shutter on top of the sample surface. The shutter was rotated using a small motor which was biased by rectangular pulses. The sample surface was exposed to the accelerated ions for 4 seconds and then covered by the shutter for 6 seconds. This solved the problem of losing the superconducting properties of the tracks, which had been reported by a couple of students before.

The etching was terminated when an open circuit on the substrate, at the sides of the YBCO tracks, was measured. Photoresist residue was removed by immersing the sample in photoresist remover for 10 min, and then immersing it in acetone for another 10 min in an ultrasonic bath.

Some results of dry etching on YBCO tracks are shown in Figure 5.8. The degradation of

the superconducting properties of the tracks was very small, and the T_c of the tracks was 3-5 K lower than the as-deposited thin film T_c.

In order to connect the sample to external test equipment, electrical contacts had to be provided. Silver (Ag) contact pads were deposited on the patterned YBCO by thermal evaporation. Silver is a good choice, because it does not react with YBCO and has a small contact resistance. It is also important to ensure that the silver layer is thick enough to be used for wire bonding.

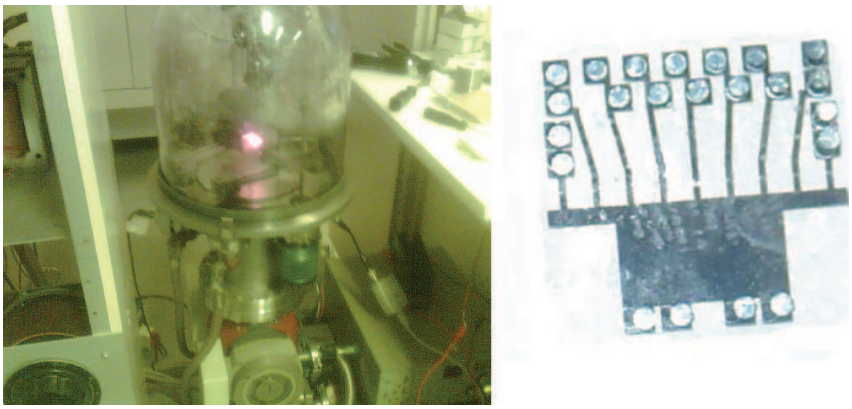

Figure 5.9: Thermal evaporation unit (left) and silver contact pads on YBCO tracks after annealing (right).

The sample was aligned with a metal mask that has 0.5 mm holes drilled where the contact pads should be deposited. The sample was placed inside the vacuum dome. The crucible in the vacuum dome was filled with silver and heated under a high vacuum (10^{-6} mbar). The silver melted and started to evaporate inside the dome. After the evaporation was complete, the sample was annealed at 450 °C for 30 minutes in an oxygen atmosphere to form a good adhesion between the silver and the YBCO surface [98].

The evaporation unit is shown in Figure 5.9, as well as the silver contact pads, after the annealing process.

5.1.5 Fabrication of Micro-bridges using AFM Nanolithography

A diamond coated AFM tip was used as a cutting tool to define the plough. The AFM was operated in contact mode. The tip, shown in Figure 5.10, was vertically displaced toward the YBCO surface with a loading force of 11μN, sufficient to completely remove the YBCO layers.

An YBCO track was imaged first, and then the middle of the track was shifted to the centre of the image. At the start of the nanolithography process, the tip was placed at the centre of the track. The constriction width W was controlled by displacing the tip by $W/2$ to the

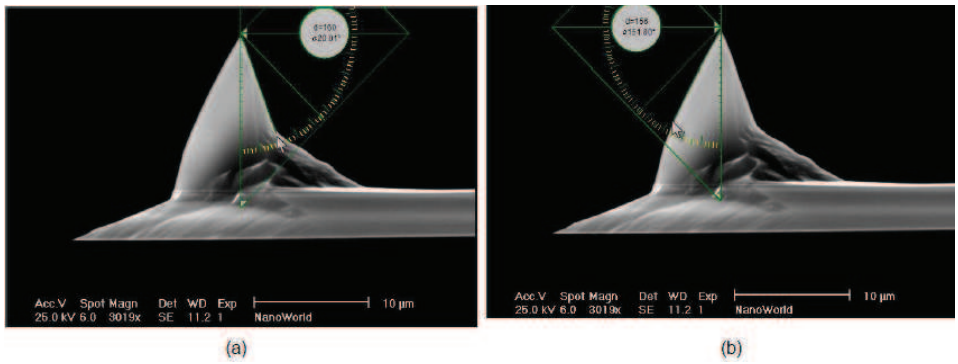

Figure 5.10: SEM images of an AFM cantilever and tip. (a) Point-probe back angle, and (b) point-probe front angle.

left-side of the track. The tip was then driven into the YBCO surface, and displaced on the same line for a few hundred cycles. The tip velocity was 4 μm/s. The constriction was completed by applying the same lithography on the right-side of the track. Constrictions with fully controlled width and depth were achieved by adjusting the tip movement and the scan speed of the ploughing operation. Figure 5.11 illustrates the cutting operation.

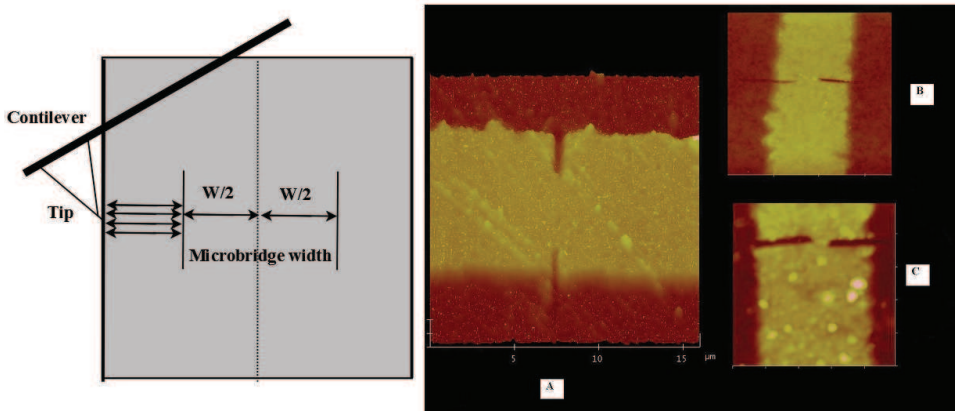

Figure 5.11: Schematic illustration of the AFM tip cutting the YBCO track (left), and on the right the micro- and nano-plough bridges made with AFM nanolihtography are shown, with a) 3.6 μm, b) 2 μm, and c) 750 nm constriction widths.

YBCO residuals from the cuts were cleaned by dipping the samples in acetone in an ultrasonic bath for a few minutes. The only drawback of this technique is the wear and resolution degradation of the tips after they have been used extensively in the lithography processes.

After the successful completion of the lithography processes and the fabrication of the microbridge structures, the samples were mounted on a printed circuit board (PCB). Extremely thin gold wires were then bonded from the contact pads to the copper strip lines on the PCB, using an ultrasonic wire bonder in the cleanroom.

5.2 Laboratory Challenges

This section highlights some problems and challenges that were faced in the laboratory during the fabrication of the Josephson structures.

5.2.1 Optimisation of Deposition Parameters

In order to determine the quality of the YBCO thin films, the superconducting properties were measured using a variety of techniques. High quality YBCO thin films were not initially achieved. The ICM sputtering parameters had to be optimised in order to produce good films.

The susceptibility and XRD measurements of some of the samples that were used during the optimisation process are shown in Figure 5.12 and Figure 5.13 respectively.

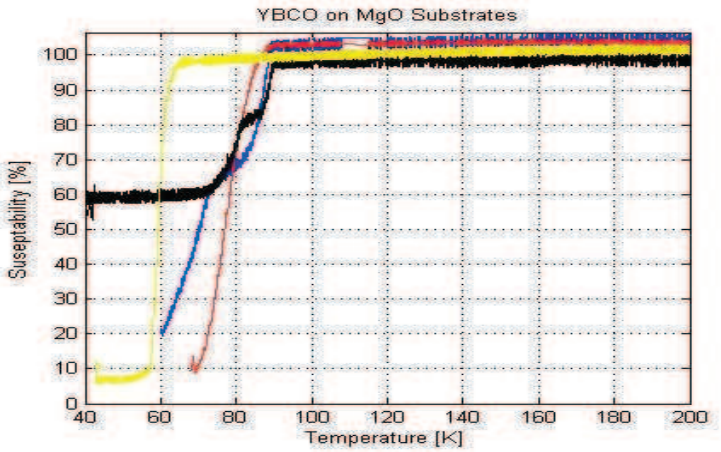

Figure 5.12: Susceptibility measurements of grown YBCO films for different deposition parameters. All the curves show bad superconducting transitions.

The surface of the initial YBCO target was not smooth, and cracks and other surface damage were observed, as is shown in Figure 5.14. From an experimental point of view, we think that the damage was caused by heat, as well as from the high-voltage discharges and sparks in the chamber.

A new YBCO target from *Adelwitz Technologiezentrum GmbH (ATZ)* (`http://www.atz-gmbh.com`) was ordered. The deposition parameters were changed and optimised for better YBCO thin film production. The susceptibility measurements shown in Figure 5.15 illustrate the quality and good superconducting properties of the films that were prepared with the new target and the optimised parameters.

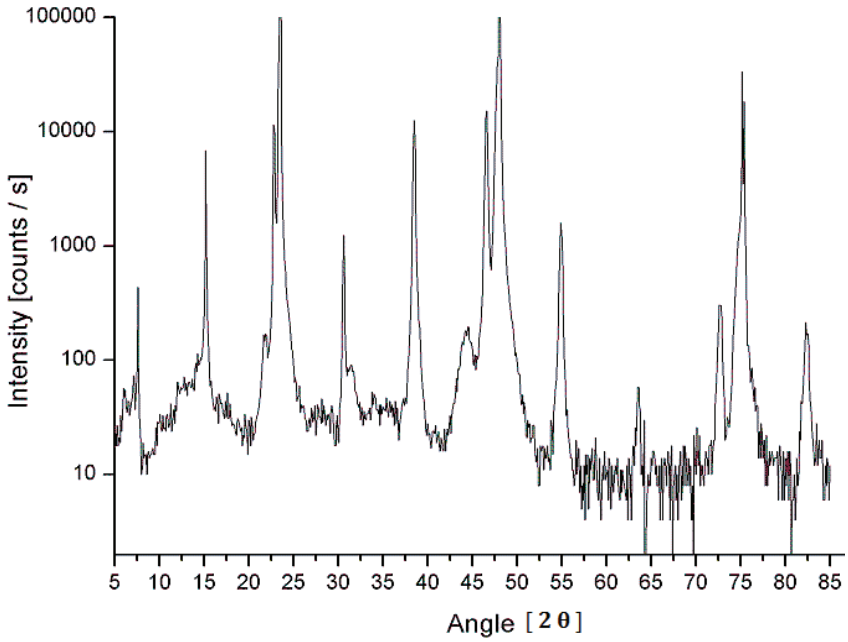

Figure 5.13: X-ray diffraction pattern of an YBCO thin film grown on a LAO substrate. (001) axis and other peaks illustrate that mixed-axis orientations are also present.

Figure 5.14: The damage on the surface of the old YBCO target.

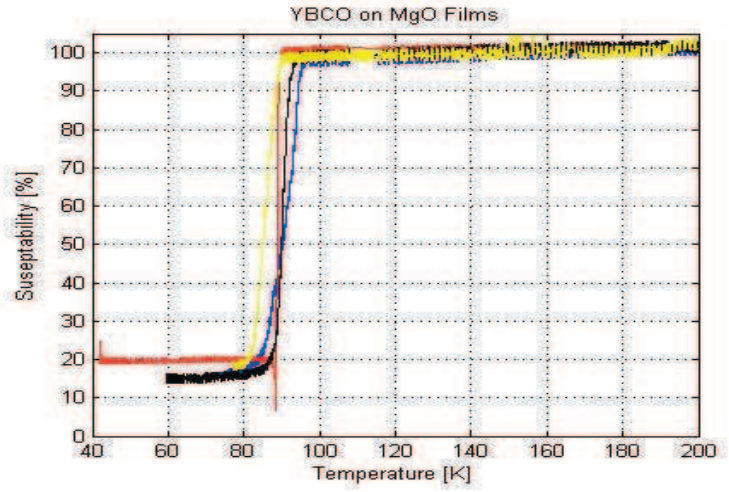

Figure 5.15: Susceptibility measurements on YBCO thin films deposited with the new target and the optimised ICM sputtering parameters.

5.2.2 Degradation of YBCO Tracks

The loss of the superconducting properties of Josephson junctions and electronic devices, such as SQUIDs, during processing is a major problem. Many students and researchers in our laboratory have experienced this problem. During our work we have faced the same problem and many samples have lost their superconductivity after they have been patterned into tracks.

In this regard, our troubleshooting steps searching for the reasons behind the phenomenon, will be explained, and how to prevent it in the future.

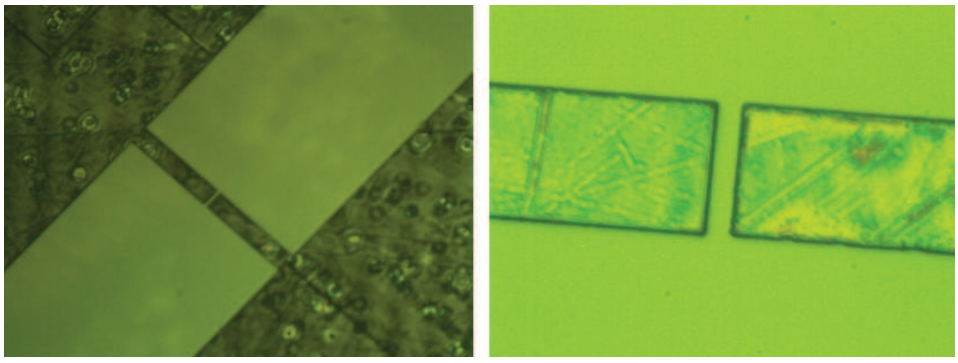

Figure 5.16: Optical microscope images of photoresist residue on top of the YBCO surface.

Initially, the photolithography process resulted in a photoresist residue on top of the YBCO surface, as is illustrated in Figure 5.16. To investigate the effect, photoresist was spun on an YBCO thin film, photolithography was performed, and then the sample was cleaned

with acetone to remove the photoresist. Thereafter, pads were deposited and a resistivity measurement was performed. The resistance of the film did not reach zero ohm below the critical temperature. There was a high contact resistance between the silver pads and the surface of the sample, even after the annealing step.

One of the important factors for a successful photolithography process is the energy of the UV light that is used for the exposure of the photoresist layer. Initially the reflector of the UV exposure unit was faulty, and had to be replaced, together with the UV lamp. This resulted in completely different results. No more photoresist residues on the exposed areas were observed, as can be seen in Figure 5.17.

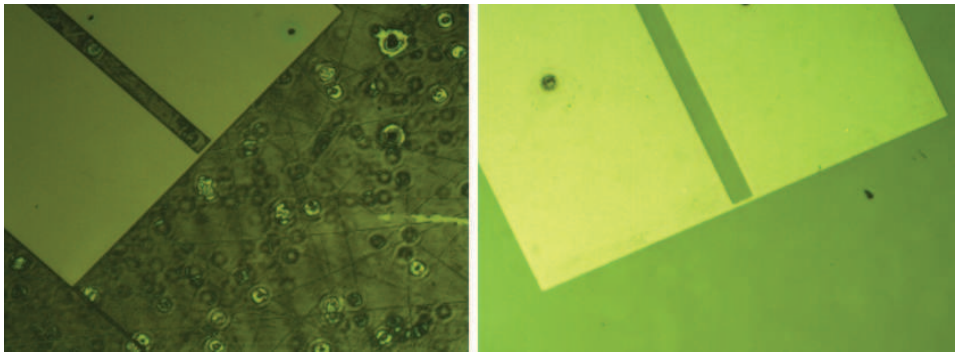

Figure 5.17: Results from the photolithography process before (left) and after (right) replacing the UV lamp and the UV reflector.

Resistivity measurements were performed on some of the new samples after the photoresist process was performed and the acetone cleaning process (prior to the etching process). Not surprisingly, the resistance between the pads reached zero ohms below the transition temperature (T_c) of the YBCO sample. A clean YBCO surface is thus very important to achieve a low contact resistance between the pads and the YBCO. It is, however, not clear if this was the reason for the samples losing superconductivity before.

The YBCO films were patterned into tracks, using two different acids, EDTA and citric acid. The mask and schematic drawing for the YBCO tracks, with the pads, are shown in Figure 5.18. In order to check the superconductive properties of the YBCO tracks, resistivity measurements were performed on the whole track, as well as between two neighbouring pads.

From Figure 5.19 it is clear that the superconductive properties of the tracks were damaged by the wet etching process. Even for neighbouring pads, the superconducting transition was wide and the resistivity only reached a zero reading at a very low temperature.

When measurements were done on the whole YBCO track, superconductivity was completely lost. Most of the damage was observed on the narrower portion of the track, and this was the probable reason for the loss of superconductivity.

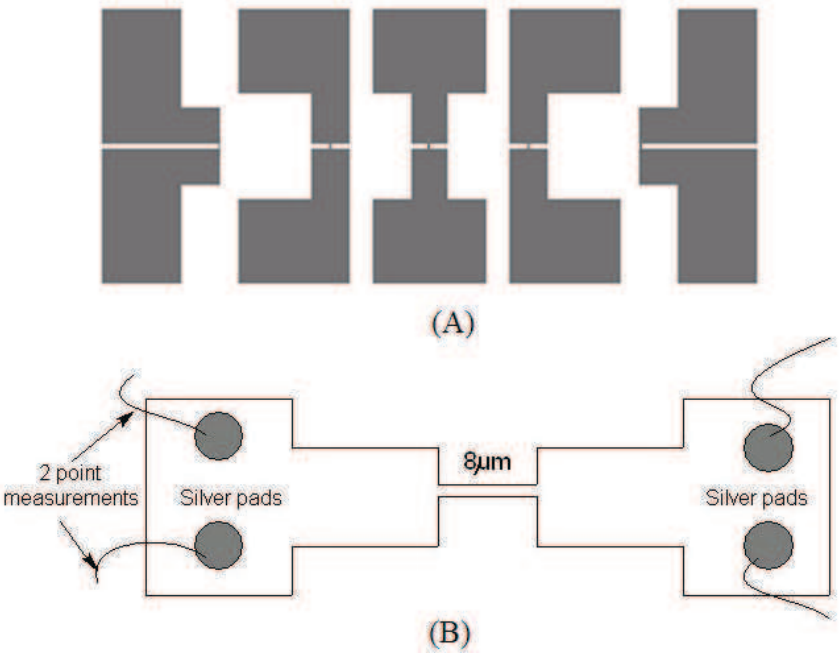

Figure 5.18: A) Schematic diagram of the mask for the YBCO tracks. B) Illustration of an YBCO track with silver pads, which are used for two- and four point probe resistivity measurements.

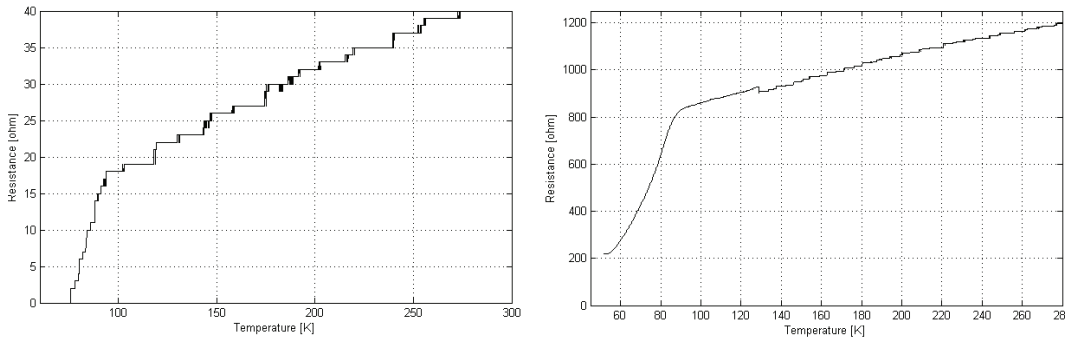

Figure 5.19: Left: Resistivity measurements between two neighbouring pads. Right: Four point probe resistivity measurements across YBCO track.

As an alternative to the wet etching process, argon ion-milling was used in a dry etching process. The defined pattern was transferred onto the YBCO samples. Silver pads were deposited on the patterned tracks, and resistivity measurements were then performed in order to check for any changes in the superconducting properties of the films.

As can be seen in Figure 5.20 the milling process also degraded the superconducting properties of the tracks. The figure shows the resistance versus temperature measurements of eight YBCO tracks from different samples. All the samples were deposited with the same ICM parameters. The resistance of the YCBO tracks never reached zero ohms for the majority

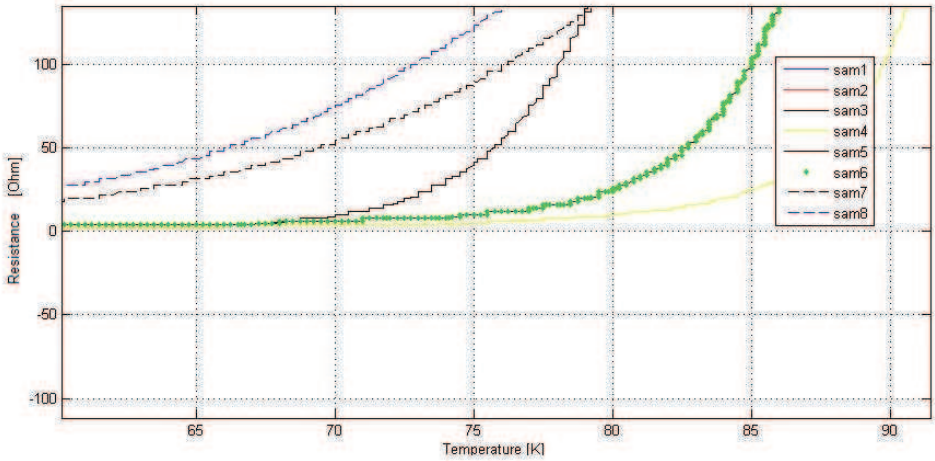

Figure 5.20: Resistivity measurements across YBCO tracks fabricated by a dry etching process. It is clear that dry etching also degrades the superconducting properties of the tracks.

of the samples. Therefore, both the wet- and dry etching processes led to a deterioration of the superconducting properties of the patterned YBCO.

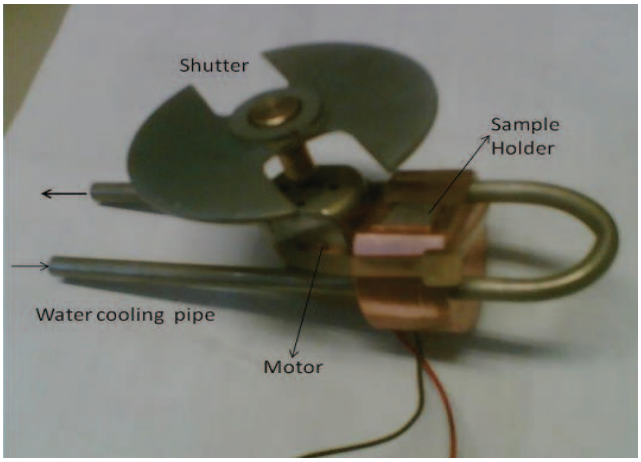

Figure 5.21: Modifications to sample holder, with added shutter on top.

Small modifications were thus also made to the dry etching system. A small shutter was added on top of the sample surface, as is shown in Figure 5.21. The shutter was rotated, using a small motor, which was biased by rectangular pulses. The sample surface was exposed to the accelerated ions for 4 seconds and was then covered by the shutter for the next 6 seconds. The water cooling pipes were placed very close to the sample, in order to optimise sample cooling. This ensured that very little degradation of the superconducting properties of the patterned microstructures and tracks occurred. This modification also

solved the problem of losing the superconducting properties of the fabricated devices in our laboratory, which has been reported by some students before.

The YBCO tracks that were dry etched by the modified system showed transition temperatures that were only a few Kelvin lower than the transition temperatures measured of the as-deposited YBCO thin films. The measurements on different YBCO tracks, deposited with the same ICM parameters, and etched with the modified system, are shown in Figure 5.22.

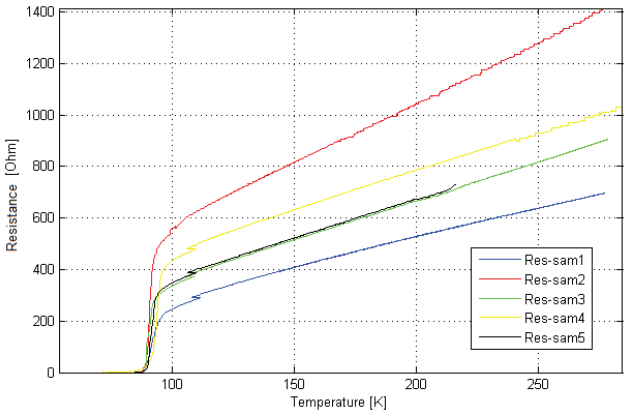

Figure 5.22: Resistivity measurements on YBCO tracks that were dry etched with the modified etching system.

5.2.3 Moisture Inside the Cold Finger

In order to test the characteristics of the YBCO tracks and devices, they have to be cooled in a cryostat. However, when the samples were removed from the cold finger after testing, moisture was formed on the sample surface, as is shown in Figure 5.23. The surface reaction between moisture and YBCO can cause a reduction in the Cu concentration inside the film, ultimately degrading the film properties and, most of the time, preventing the film from becoming superconductive.

This problem was very serious, and sometimes only one track from five could be tested or measured after the sample had been removed from the cold finger.

To prevent this problem, the roughing pump had to stay on until the temperature inside the cold finger had reached room temperature. Thereafter, the tested sample had to be cleaned with acetone, dried with N_2 gas and then stored with silica gel in a vacuum.

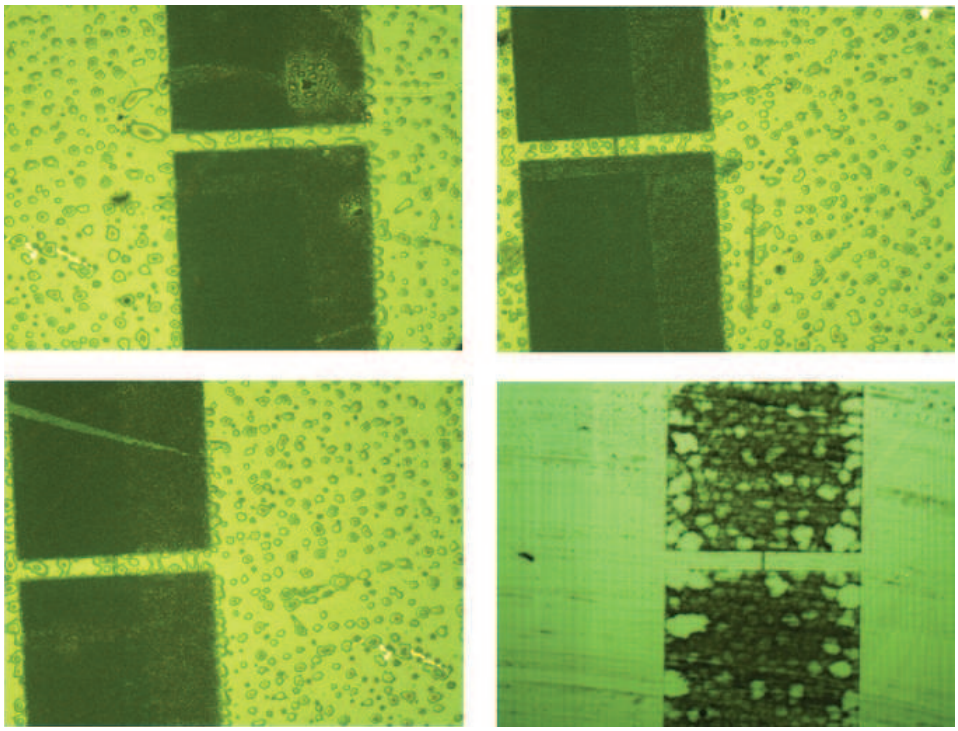

Figure 5.23: Optical microscope images showing the moisture on the surface of the YBCO samples.

5.2.4 Unsolved Problem

Most of our fabricated bridges became open circuits as soon as they were excited, using the Mr SQUID measurement unit. The devices were very sensitive, especially when the widths or the thicknesses of the bridges became narrower or thinner. Figure 5.24 shows few different type of bridges fabricated on different samples. the structure of the constricted or the ploughed bridges were destroyed and entirely deformed. The reasons behind the phenomenon, or how to avoid it, is still unclear. However, the same problem on planar sub-micron bridges made by electron-beam lithography was observed by researchers in Italy [99].

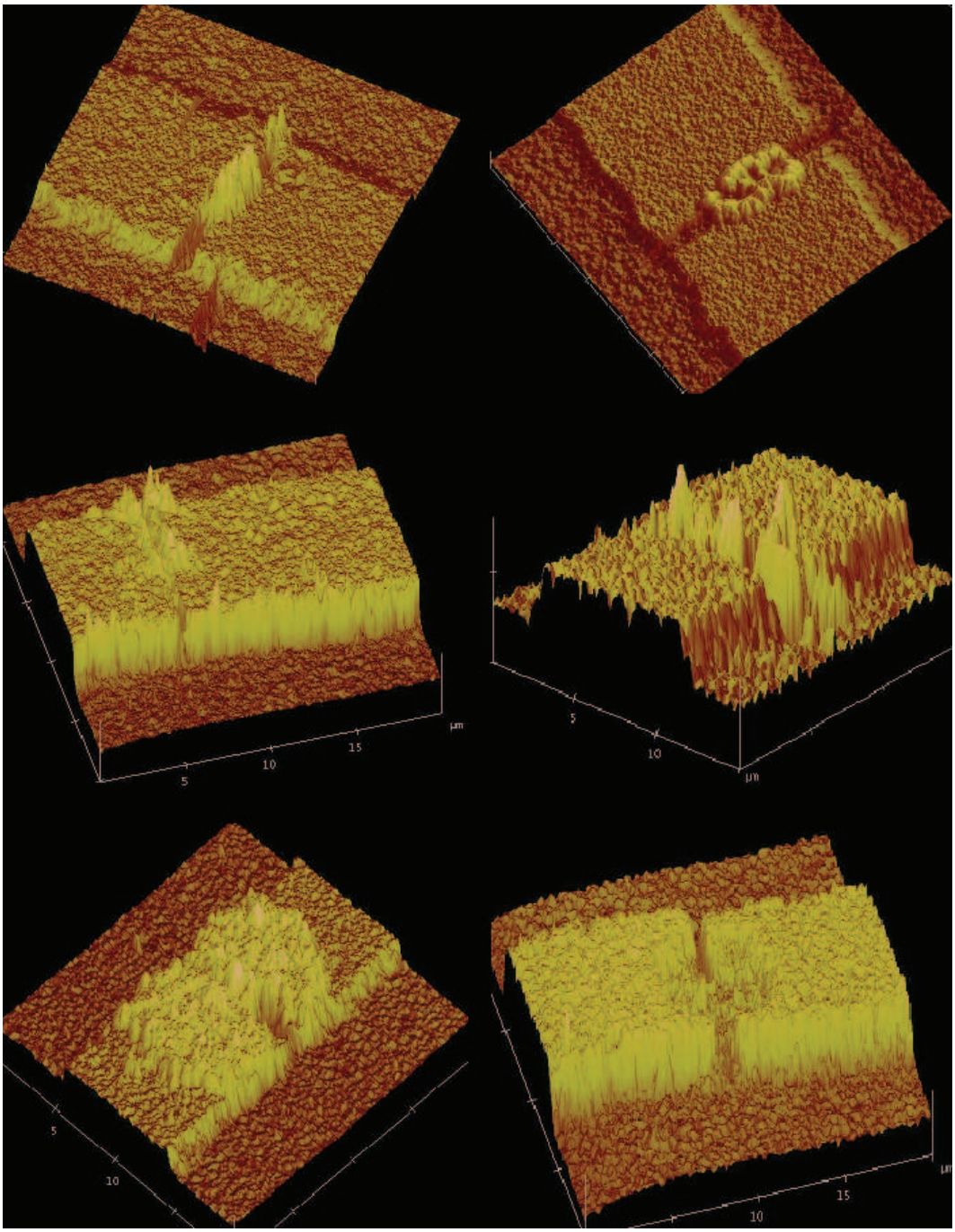

Figure 5.24: AFM images of the destroyed bridges fabricated by AFM nanolithography.

5.3 Measurement of Current-Voltage (I-V) Characteristics and the Observation of Shapiro Steps

Our first aim was to demonstrate the Josephson effect on micro-bridge structures that were fabricated by AFM nanolithography. A direct way of testing for the presence of the

Josephson effect is the generation of Shapiro steps on an I-V curve [See Appendix C.1 paper 1].

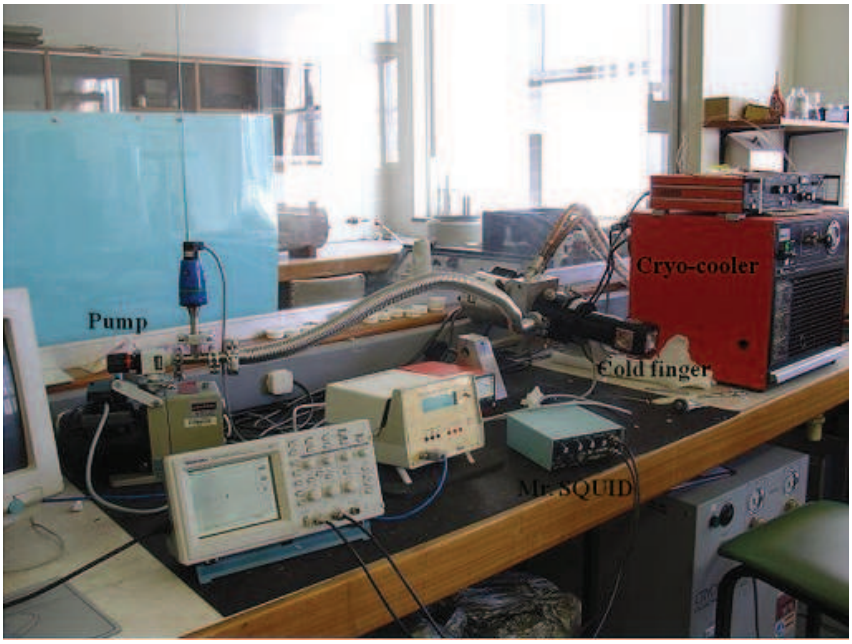

Figure 5.25: Cryocooler system for testing HTS circuits and devices.

In order to display the I-V curves of the junctions, a triangular current was applied to the bridge, using a Mr SQUID measurement unit [100]. A Mr SQUID unit can supply a triangular current waveform, which can be swept in the range from 0-3.5 mA. The unit also contains a low noise amplifier, which amplifies the measured voltage signal. The oscilloscope is set to the XY-display mode, and the triangular current is connected to one channel and the voltage across the bridge to the other.

To test the fabricated micro-bridges, the sample was placed on a copper base inside the cold finger of the cryo-unit, which is shown in Figure 5.25. The cold finger has four probe wires available to provide circuit excitation.

The I-V characteristics of a 3.6 μm width micro-plough, in the absence of microwave power, at 57 K are shown in Figure 5.26. The I-V curve showed flux-flow type behaviour. However, without microwave irradiation, constant current steps on the I-V curve, which can be proof of a flux-flow type junction, were not observed. Subharmonic steps in the I-V curve, which also can be proof of a flux-flow type junction [40], were also not observed.

From the I-V curve, the critical current was determined to be 1.58 mA at 47 K. This temperature was the lowest that the specific cryocooler could reach. The value of the normal resistance of the junction was calculated to be approximately 1.2 Ω, and the I_cR_n-product was 90 μV at 77 K.

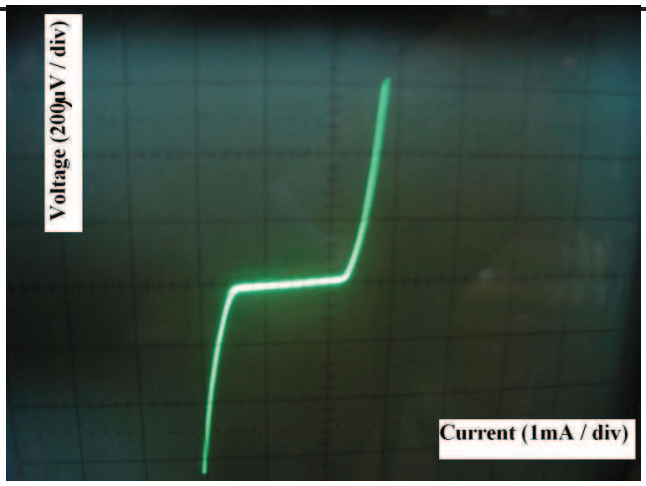

Figure 5.26: I-V curve of a fabricated 3.6 μm micro-plough constriction junction at 57 K in the absence of microwave excitation.

As a result of thermal fluctuations a rounding effect can be present in the I-V characteristics of a junction [5]. However, our I-V curves exhibit sharp knees, possibly ruling out any thermal fluctuation effects.

However, a mere observation of the expected I-V characteristics with DC excitation may not necessarily mean that the Josephson effect is truly demonstrated. In order to establish that, one should demonstrate both the DC and the AC Josephson effect, as well as the magnetic modulation of the critical currents.

We applied microwave power in the 2-18 GHz range via a coaxial cable, terminated with an antenna above the device. Well defined Shapiro steps were observed on the I-V curve at 10.225 GHz, as is demonstrated in Figure 5.27. The response of the constricted micro-bridge to microwave radiation (Shapiro steps) clearly gives positive evidence of the Josephson effect. This is because the observed step sizes satisfy (5.1), which can only be true for the fundamental Josephson effect.

The step sizes can be used to calculate the theoretical constant $\frac{e}{h}$. The voltage step is expressed as

$$V_0 = n(\frac{\Phi_0}{2\pi})w_s, \tag{5.1}$$

which is equivalent to

$$V_0 = n(\frac{hw_s}{4\pi e}) = n\frac{hf_s}{2e}, \tag{5.2}$$

where $\Phi_0 = \frac{h}{2e}$. This equation can be rewritten to yield the theoretical constant $\frac{e}{h} = 2.41796 \times 10^{14}$ Hz/V as

$$\frac{e}{h} = n(\frac{f_s}{2V_0}). \tag{5.3}$$

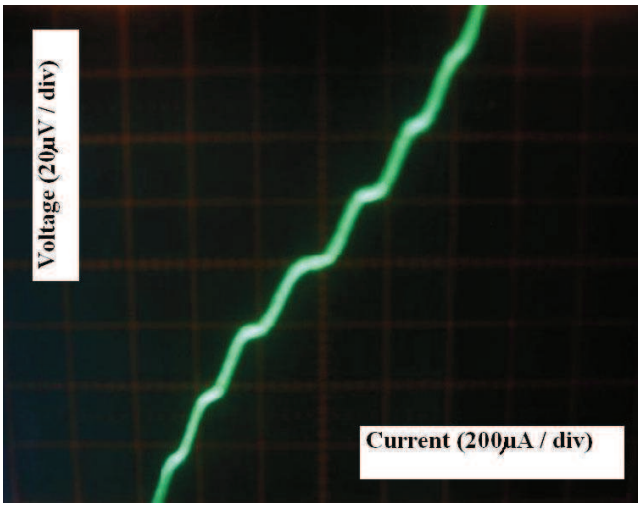

Figure 5.27: Observed Shapiro steps on the I-V curve of the micro-bridge junction after exposure to microwave radiation at a frequency of 10.225 GHz.

From Figure 5.27 the voltage V_0 was measured as approximately 21 μV, with some degree of uncertainty, and according to the test setup, the frequency was f_s=10.225GHz. Substitution of these values into (5.3) results in $\frac{e}{h} = 2.4345 \times 10^{14}$ Hz/V. This value corresponds quite well with the theoretically predicted value, constituting positive evidence for the Josephson effect.

At this stage we have to recall a deeper argument by Likharev [33], that similar voltage steps can occur due to the motion of Abrikosov vortices in a weak link, whose width is larger than a critical width W_c ($W_c/\xi \sim 4.4$), which is a few Angstrom. Therefore, with our constriction widths in the micron range, we are in a regime where $W_c/\xi > 4.4$, making the chances for the observation of Abrikosov vortex motion slim.

However, one should also note that Abrikosov vortex motion is only possible in a junction that is free of inhomogeneities [33]. Even small inhomogeneities will pin the fluxons, so that they cannot move.

In high-T_c cuprate superconductors, where the coherence length is very small, even a small defect can act as a pinning centre. From an experimental point of view it is very unlikely to deposit an YBCO thin film that will be absolutely free of inhomogeneities. These inhomogeneities, that naturally occur during the deposition of thin films, will pin any Abrikosov vortices and therefore there should not be any vortex motion.

In this scenario, we believe that the observed steps are more likely to be Shapiro steps than the steps due to Abrikosov vortex motion.

Some of our functional fabricated micro-bridge structures, when cooled below the critical temperature, were destroyed and turned into open circuit devices as soon as the bridges were excited with the Mr SQUID test unit. The YBCO layers in the micro-bridge region were changed and their entire crystal structure was displaced (see Section 5.2.4 for images). The same phenomenon has been observed by a research group in Italy [99]. They used electron-beam lithography to fabricate sub-micron junctions. They also found that bridges with small widths were very sensitive and became open circuits when they were tested. It is thus essential to handle these samples like one would handle sensitive CMOS ICs.

5.4 Magnetic Field Effect

The magnetic field dependence of the critical current gives important information about the spatial homogeneity of the Josephson current. In order to test that, two Helmholtz coils were added to the test setup. The coils were positioned to provide a DC magnetic field perpendicular to the bridges and perpendicular to the direction of the supercurrent flow.

Figure 5.28 shows the I-V characteristics of the three junctions that were tested for magnetic field modulations of the critical current. All the bridges were made on the same sample. The curves seem to follow RSJ type bridge behaviour, and not flux-flow type, as was observed for the first bridge junction (Figure 5.26) in Section 5.3.

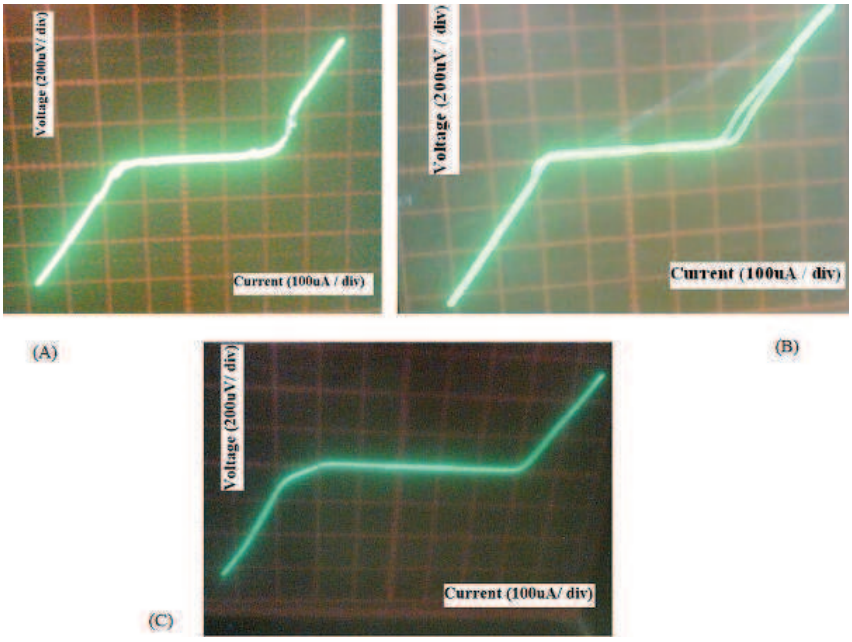

Figure 5.28: Measured I-V curves for fabricated micro-bridges with widths (A) 1.9 μm, (B) 3.1 μm, and (C) 4.1 μm.

Figure 5.29 shows the magnetic field modulation of critical current of the three different width bridges.

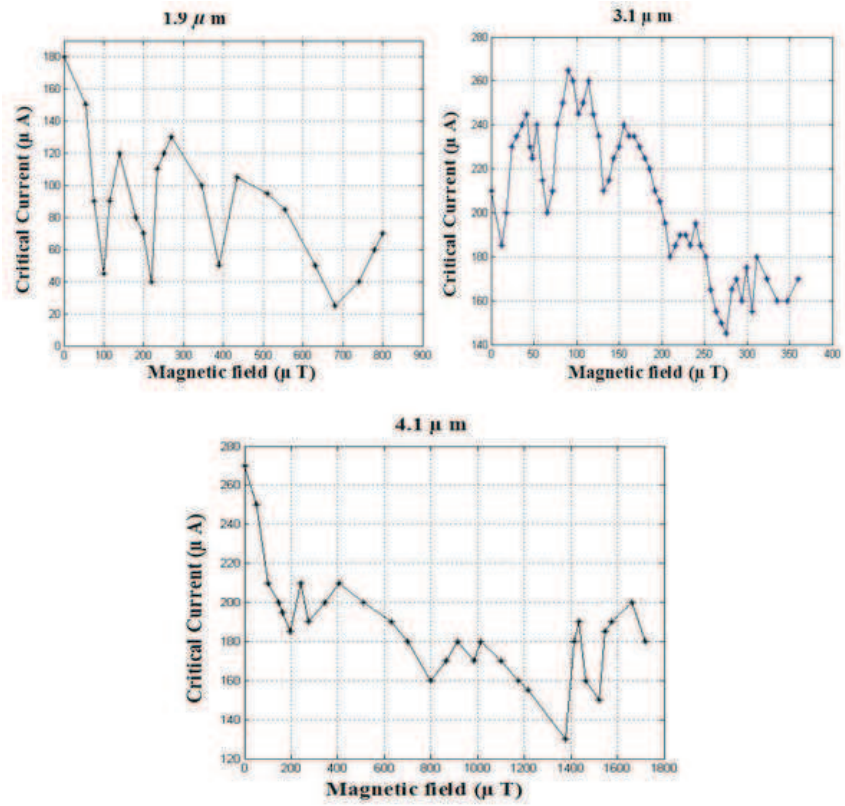

Figure 5.29: Measured critical current versus magnetic field relationship for micro-bridge junctions with different widths.

When an external magnetic field is applied to a uniform Josephson junction, a Fraunhofer-type of modulation of the critical current is expected. In our experiment, the magnetic field dependence on critical current shows a substantial modulation and variations in amplitude, which deviates from the ideal Fraunhofer diffraction pattern, that is expected in small junctions [101].

In all cases the critical current was not completely suppressed to zero. However, a suppression of the critical current by up to 84% was observed in the 1.9 μm wide bridge. The non-ideal critical current modulation by the magnetic field, the large amplitude of the side-peaks and the incomplete suppression of the critical current can possible be ascribed to the non-uniform current distribution over the junction, or the inhomogeneity of the bridge [See Appendix C.1, Paper 2].

5.5 Critical Current versus Temperature Characteristics

The measured temperature dependence of the critical current profiles of micro-bridges with different widths, are given in Figure 5.30. The critical current $I_c(T)$ shows a quasi-linear to a quasi-quadratic dependence on temperature, near the critical temperature. This relationship can be expressed as

$$I_c(T) \propto \left(1 - \frac{T_c}{T}\right)^x, \tag{5.4}$$

where x ranges from 1.2 to 2.

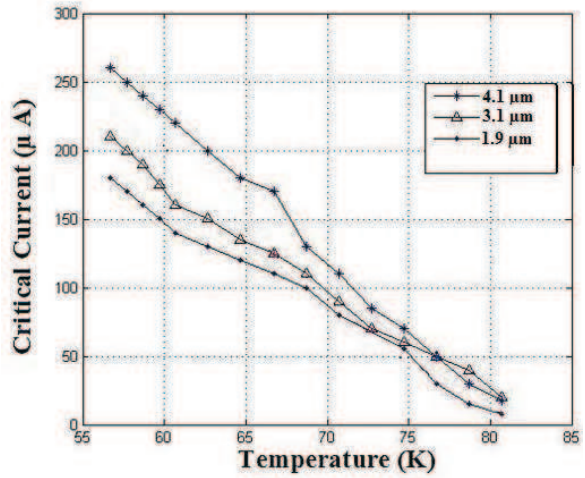

Figure 5.30: Measured critical current versus temperature profiles for fabricated micro-bridge junctions with different widths.

The quasi-linear dependence of critical current on temperature is typical for S-$\acute{S}$-S bridges [33], and the quasi-quadratic dependence of I_c on temperature is well know for S-N-S structures [5]. Therefore, it seems that our fabricated micro-bridge structures by AFM nano-lithography vary from S-$\acute{S}$-S structures to S-N-S structures.

The critical current of the micro-bridges, with widths of 1.9 μm, 3.1 μm and 4.1 μm, were measured as 180 μA, 210 μA and 260 μA respectively, at 57 K. The critical currents of the micro-bridges scales linearly with the dimensions of the bridges.

5.6 Micro-bridge Junction Behaviour on MgO and STO Substrates

To understand the substrate effect, we have fabricated micro-bridges on a number of MgO and STO substrates (see Figure 5.31). The measured results of the micro-bridges on MgO and STO give some insight into the natural behaviour of these planar junctions and the effect of the substrate materials on the critical current and Shapiro steps [See Appendix C.1, Paper 3].

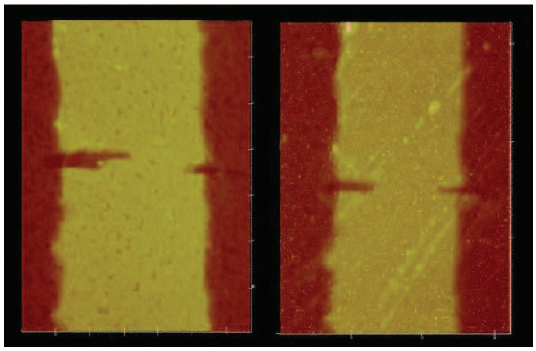

Figure 5.31: Micro-bridge junctions fabricated by AFM lithography on MgO- and STO substrates. The width of the bridge is 3.6 μm on MgO (left) and 3.2 μm on the STO substrate (right).

Figure 5.32 shows the measured I-V curves and Shapiro steps of two micro-bridges, fabricated on an MgO- and STO substrate respectively. Shapiro steps on the I-V curve of the junction on the MgO substrate was observed at a frequency $f_s = 8.1522$ GHz, with voltage step sizes of 17 μV. For the junction on the STO substrate the steps occurred at a frequency of $f_s = 9.6132$ GHz, with voltage step sizes of 20 μV. These values correspond quite well with the theoretically predicted value. As can be seen, the Shapiro steps of the junction on the STO substrate are not very clear, when compared to the well defined steps observed on the MgO substrate. It is known that STO substrates exhibit unpredictable microwave resonances in the range of temperatures from 60 K to 90 K [102]. These resonances can interfere with the observation of Shapiro steps. Our measurements, showing that micro-bridges fabricated on STO substrates show poor quality Shapiro steps, as compared to those on the MgO substrates, thus verify these findings.

Apart from the unclear Shapiro steps, the measured critical current is larger for the micro-bridge that was fabricated on the STO substrate.

STO has a very small lattice mismatch with YBCO (2%), but the substrate is unsuitable for high frequency applications due to its large dielectric constant (277 at room temperature). MgO, on the other hand, has a modest dielectric constant (9.65), it is readily available, and

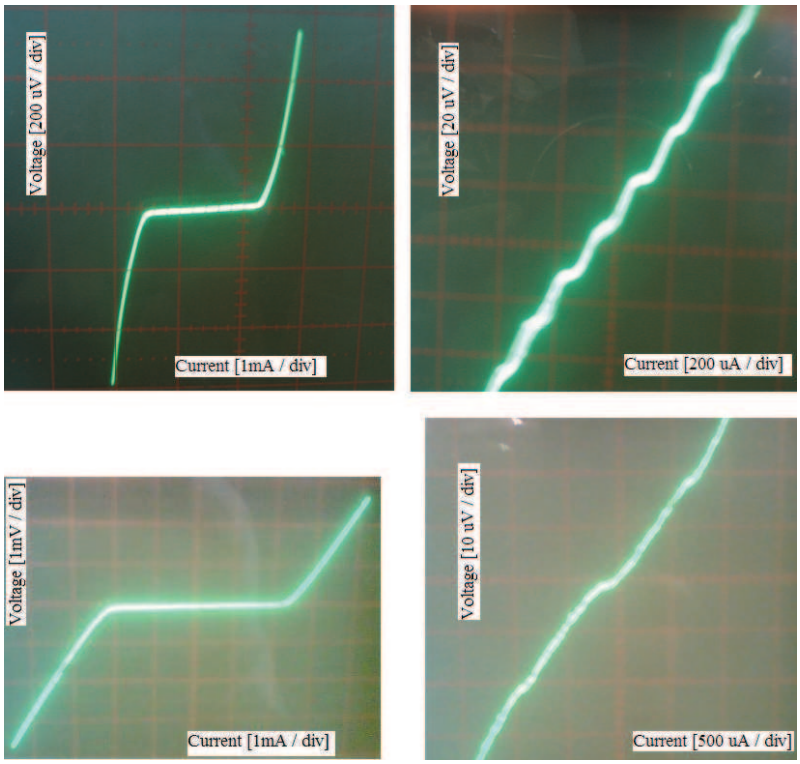

Figure 5.32: Measured I-V curves and Shapiro steps for the micro-bridge junctions on MgO- (top) and STO substrates (bottom), fabricated by AFM lithography.

has a 9% lattice mismatch with YBCO. The very low dielectric constant and the low cost make MgO substrates more suitable for junctions for high frequency applications.

5.7 Summary

This chapter presented all the required process steps for the fabrication of micro-bridges. The steps include HTS thin film deposition and analysis, photolithography, etching, pad deposition and AFM nanolithography. Laboratory challenges that were experienced during the course of the research were highlighted.

The second part of this chapter presented measurements and results on micro-bridges made by AFM nanolithography. This include I-V curve, Shapiro steps, magnetic field effects and the substrates effects.

Chapter 6

Nanoscale Variable Thickness Bridges: Josephson Effect and Critical Current Behaviour

We have fabricated nanoscale variable thickness bridge (VTB) structures on YBCO thin films using AFM lithography. To save time and space, the fabrication process steps, such as film deposition, photolithography, etching and pad deposition, will not be repeated here. More or less the same parameters and procedures were used as described in Chapter 5.

In this chapter, we will show results of the VTB fabrication processes, as well as the transport properties of these structures.

6.1 Fabrication of Nanoscale VTB Structures

YBCO thin films were deposited on MgO substrates. The thickness of the films were varied between 120 nm and 160 nm. An old YBCO target was replaced with a new one, because it had cracks on the surface, and some difficulties to ignite the plasma in the ICM chamber were experienced. Some sputtering parameters were also changed during the depositions with the new target.

Figure 6.1 shows the AFM image of the YBCO film surface. The surface roughness was less than 6 nm, and the very smooth film surface was excellent for the fabrication of superconducting Josephson junctions and devices.

X-ray diffraction measurements were performed to assess the crystalline quality, the phase composition and the purity, as well as the *c*-lattice parameter for annealed YBCO films. The pattern of a deposited YBCO film is shown in Figure 6.2.

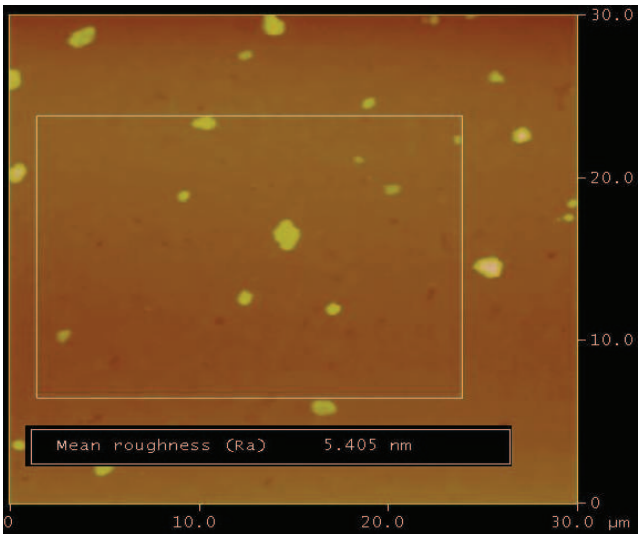

Figure 6.1: An AFM image of the smooth surface of the YBCO thin film, which was deposited by ICM sputtering on an MgO substrate.

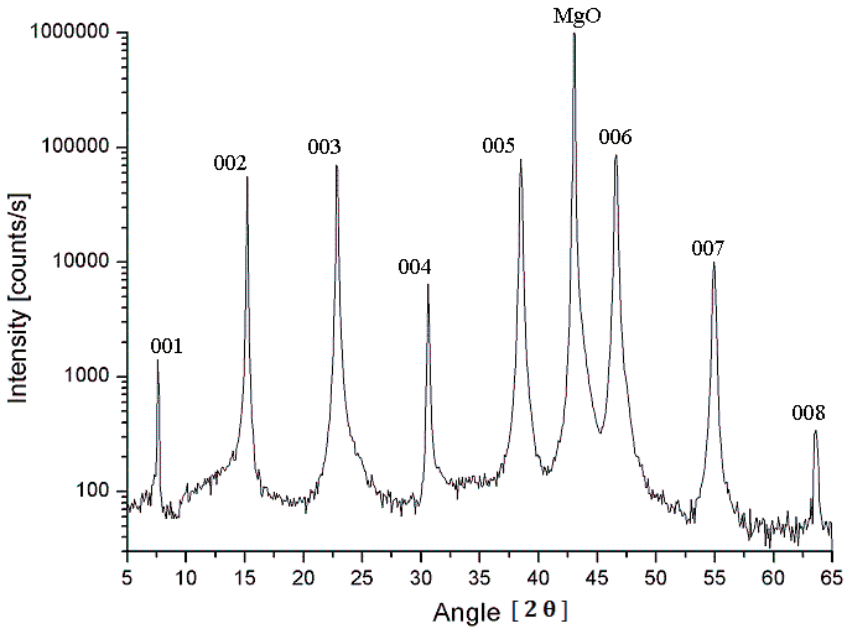

Figure 6.2: X-ray diffraction pattern of a deposited YBCO thin film on an MgO substrate.

Strong and sharp YBCO (001) peaks indicate a high degree of *c*-axis orientation. Non-off *a*-axis and non-off *b*-axis orientation peaks were observed in the pattern.

The superconducting properties of the as-grown YBCO films were characterised by AC susceptibility measurements. As shown in Figure 6.3 below, the film has a transition temperature of 89 K, with a transition width of (∼3 K).

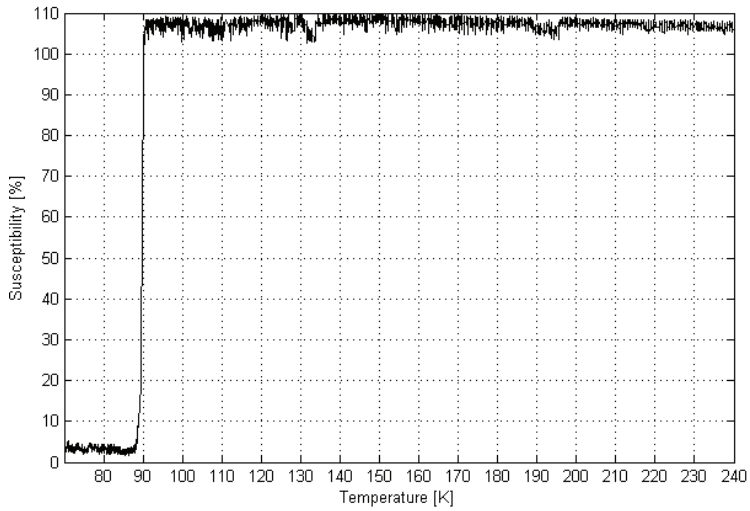

Figure 6.3: Susceptibility measurements on grown YBCO films showing the superconducting transition.

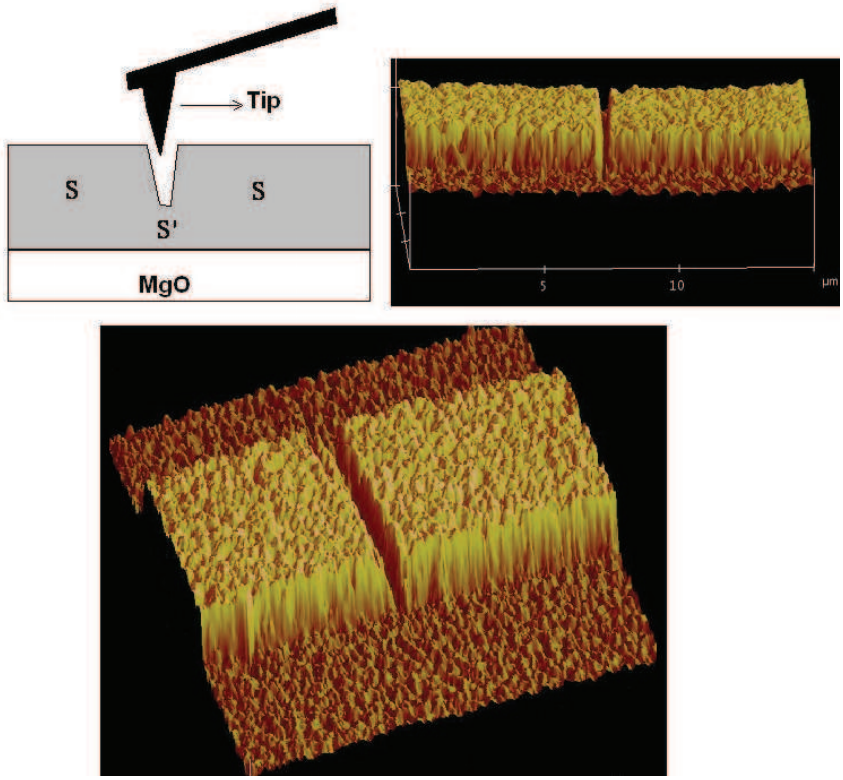

Figure 6.4: Illustration and images of a VTB structure fabricated using AFM lithography.

Photolithography, etching, and silver pad deposition steps were performed. Details can be found in Subsections 5.1.3 and 5.1.4, in Chapter 5.

In the AFM lithography process, a diamond coated tip was used as a cutting tool to define the plough. The tip was vertically displaced toward the YBCO surface, with a loading force of 11μN, which was sufficient for thinning the YBCO electrode. Thereafter, the tip was displaced over the width of the YBCO track for a few hundred cycles. By moving the tip, with the mentioned loading force, on the same line over the YBCO track, about 80-90% of the material was removed on average, leaving a 15-30 nm thick and 560-880 nm length variable thickness nano-bridge, as is shown in Figure 6.4.

6.2 Demonstration of the Josephson Effect

In order to test whether the fabricated constriction-type thickness bridges showed weak link behaviour, low-temperature transport measurements were performed, using the test setup shown in Figure 6.5. In particular, the current-voltage characteristics, microwave irradiation response, and the critical current as a function of temperature, were measured.

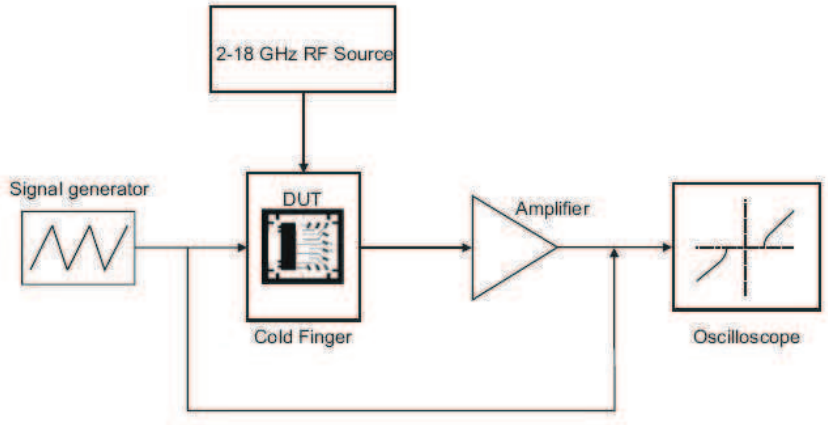

Figure 6.5: Schematic diagram of the measurement test setup for the fabricated junctions.

The sample was mounted on a PC board. Gold wires were bonded from the silver contact pads to the copper tracks on the PC board. The sample was then positioned inside the cold finger of the cryocooler unit, for testing.

The measured I-V curve of a 25 nm thick bridge is shown in Figure 6.6. No foot-like behaviour was observed in the I-V curves, at low voltages, in any of the measured VTB junctions, as is predicted by Aslamazov and Larkin [103], and typically observed in most low-temperature superconducting VTB bridges.

Since the bridge dimensions are much larger than the superconducting coherence length ξ_{ab} ≈1.5 nm, the VTB bridge type basically falls in the flux-flow regime [104]. However, from our point of view, the behaviour can also be due to the loading force on the tip damaging the YBCO crystal structure at the bridge region and form a weak link, or it can

alternatively be attributed to grain boundaries, which are naturally abundant in YBCO films, crossing the bridges [see appendix C.1 paper 4].

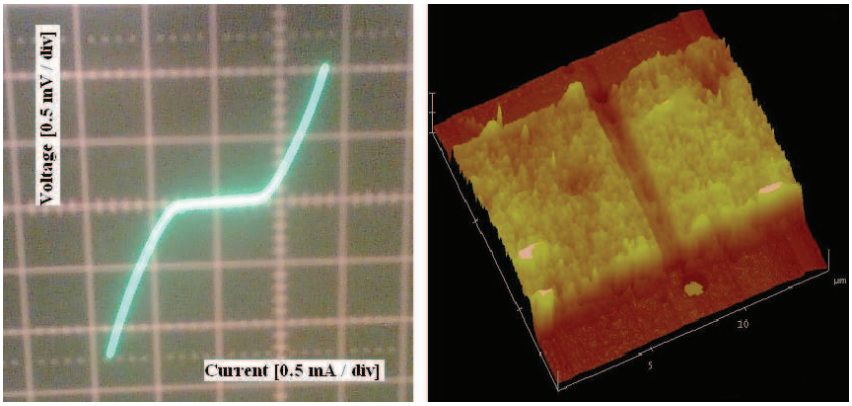

Figure 6.6: The measured I-V curve of a 25 nm thick VTB junction. An AFM image of the junction is shown on the right.

In order to identify the AC Josephson effect of the fabricated devices, measurements on the I-V characteristics of the VTB junctions were performed in the presence of external microwave power irradiation.

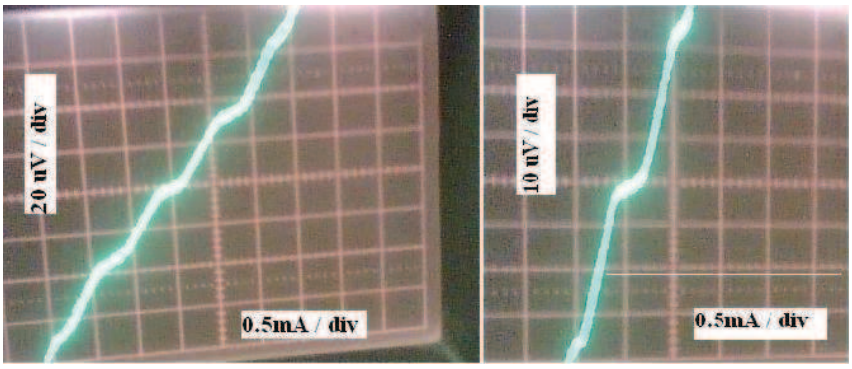

Figure 6.7: Measured Shapiro steps on the I-V curve after the VTB was exposed to microwave irradiation at a frequency of 15.383 GHz.

Microwave irradiation was applied in the 2-18 GHz range via a coaxial cable, terminated with an antenna above the device. Well defined Shapiro steps on the I-V curve were observed at a frequency of 15.383 GHz, as can be seen in Figure 6.7.

The measured voltage step (V_0) was about 32 μV, with some degree of uncertainty, as shown in Figure 6.7. This value satisfies the theoretically predicted value $\frac{e}{h} = 2.41796 \times 10^{14}$ Hz/V very well, which can only be derived from the fundamental Josephson effect.

The critical current versus temperature of the VTB was also measured, and is shown in Figure 6.8. The current relationship follows a quasi-linear dependence, which is typical for S-$\acute{S}$-S structures [33].

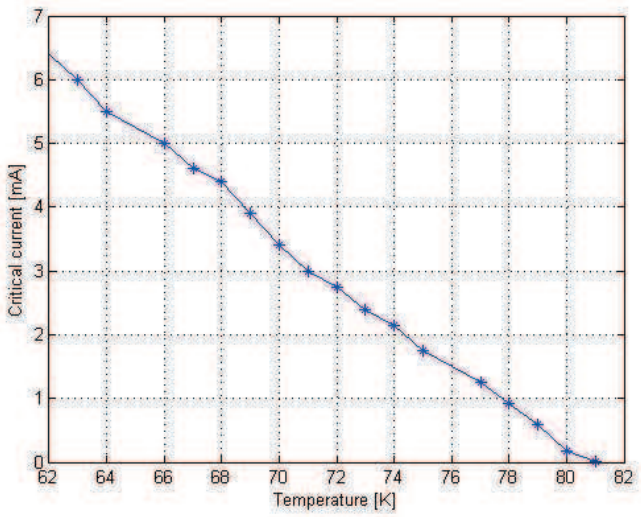

Figure 6.8: Temperature dependence of the critical current of the fabricated VTB.

6.3 Critical Current Dependency on Magnetic Fields

One of the most striking features of the behaviour of Josephson structures is the occurrence of diffraction and interference phenomena of supercurrents in the presence of externally applied magnetic fields. The magnetic field modulation of the critical current serves as a reliable indicator of the junction uniformity. However, perfect magnetic modulations can seldom be seen on HTS Josephson junctions, due to the intrinsic inhomogeneity of almost all types of HTS junctions.

A magnetic field was applied perpendicular to the VTB bridge, as well as perpendicular to the supercurrent direction. Figure 6.9 shows the behaviour of the critical current in the presence of the magnetic field. The current distribution and the critical current of the bridge were changed. The critical current was suppressed by the applied magnetic field and multiple peaks in the curve were observed [See Appendix C.1, Paper 4].

The critical current was quasi-periodically modulated by the applied magnetic field. Also, the magnetic flux minima did not occur at multiples of a flux quantum. In addition, the minima did not occur at zero current. These deviations from the ideal behaviour can be attributed to the presence of an asymmetric current density distribution in the junction.

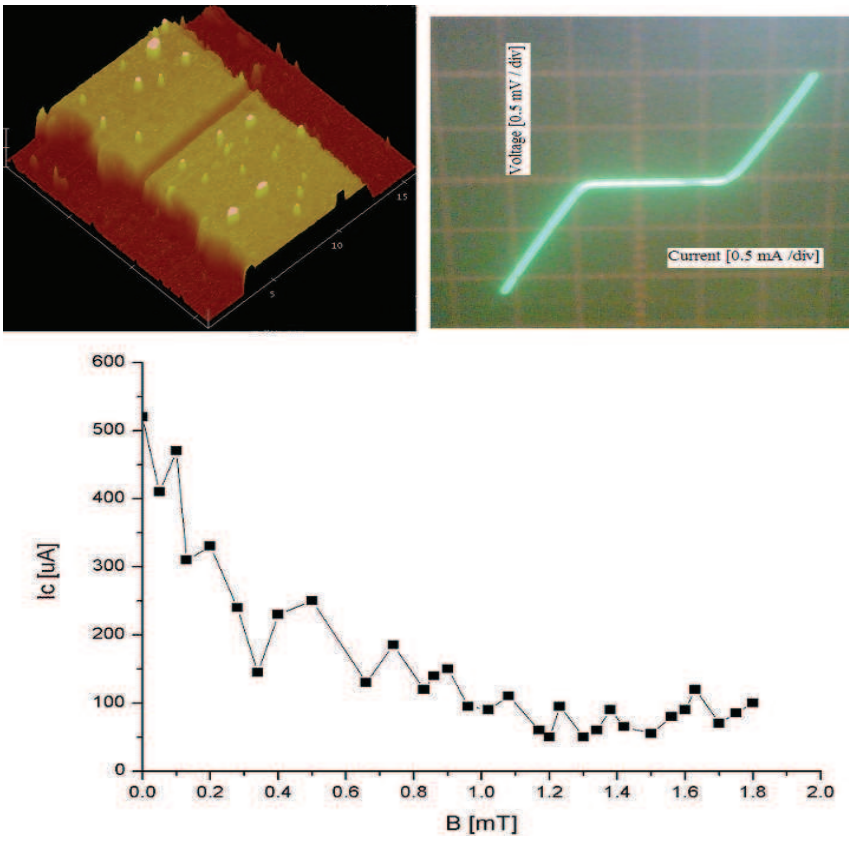

Figure 6.9: Top: AFM image and measured I-V curve of VTB junction. Bottom: Measured critical current versus magnetic field relationship for a 35 nm thick VTB bridge-type junction created by AFM lithography.

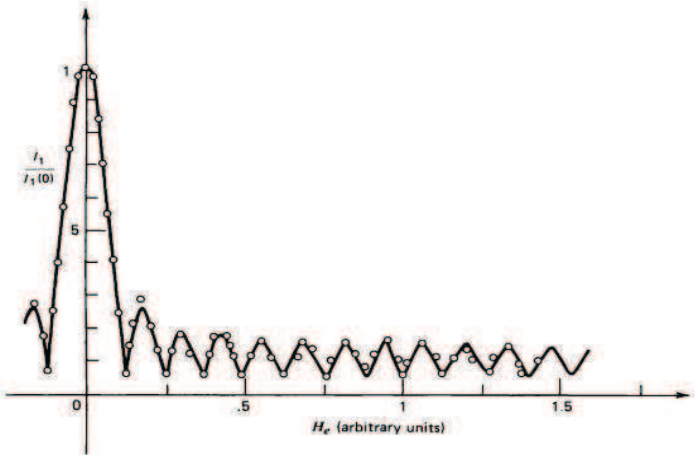

Figure 6.10: Magnetic field dependence of the critical current in a Pb-CdS-In tunnel junction, exhibiting small scale spatial fluctuations [5].

From our point of view, the deviation of the critical current modulation is due to the structural fluctuations effect, in which inhomogeneities are assumed to be randomly distributed all over the bridge region. Such an effect was demonstrated in Josephson tunnel junctions due to barrier non-uniformities [5] (see Figure 6.10).

6.4 Summary

This chapter presented the fabrication procedures of nanoscale VTB structures, made by AFM lithography. Results from AFM, XRD and susceptibility measurements were illustrated. Measured data for the DC and AC Josephson effect, as well as the critical current dependency on magnetic field, were also presented and discussed for these weak link structures.

Chapter 7

Fabrication of Nano-Constrictions: Measurement of the Josephson Effect.

In this chapter the fabrication steps for nano-constrictions on YBCO tracks are discussed. This is followed by a presentation and discussion of the experimental results. These results include measurements such as Shapiro steps, critical current versus temperature relationships, as well as magnetic field modulation of the critical current.

7.1 Introduction

Small Josephson junctions are gaining significance, due to their potential applications in qubit technology and nano-SQUID sensors.

- *Qubit perspective:* Josephson junctions are potentially good candidates for the fabrication of qubits and the design of quantum computers. The advantages of Josephson junctions as qubits are twofold. One is the potential for long coherence times, due to the low dissipation inherent to superconductors. The other one is that integrated circuit technology and micro-fabrication techniques can be used to fabricate superconducting circuits involving large numbers of Josephson junction qubits. In the perspective of qubit design, the Josephson junction is usually operated in the regime $E_c \sim E_j$ and $E_c \gg kT$, where E_c and E_j are the charging- and Josephson energy respectively. The first condition ensures that the Josephson junction is operated in the quantum

limit and the second one that the Josephson junction is being operated well above the noise threshold. These aspects are achieved when the Josephson junction size is reduced to nanoscale dimensions.

- *Nano-SQUIDs:* Advances in the fabrication of nanoscale SQUIDs (nano-SQUIDs) have opened up new measurement and detection possibilities with respect to the magnetisation of individual particles or molecular spins. In particular Bouchiat [63] has shown that, in the near field regime, the spin sensitivity (S_N) in terms of the number of spins detected, is expressed as $S_N = 4r\varphi_{ns}/\alpha\mu\mu_0 B$. Similarly the coupling limit is $\sim \mu_0 M/2r$. Both these aspects require the bridge dimensions to be as small as possible, preferably in the nanoscale range.

Planar nano-bridges, with dimensions smaller than the effective penetration depth, have been prepared in epitaxial YBCO thin films by means of AFM nanolithography. Although we have been able to demonstrate Josephson effects on only one nano-bridge structure, the measured I-V curve, Shapiro steps, and magnetic field modulation of the critical current, are still very useful for the study of this type of Josephson junction. All the other attempted nano-bridge structures became open circuits as soon as they were excited with the Mr SQUID test box (see Section 5.2 for images of some structured nano-bridges that became open circuits).

7.2 Fabrication Process for Nano-Constriction

Thin YBCO films (typical thickness 100 nm) were deposited on MgO substrates by DC inverted cylindrical magnetron sputtering, using the following parameters: Substrate temperature 740 °C, 1:1 Ar/O_2 mixture, total pressure 225 μHg, DC sputtering power 73 W. The resulting growth rate was relatively small (2.8 nm/min).

After the deposition the sample was cooled to 460 °C for 30 min, before it was cooled down to room temperature in pure oxygen at 1 bar.

Figure 7.1 shows the results of an AFM surface scan for an YBCO thin film. The surface was smooth with a typical surface roughness of 4-6 nm. Particles having a size of more than a few hundred nanometers in lateral dimension and few tens of nanometers in height are observed on the surface, as well as few large particles having diameters larger than 2 μm.

X-ray diffraction was used for sample characterisation. As can be seen in Figure 7.2. The samples exhibit the main peaks of a typical (001) *c*-axis orientation for superconducting orthorhombic structures. The strong intensities of the peaks indicate a well textured *c*-axis oriented grain structure.

The measurement of AC susceptibility as a function of temperature is often used to determine the transition temperature of superconductors. The curve of the susceptibility versus temperature for the deposited *c*-axis oriented YBCO thin film is shown in Figure 7.3.

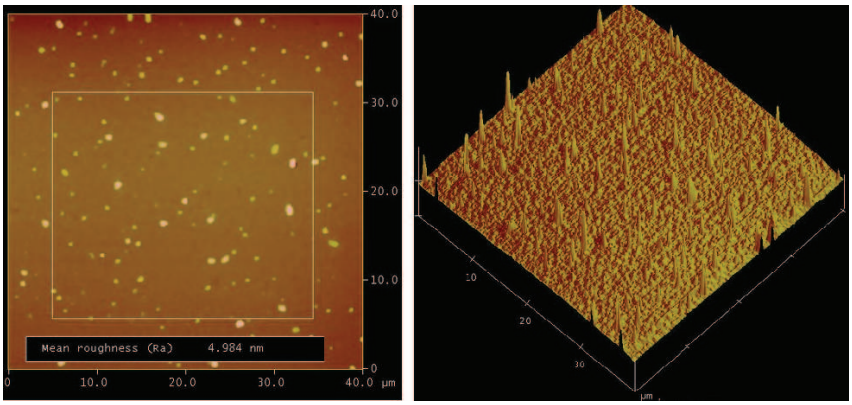

Figure 7.1: AFM images showing the YBCO surface morphology of the deposited films. The sample has a 4.98 nm surface roughness over a 25×25 μm area.

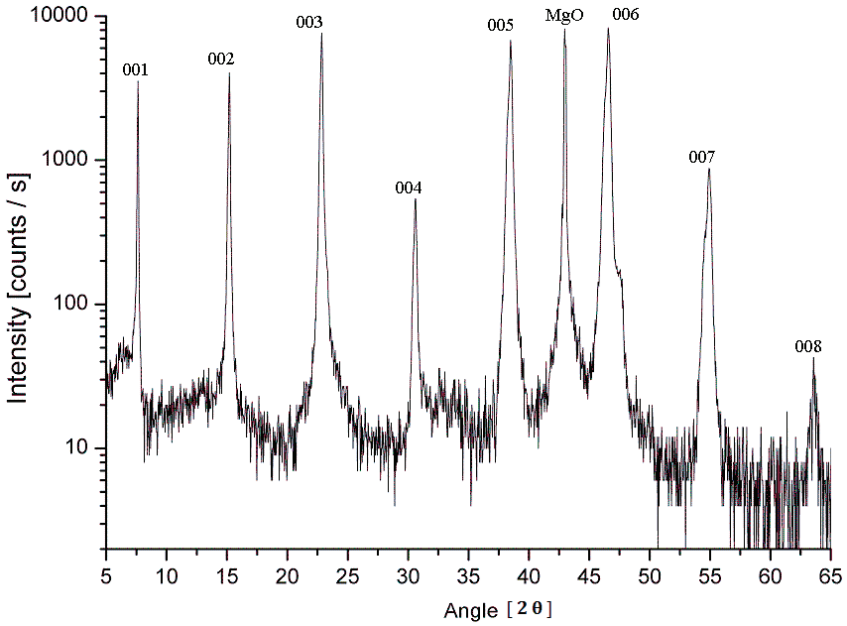

Figure 7.2: X-ray diffraction pattern for YBCO thin film grown on an MgO substrate at 740 °C.

Quite a sharp transition width of less than 3 K was measured, with an onset value of 89 K. This transition width and the high critical temperature are good indicators for very good quality YBCO thin films.

Each film was patterned into five tracks using a standard photolithography and argon ion-milling process. The widths of these tracks at the constriction regions varied from 6 μm to 10 μm. See Chapter 5 for more details.

Nano-bridges were fabricated on these tracks, using AFM ploughing. The AFM was operated in contact mode. The tip was vertically displaced onto the YBCO surface with a loading

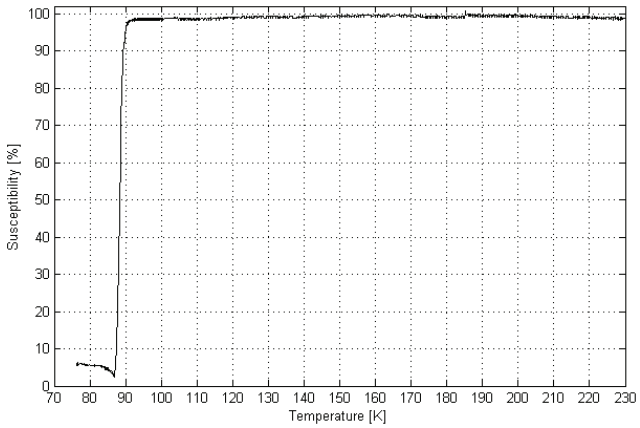

Figure 7.3: Measured susceptibility as a function of temperature for the deposited YBCO thin film.

force of 11 μN. This force was found to be sufficient to completely remove the YBCO material. To obtain a constriction width (W), the diamond coated tip was first placed at

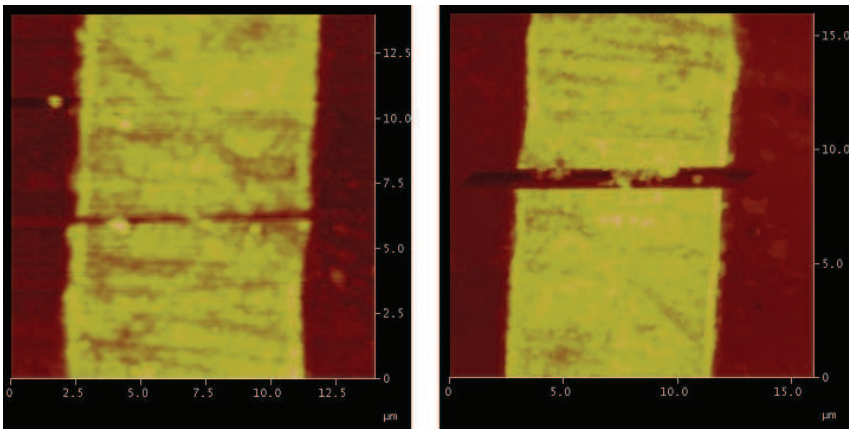

Figure 7.4: AFM images of YBCO nano-bridges fabricated by AFM nanolithography. The left image shows a bridge with a width of 490 nm and the right image a bridge with a width of 630 nm.

the centre of the track. The tip was then displaced by $W/2$ to the left side of the track. It was then driven into the YBCO film surface and ploughed on the same line till the left edge of the film was reached, back and forth for a few hundred cycles. The optimum tip velocity was 4 μm/s. The constriction is completed by applying the same ploughing process to the right side of the track. By adjusting and optimising the tip movement and the scan speed of the ploughing operation, constrictions of the desired width can be obtained. The YBCO residuals were cleaned by dipping the film in acetone and then into an ultrasonic bath for a few minutes. Typical nano-constrictions of constant thickness (≈100 nm) and widths of approxumately 490 nm and 630 nm are shown in Figure 7.4.

7.3 Josephson Behaviour in AFM Ploughed Nano Constrictions

To measure the I-V characteristics of the fabricated nano-bridges the Mr SQUID test setup was used. The sample was placed on a cold finger in a closed cycle cryostat. The DC I-V characteristics of the sample was measured and then a loop antenna from a microwave source was placed just above the sample, so that the I-V characteristics in the presence of microwave irradiation could also be measured. The applied power level was 3 dBm in the frequency range from 2-18 GHz.

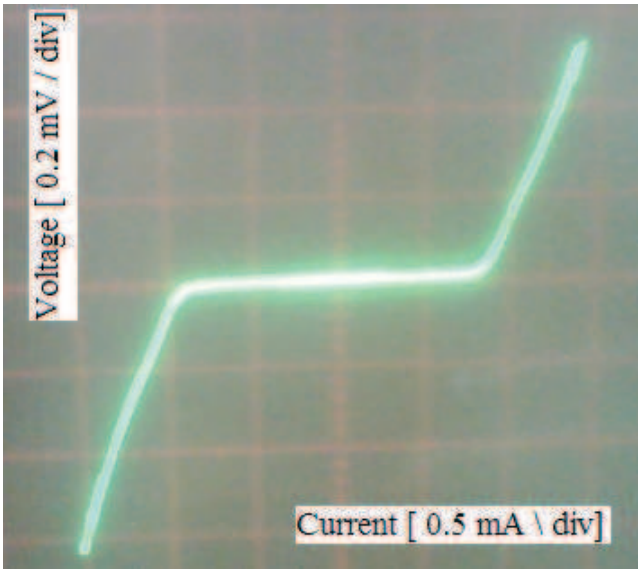

Figure 7.5: I-V characteristics (without microwave irradiation) of a 490 nm nano-constricted bridge, measured at 67 K.

The measured I-V characteristics (without microwave irradiation) of a 490 nm nano-constricted bridge is shown in Fig. 7.5, taken at a temperature of 67 K. Here, current is fed through the junction and the voltage drop across it is monitored. The critical current can be clearly be obseved. The I_cR_n-product at 77 K is measured as about 270 μV. For currents larger than the critical current I_c, a finite voltage drop appears across the junction, defined by its normal resistance $R_n = 1.1\ \Omega$. As the temperature decreases, the normal resistance increases.

At all measured temperatures, the bridge seemed to obey a flux-flow like I-V curve [See Appendix C.1 paper 4]. Such behaviour was demonstrated in nano-bridges made by focused ion-beam and electron-beam lithography. Flux-flow behaviour was also observed in low angle grain boundaries (LAGB) with less than 10° misorientation angles. However, the measured I-V characteristics of the nano-bridge did not show specific kinks and steps. Such kinks and steps can be attributed to discrete coherent vortex motion along single or multiple paths

across the bridge [70]. Instead, the observed I-V curve of the fabricated nano-bridge looked like true RSJ behaviour, but with thermal noise.

As a result of these thermal fluctuations a rounding effect was observed in the I-V curves at high temperatures. However, this effect became less pronounced as the bridge cooled down. The lowest measuring temperature possible with the specific cryocooler was 53 K. At very low temperatures (T <20 K) one would expect the characteristics to obey true RSJ behaviour.

Shiga *et al* [35] showed that the I-V characteristics of planar junctions made by focused ion-beam are strongly dependent on the fluence of the beam irradiation. The I-V curve can be either flux-flow or RSJ type, depending on the damage in the bridge region caused by the beam irradiation.

The response of the bridge to external microwave power irradiation was carried out by applying the microwave signal and observing the I-V characteristics over a wide range of frequencies.

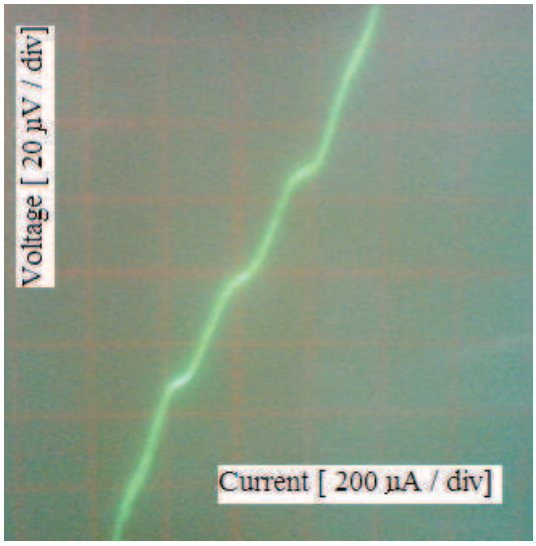

Figure 7.6: Measured I-V curve with Shapiro steps of the AFM lithography nano-bridge. The bridge was exposed to a 14.427 GHz microwave signal.

We have observed well defined Shapiro steps on the I-V curve at 14.427 GHz. The measured response of the nano-bridge to microwave radiation, shown in Figure 7.6, clearly gives positive evidence of the presence of the Josephson effect. The position of the steps is in agreement with the Josephson voltage-frequency relationship, the step sizes of 30 μV fit very well into the expression $\frac{e}{h} = \mathrm{n}\left(\frac{f_s}{2V_0}\right)$, yielding a value very close to 2.4179×10^{14} Hz/V, which is in good agreement with the text book value.

Based on Aslamazov-Larkin theory [57], Shapiro steps appear in the I-V characteristics under microwave irradiation in nano-bridges and can be explained by synchronisation of the

vortices' motion by the external microwave field. When a bridge is placed in a microwave field, the total current through the bridge is an alternating current superimposed on a dc bias, $I(t) = I_{dc} + I_{rf}sin(2\pi vt)$. Whenever this current exceeds I_0, vortices start to move in the bridge, which results in the development of a time-averaged voltage V. In the time intervals where the current through the bridge exceeds I_0, it has a normal component $I_n = I_{dc} + I_{rf}sin(2\pi vt) - I_0$. It is the interaction of this pulsatory normal current with the periodically moving vortices which finally produces constant voltage steps. Frequency locking occurs when the frequency nv of the nth harmonic of the microwave current is a multiple of the frequency of the motion of the vortices.

In order to study our fabricated nano-bridge further, we have measured the critical current versus the temperature over a wide range of temperatures. Figure 7.7 shows the temperature dependency of I_c. The critical current $I_c(T)$ follows a quasi-linear dependency near the critical temperature and can be approximated by $I_c(T) \sim (1 - T/T_c)$ over the wider temperature range. Similar $Ic(T)$ behaviour of nano-bridges, made by a focused ion-beam, was published by Lee *et al* [12]. The I-V characteristics showed typical RSJ type junction behaviour.

Flux-flow will result in a power law dependence ($I_c \sim [1-T/Tc]^v$). In the literature the value of v varies between 1 and 2 . In particular, Schneider *et al* [72] demonstrated that, in the flux-flow regime, the exponent for long nano-bridges (nano-constriction width, but length in micron range) is about 2. Our bridge is similar, and yet, does not show the expected power law behaviour, but rather a sraight line behaviour.

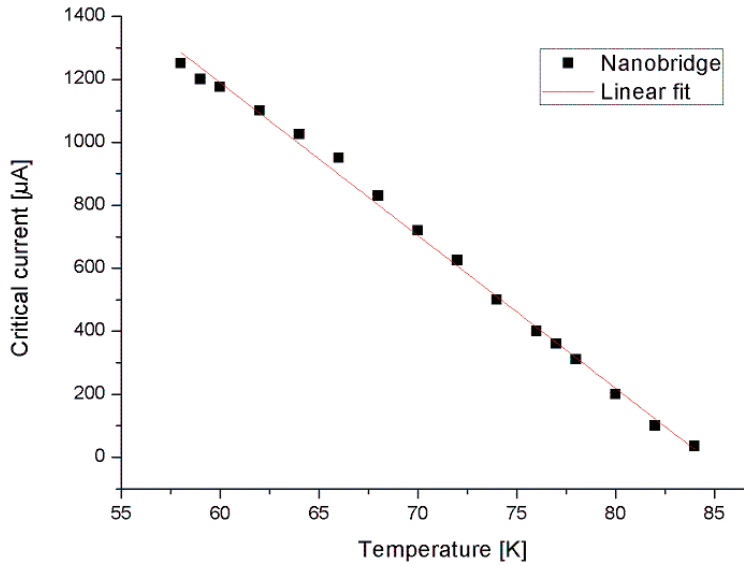

Figure 7.7: Measured critical current versus temperature relationship for the fabricated nano-bridge. The curve fit is quasi-linear.

To further understand the Josephson behaviour in our nano-constrictions, measurements

were done to determine the Ic dependence on the external magnetic field (B). We applied the uniform magnetic field perpendicular to the plane of the palnar nano bridge, using a Helmholtz coil setup. We can only do this one orientation of field with respect to the plane of the bridge in our experimental set up. A uniform junction will show the well known Fraunhofer behaviour.

Figure 7.8 shows the magnetic field dependency of I_c for the fabricated nano-bridge [See Appendix C.1, Paper 4]. Variations in amplitude were only taken over a single period, due to the limitations of the Helmholtz coils. As can be seen, it deviates from the ideal Fraunhofer diffraction pattern. The maximum applied magnetic field in our setup was 18 Gauss. Similar results were observed on break junctions [105]. The pattern, with non-zero minima, can be attributed to a variety of mechanisms, including non-uniform current density distribution along the junction width due to faceting and d-wave symmetry of the superconducting order parameter [106], and grain boundary barriers containing a high density of localised states.

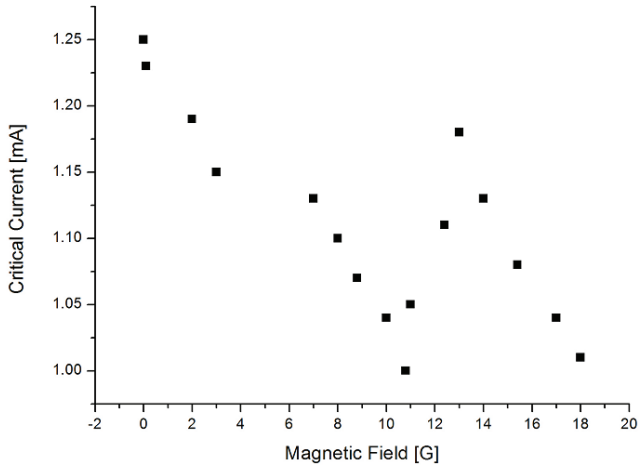

Figure 7.8: Measured critical current versus magnetic field relationship for the fabricated nano-bridge.

Nano-bridges with widths and lengths smaller than the effective penetration depth (λ_{eff}) are expected to show Josephson-like behaviour, as a result of coherent vortex motion. For perpendicular fields on these bridges, a field period $B = \Phi_0/(wl) \approx 0.0422$ T is estimated with w=490 nm and l=100 nm [107]. Since the experimentally found period of modulation in Figure 7.8 is much smaller, Josephson behaviour due to coherent vortex motion is unlikely the cause for the observed modulation in our nano-bridge.

From the relation $I_c \sim |sin(\Phi/\varphi_0)/(\Phi/\varphi_0)|$ and the bridge dimensions, for the field applied parallel to junction plane configuration, one can estimate the junction critical field ($H_{c||}$) at which the magnetic diffraction pattern goes through first zero. This happens when $\Phi LW = \varphi_0$. With measured L=660 nm and W=490 nm, and $\varphi = 2.07 \times 10^7$ Gauss/cm^2, we estimate the junction critical field to be $\sim$ 60 Gauss. However the measured value is $\sim$

11 Gauss. This is about 6 times less than the estimated value for the parallel configuration. This discrepancy can be explained by the recent advances made by Monaco et al [108] on the effect of orientation of the field with respect to the plane of the junction. We should note that in our experimental set up we applied field perperndicular to the palne of the bridge. In this configuration the applied magnetic field is more effective in modulating the critical current. This is because of the screening currents induced by the transverse field that circulate on the borders of the film surface.

In the case of Nb/Al/Nb planar overlap type Josephson tunnel junctions it was found that junction critical field $H_{c\perp}$ is much less than the $H_{c||}$ [108]. The ratio $H_{c||}/H_{c\perp}$ is varying between 30 to 13 depending on the J_c of the junction. For high critical current density junctions, this ratio is small. Though this analysis has been developed for planar overlap type low T_c Josephson tunnel junctions, we believe that the physics is similar in our nano bridges and that the measured $H_{c\perp} = 11$ Gauss is about 6 times (let us call it reduction factor) smaller than the estimated ~ 60 Gauss, which can be understood in the model of Monaco et al. At this stage exact estimation of the reduction factor is not possible from the model of Monaco et al.

As far as we are concerned, we are the first research group to demonstrate Josephson effects on a nano-bridge made by AFM nanolithography. Using the AFM ploughing technique, we have fabricated a nano-bridge on a high-T_c YBCO superconducting thin film, which can be operated at liquid nitrogen temperatures. We demonstrated positive evidence of the Josephson effect in the bridge by measuring Shapiro steps. Josephson effects are often confused with parallel effects coming from flux-flow phenomena. However, our I_c versus temperature data, with clear linear behaviour as opposed to the power law behaviour for flux-flow, and the pattern of I_c versus B, both rule out flux-flow behaviour in our bridge.

7.4 Summary

This chapter presented the fabrication process of planar nano-bridges on HTS YBCO. The chapter also provided measured results for the fabricated Josephson junction. The I-V characteristics were presented and interpreted. The results showed very good junction behaviour, including the critical current versus temperature relationship, Shapiro steps and the magnetic field modulation of the critical current.

Chapter 8

Conclusions and Future Work

This chapter gives a general overview of the research presented in this thesis, emphasising the important accomplishments, and outlining the possibilities and new ideas for future researcher.

8.1 Dissertation Overview

Chapter 1 gave a brief introduction to Josephson junctions and device applications, followed by a motivation to manufacture planar weak link structures.

The fundamental derivation of Josephson effects in SIS structures were discussed in Chapter 2. It was followed by the theoretical background of lumped and generalised Josephson junctions. A suitable model to describe superconductive tunnelling junctions were given. The RSJ model was developed to determine the response of a junction to various values of the damping parameter. The response of Josephson junctions to microwave irradiation (Shapiro steps), the effect of external magnetic fields on the critical currents of junctions, as well as the thermal fluctuation effect on the current-voltage curves of Josephson junctions, were all studied. The chapter concluded with an introduction to high-temperature superconducting Josephson junctions.

A literature study on superconducting weak links was given in Chapter 3. The Josephson effect in those structures, fabrication methods and some parameters of weak link structures, especially in micro-bridges, variable-thickness bridges and nano-bridges, were introduced.

Chapter 4 was divided into two parts, namely YBCO thin film deposition and patterning, and thin film characterisation. The first part included discussions on the YBCO crystal structure and its superconducting phase, thin film growth modes, introduction of the most common substrates used for YBCO thin film growth, sputtering systems, the locally made inverted cylindrical magnetron sputtering system for the deposition of YBCO thin films,

and patterning processes,including photolithography and etching. The second part of the chapter provided an overview of the analysis techniques to characterise film quality. This included the X-ray diffraction technique, the operation of an atomic force microscope and its application to perform nanolithography, and resistivity and susceptibility testing.

Experimental results are given and discussed in three chapters, dealing with micro-bridges, variable thickness bridges and nano-bridges respectively. In Chapter 5 all the required process steps for the fabrication of micro-bridges were given in detail. The parameters that were used in every single process step were illustrated, including HTS thin film deposition and analysis, photolithography, etching and pad deposition, and AFM nanolithography. The chapter also addressed most of the laboratory challenges and problems that were faced during the research. The second part of the chapter showed and analysed the test results of the planar micro-bridge structures, investigating the Josephson effect behaviour in them.

In the same manner, Chapter 6 and 7 showed the fabrication, measurements, analyses and results on VTB and nano-bridge junctions respectively. Results from I-V characteristics, microwave irradiation and magnetic field effects were illustrated, and physical interpretation of the results were given to understand the behaviour of the fabricated structures.

8.2 Conclusion

The body of work and the results presented in this dissertation demonstrate the contributions that were made to HTS research at Stellenbosch University. These contributions include:

- *Improved photolithography processes.* Extremely good photolithography results were achieved after the UV light and the UV reflector were replaced. The optimum parameters for the process were documented for current and future students and researchers.
- *Solution to the superconductivity degradation problem.* The argon ion-milling system was modified to produce better yield. The samples were positioned to be very close to the water cooling pipes in order to keep them cool during the etching process. In addition, the etching time was periodically applied (4 seconds on and 6 seconds off) in order to provide further cooling. This modification helped to prevent the degradation of the superconducting properties of our YBCO tracks on the samples.
- *Deposition of Silver Pads.* Silver pads can be evaporated and annealed, by using the thermal evaporation system. This method is much easier than using the PLD technique for gold deposition.
- *Computer controlled AFM nanolithography.* The movement of the diamond coated AFM tips were placed under full computer control. The tips can be displaced with the desired speed in any direction, allowing one to scratch, modify or cut any region on the sample surface. The AFM nanolithography described in this dissertation can thus be used to fabricate or modify various structures on different materials.

- *An intergrated fabrication process.* The entire fabrication process has been documented, allowing similar devices to be fabricated in the future. This contributes towards the future implementation of practical devices based on the same prototype.

AFM imaging and XRD analyses were performed on the fabricated YBCO thin films. Using the optimised parameter sets, the results have shown that the superconducting YBCO thin films are very smooth, uniform, and crystalline with the desired orientation. Such films can be used for the fabrication of practical superconducting elements and devices.

The results of an experimental study of micro-bridge weak link structures, fabricated using AFM nanolithography, have been presented. The first measurements were performed on a 3.6 μm wide micro-bridge. The results successfully demonstrate both DC and AC Josephson effects in the structure. The voltage step values correspond well with the predicted theoretical constant for Shapiro-steps.

The magnetic field modulation of the critical current was measured for micro-bridges with different widths. The narrowest bridge width tested was about 1.9 μm. The magnetic field dependence of the critical current showed a substantial modulation and variations in amplitude, which deviated from the ideal Fraunhofer diffraction pattern that is expected in small uniform junctions.

The I-V curves of the fabricated micro-bridges varied from one bridge to another, from flux-flow to RSJ type. The only difference in the structures' fabrication process were the tip loading force, which varied from one diamond coated tip to the other, as well as the number of ploughing cycles. This could have changed the degree of damage of the remaining YBCO in the bridge regions.

The measured critical currents $I_c(T)$ of our micro-bridges followed a quasi-linear to a quasi-quadratic dependence with respect to temperature near the critical temperature.

Results from the fabricated constriction-type thickness bridges were also presented. With less than a 15 nm thickness plough, variable thickness bridges acted as real weak links. Low-temperature transport measurements illustrated the Josephson effects in VTB structures. I-V characteristics, Shapiro steps, and the suppression of critical current by magnetic field irradiation demonstrated the existence of Josephson junctions in the fabricated VTB junctions. However, the observed deviation of the critical current modulation with respect to an applied magnetic field, can possibly be ascribed to the structural fluctuations effect, in which inhomogeneities are assumed to be randomly distributed all over the bridge region. Measurements of the relationship of the critical current on temperature, showed a quasi-linear dependency. Such behaviour is typical for S-$\acute{S}$-S type structures.

We have also successfully fabricated nano-bridges on YBCO thin films using AFM nanolithography. However, we could only do measurements on one bridge, due to the fact that the other fabricated nano-bridges became open circuits during the bridge excitation process.

The measurements on this nano-bridge demonstrated the Josephson effects. At all measured temperatures the I-V curves of the bridge seemed to exhibit RSJ-, and not a flux-flow like behaviour. Other researchers have demonstrated flux-flow behaviour in nano-bridges made by focused ion-beam and electron-beam lithography.

We have observed well defined Shapiro steps on the I-V curve at a frequency of 14.427 GHz. The voltage step height value corresponded quite well with the theoretically predicted value.

In the presence of an externally applied magnetic field perpendicular to the bridge, we have observed variations in amplitude over a single period, which deviated from the ideal Fraunhofer diffraction pattern in that the minima did not reach zero. The pattern with non-zero minima can been attributed to a variety of mechanisms, including non-uniform current density distribution along the junction width, and grain boundary barriers containing a high density of localised states.

The only drawback of the AFM lithography technique was the gradual degradation of the expensive diamond coated tips. At present AFM tips made of pure diamond have become available on the market. These tips can be reshaped and fixed, and it will be a good alternative in future research.

Although many of the fabricated bridges, including micro-, nano-bridges and VTB structures, turned to open circuits during measurement procedures, the results which were supplied in the chapters demonstrate that the original aim of this work was successfully achieved. This provides a strong foundation for the application of the AFM nanolithography technique to fabricate practical Josephson junctions for future applications.

8.3 Recommendations and Future Work

During the execution of the research numerous challenges and problems in the laboratory were solved. A substantial amount of time was spent during the research towards the fabrication of functioning devices made by AFM lithography. However, a number of challenges remain to increase the yield and to make useful devices for practical applications.

- The ICM chamber should always stay clean under vacuum. The YBCO target has to be stored in a proper place under vacuum conditions, as oxidation of the target surface could effect the sputtering parameters, as well as the properties of the deposited YBCO films.
- Argon ion-milling reproducibility is still poor. The etching times of samples with the same thickness sometimes differed quite substantially. It seems as if the number of accelerated electrons in the chamber is different every time.
- The test setup needs to be improved in order to allow for more reliable measurements to be performed and much better results to be achieved. The cryocooler is designed to cool down to 37 K or below, however, the lowest temperature that can be reached

at present is 49 K or higher. A new Helmholtz coil is required to generate stronger magnetic fields for the magnetic field modulation of critical current measurements. Shields for noise and the earth's magnetic field need to be improved in order to achieve clearer results, as well as to be able to perform some measurements on very high sensitivity devices, such as SQUID magnetometers.

- Additional techniques, including SEM, need to be available in order to investigate and study the YBCO bridge structures after patterning has been completed. This will help to identify the type of the weak link structure made by AFM lithography.
- Alternative equipment for the excitation of the test current for the measurement of I-V characteristics should be considered. This could minimise damage to the sensitive bridge structures.
- Implementation of these bridges for practical device applications, such as SQUID magnetometers or gradiometers, should be investigated.

Apart from the results presented in this dissertation, there remains a vast number of unanswered questions that need to be explored with regard to the fabrication of Josephson junctions and devices, using AFM lithography. It is my wish that the knowledge that has been gained and that has been presented in this dissertation will be applied in future work to further improve the impact of local researchers on the international research community.

Bibliography

[1] Ambegaokar, V. and Halperin, B.: Voltage due to thermal noise in the DC Josephson effect. *Phys. Rev. Lett.*, vol. 22, no. 25, pp. 1364–1366, June 1969.

[2] Rossat-Mignod, J., Regnault, L., Vettier, C., Burlet, P., Henry, J. and Lapertot, G.: Investigation of the spin dynamics in YBCO by inelastic neutron scattering. *Physica B*, vol. 169, no. 1, pp. 58–65, February 1991.

[3] Clearfield, A., Reibenspies, J. and Bhuvanesh, N.: *Principles and Applications of Powder Diffraction*. John Wiley & Sons, 2008.

[4] Xie, X., Chung, H., Sow, C. and Wee, A.: Nanoscale materials pattering and engineering by atomic force microscopy nanolithography. *Materials Science and Engineering*, vol. R54, pp. 1–48, 2006.

[5] Barone, A. and Paterno, G.: *Physics and Applications of the Josephson effect*. John wiley & Sons, 1982.

[6] Josephson, B.D.: Possible new effects in superconductive tunneling. *Physics Letters*, vol. 1, pp. 251–253, July 1962.

[7] Anderson, P.W. and Rowell, J.M.: Probable observation of the Josephson superconducting tunneling effect. *Phys. Rev. Lett.*, vol. 10, no. 6, pp. 230–232, 1963.

[8] Perold, W.J., Jeffery, M., Wang, Z. and Duzer, T.V.: Complementary Output Switching Logic-A new superconducting voltage-state logic family. *IEEE Transactions on Applied Superconductivity*, vol. 6, no. 3, pp. 125–131, 1996.

[9] Likharev, K.K. and Semenov, V.K.: RSFQ Logic/Memory Family: A new Josephson-junction technology for sub-Terahertz-clock-frequency digital systems. *IEEE Transactions on Applied Superconductivity*, vol. 1, no. 1, pp. 3–28, 1991.

[10] Chen, W., Rylyakov, A.V., Patel, V., E, J. and Likharev, K.K.: Rapid Single Flux Quantum T-Flip Flop operating up to 770 GHz. *IEEE Transactions on Applied Superconductivity*, vol. 9, no. 2, pp. 3212–3215, 1999.

[11] Wu, C., Chou, Y., Kuo, W., Chen, J., Wang, L., Chen, J., Chen, K., Sou, U., Yang, H. and Jeng, J.: Fabrication and characterization of high-T_c YBaCuO NanoSQUIDs made by focused ion beam milling. *Nanotechnology*, vol. 19, pp. 315304–1–5, June 2008.

[12] Lee, S., Oh, S., Kang, C. and Kim, S.: Superconducting nanobridge made from YBCO film by using focused ion beam. *Physica C: Superconductivity and its Applications*, vol. 460-462, no. 2, pp. 1468–1469, September 2007.

[13] Wendt, J., Martens, J., Ashby, C., Hietala, T. and Tigges, C.: YBaCuO nanobridges fabricated by direct-write electron beam lithography. *App. Phys. Lett.*, vol. 61, no. 13, pp. 1597–1599, September 1992.

[14] Irmer, B., Blick, R., Simmel, F., Godel, W., Lorenz, H. and Kotthaus, J.: Josephson junctions defined by a nanoplough. *App. Phys. Lett.*, vol. 73, no. 14, pp. 2051–2053, October 1998.

[15] Gregor, M., Plecenik, A., Plecenik, T., Tomasek, M., Kus, P., Micunek, R., Stefecka, M., Zahoran, M., Grancic, B., Kubinec, M. and Gasparik, V.: Preparation of variable-thickness MgB_2 thin film bridges by AFM nanolithography. *Physica C*, vol. 435, pp. 82–86, 2006.

[16] Feynman, R.P., Leighton, R.B. and Sands, M.: *The Feynman Lectures on Physics.* Addison-Wesley, Reading, MA, 1963.

[17] Orlando, T.P. and Delin, K.A.: *Foundations of Applied Superconductivity.* Addison-Wesley, 1991.

[18] Ambergaokar, V. and Baratoff, A.: Tunneling between superconductors. *Phys. Rev. Lett.*, vol. 10, pp. 486–489, 1963.

[19] McCumber, D.E.: Effect of ac impedance on dc voltage-current characteristics of superconductor weak-link junctions. *J. Appl. Phys.*, vol. 39, pp. 3113–3118, July 1968.

[20] Stewart, W.C.: Current-voltage characteristics of Josephson junctions. *Appl. Phys. Lett.*, vol. 12, pp. 277–280, April 1968.

[21] Van Duzer, T. and Turner, C.W.: *Principles of Superconductive Devices and Circuits.* Prentice Hall PTR, 1999.

[22] Shapiro, S., Janus, A. and Holly, S.: Effect of microwaves on Josephson currents in superconducting tunneling. *Phys. Rev. Lett.*, vol. 36, pp. 223–225, 1964.

[23] Tinkham, M.: *Introduction to Superconductivity.* McGraw-Hill, Inc., 1996.

[24] Kaplunenko, V. and Borzenets, V.: Timing jitter measurement in a circular Josephson transmission Line. *IEEE Transactions on Applied Superconductivity*, vol. 11, pp. 288–291, 2001.

[25] Gross, R., Alff, L., Beck, A., Froelich, O., Koelle, D. and Marx, A.: Physics and Technology of High Temperature Superconducting Josephson junctions. *IEEE Transactions on Applied Superconductivity*, vol. 7, no. 2, pp. 2929–2934, 1997.

[26] Khare, N.: *Handbook of High-Temperature Superconductor Electronics.* Marcel Dekker, 2003.

[27] Daly, K., Dozier, W., Burch, J. and Simon, R.: Substrate step-edge YBCO rf SQUIDs. *Appl. Phys. Lett.*, vol. 58, pp. 543–545, 1991.

[28] van Staden, W.F.: *The Fabrication of PBCO Buffered Step-edge Josephson Junctions.* Master's thesis, Electronic Engineering, University of Stellenbosch, Stellenbosch, South Africa, 2006.

[29] de Villiers, H.A.C.: *A Process for the Manufacture of High Temperature Bi-epitaxial Josephson Junctions.* Master's thesis, Electronic Engineering, University of Stellenbosch, Stellenbosch, South Africa, 2006.

[30] Yanson, I.K., Svistunov, V.M. and Dmitrenko, I.M.: Experimental observation of the tunnel effect for Cooper pairs with the emission of photons. *Sov. Phys. JETP*, vol. 21, pp. 650–653, 1965.

[31] Shapiro, S.: Josephson currents in superconducting tunneling: The effect of microwaves and other observations. *Phys. Rev. Lett.*, vol. 11, pp. 80–82, 1963.

[32] Likharev, K.K.: *Dynamics of Josephson Junctions and Circuits*. Gordon and Breach Science Publishers, 1986.

[33] Likharev, K.K.: Superconducting weak link. *Review Modern Physics*, vol. 51, no. 1, pp. 101–159, 1979.

[34] Yoshihisa, S. and Yoichi, O.: Magnetic Field Modulation of Critical Currents in YBaCuO Co-planar Josephson Junctions using Focused Ion Beam. *IEEE Transactions on Applied Superconductivity*, vol. 7, no. 2, pp. 2311–2314, June 1997.

[35] Shiga, H., Soutome, Y. and Okabe, Y.: Fabrication of YBaCuO Junctions by the Irradiation of Focused Ion Beam. *IEEE Transactions on Applied Superconductivity*, vol. 9, no. 2, pp. 2890–2893, June 1999.

[36] Anderson, P.W. and Dayem, A.H.: Radio-frequency effects in superconducting thin film bridges. *Phys. Rev. Lett.*, vol. 13, pp. 195–197, June 1964.

[37] Aslamazov, L.G. and Larkin, A.I.: Josephson effect in superconducting point contacts. *JETP Lett.*, vol. 9, pp. 87–91, 1969.

[38] Yamashita, T., Kawakami, A., Noge, S., Xu, W., Takata, M., Komatsu, T. and Matusita, K.: Grain Boundary Josephson Devices by YBaCuO Films and $77K$ Operations. *IEEE Transactions on Magnetics*, vol. 25, no. 2, pp. 923–926, 1989.

[39] Kita, S., Tanabe, H. and Kobayashi, T.: Millimeter-wave detection by GBJJ using high-T_c superconducting YBaCuO films. *IEEE Transactions on Magnetics*, vol. 25, no. 2, pp. 907–910, 1989.

[40] Changhyun, C., Joongshik, S., Doosup, H., Youngkeun, K., Youngjong, L. and John, S.: Microwave response of YBaCuO grain boundary junction. *J. App. Phys.*, vol. 77, no. 5, pp. 2193–2195, March 1995.

[41] Hauser, B., Klopman, B., Gao, J. and Rogalla, H.: Response of YBaCuO thin-film microbridges to microwave irradiation. *App. Phys. Lett.*, vol. 54, no. 14, pp. 1368–1370, April 1989.

[42] Hauser, B., Klopman, B., Blank, D. and Rogalla, H.: Properties of lift-off structured high T_c microbridges. *IEEE Transactions on Magnetics*, vol. 25, no. 2, pp. 919–922, March 1989.

[43] Golovashkin, A.I., Gudkov, A.L., Krasnosvobodtsev, S.I., Kuzmin, L.S., Likharev, K.K., Maslennikov, Y.V., Pashkin, Y.A. and Pechen, E.V.: Josephson Effect and Macroscopic Quantum Interference in High-T_c Superconducting Thin-film Weak Link at $77K$. *IEEE Transactions on Magnetics*, vol. 25, no. 2, pp. 943–945, March 1989.

[44] Wiener-Avnear, E., Cooper, J.E., Kerber, G.L., Spargo, J.W. and Toth, A.G.: Laser Patterning of YBaCuO Weak Link Bridges. *IEEE Transactions on Magnetics*, vol. 25, no. 2, pp. 935–938, March 1989.

[45] Gijs, M.A. and Jansen, R.J.: Microwave response of YBaCuO thin-film Dayem bridges. *Appl. Phys. Lett.*, vol. 56, no. 15, pp. 1484–1486, April 1990.

[46] Buttner, U., Hardie, G., Rossouw, R., Srinivasu, V. and Perold, W.: Fabrication of submicron YBCO Josephson junctions by a sample mosaic navigation assisted laser etching process. *Supercond. Sci. Technol.*, vol. 20, pp. S426–S429, October 2007.

[47] Malisa, A., Valkeapaa, M., Johansson, L. and Ivanov, Z.: Josephson effects in magnesium diboride based Josephson junctions. *Supercond. Sci. Technol.*, vol. 17, pp. S345–S349, April 2004.

[48] Hollkott, J., Hu, S., Becker, C., Auge, J., Spangenberg, B. and Kurz, H.: Josephson junctions fabricated by oxygen ion irradiation of YBaCuO thin films. *IEEE Transactions on Applied Superconductivity*, vol. 7, no. 2, pp. 3674–3677, June 1997.

[49] Kahlmann, F., Engelhardt, A., Schubert, J., Zander, W. and Buchal, C.: Properties of SNS Josephson Junctions Fabricated by 200 KeV Oxygen Implantation into YBaCuO. *IEEE Transactions on Applied Superconductivity*, vol. 9, no. 2, pp. 2874–2877, June 1999.

[50] Tolpygo, S., Shokhor, S., Nadgorny, B., Lin, J. and Gurvitch, M.: Normal-state Properties and Josephson Effects in HTS Weak Links produced by Electron Beam. *IEEE Transactions on Applied Superconductivity*, vol. 5, no. 2, pp. 2521–2526, June 1995.

[51] Kim, S. and Yamashita, T.: Focused Electron Beam Damaged YBCO Josephson Junctions for THz Device Applications. *IEEE Transactions on Applied Superconductivity*, vol. 9, no. 2, pp. 4221–4224, June 1999.

[52] Lathrop, D.K., Russek, S.E., Moeckly, B.H., Chamberlain, D., Pesenson, L., Buhrman, R.A., Shin, D.H. and Silcox, J.: Josephson-like Properties of YBaCuO Thin Film Weak Links. *IEEE Transactions on Magnetics*, vol. 27, no. 2, pp. 3203–3208, March 1991.

[53] Kimura, H., Miyazaki, M., Tsuda, K. and Okabe, Y.: Characteristics of Josephson Junctions Using The Crack in YBCO Thin Films. *IEEE Transactions on Applied Superconductivity*, vol. 3, no. 1, pp. 2413–2416, March 1993.

[54] Sheahen, T.P.: *Introduction to High-Temperature Superconductivity.* Kluwer Academic Publishers, 2002.

[55] Schrieffer, J.R.: *Handbook of High-Temperature Superconductivity.* Springer, 2007.

[56] Likharev, K.K.: Vortex Motion and the Josephson Effect in superconducting Thin Film Bridges. *Sov. Phys. JETP*, vol. 34, no. 4, pp. 906–912, April 1972.

[57] Aslamazov, L.G. and Larkin, A.I.: Josephson effect in wide superconducting bridges. *Sov. Phys. JETP*, vol. 41, no. 2, pp. 381–386, February 1975.

[58] Gubankov, V.N., Koshelets, V.P., Likharev, K.K. and Ovsyannikov, G.A.: Coherent Motion of Vortices in Superconducting Bridges of Large Dimensions. *Sov. Phys. JETP*, vol. 18, no. 5, pp. 292–295, September 1973.

[59] Gubankov, V.N., Koshelets, V.P. and Ovsyannikov, G.A.: Coherent effects in Superconducting Bridges of Variable Thickness. *Sov. Phys. JETP*, vol. 44, no. 1, pp. 181–186, July 1976.

[60] Yeh, J.T. and Buhrman, R.A.: Superconducting lead variable-thickness microbridges. *J. Appl. Phys.*, vol. 48, no. 12, pp. 5360–5361, December 1977.

[61] Wolf, S.A., Cukaskas, E.J., Rachford, F.J. and Nisenoff, M.: Granular Niobium and High T_c Niobium Nitride Variable Thickness Weak Link SQUIDs. *IEEE Transactions on Magnetics*, vol. Mag-15, no. 1, pp. 595–598, January 1979.

[62] Schwartz, D.B., Mankiewich, P.M., Jain, A.K. and Lukens, J.E.: Microwave Power Spectra of Variable Thickness Sub-Micron Bridges. *IEEE Transactions on Magnetics*, vol. Mag-17, no. 1, pp. 92–94, January 1981.

[63] Bouchiat, V. and Faucher, M.: Josephson junctions and superconducting quantum interference devices made by local oxidation of niobium ultrathin films. *Appl. Phys. Lett.*, vol. 79, no. 1, pp. 123–125, July 2001.

[64] Hahn, C., Matsuyama, T., Merkt, U. and Wiesendanger, R.: Nanofabrication of weak links based on scanning force methods. *Appl. Phys. A*, vol. 62, pp. 289–292, 1996.

[65] Gregor, M., Plecenik, T., Prascak, M., Micunek, R., Kubinec, M., Gasparik, V., Grajcar, M., Kus, P. and Plecenik, A.: MgB_2 radio-frequency superconducting quantum interference device prepared by atomic force microscope lithography. *Appl. Phys. Lett.*, vol. 91, no. 12, pp. 1225021–1225023, September 2007.

[66] Park, C.H., Kobayashi, T. and Goto, T.: Millimeter Wave Response of YBCO Variable-Thickness Bridges. *IEEE Transactions on Applied Superconductivity*, vol. 3, no. 1, pp. 2409–2412, March 1993.

[67] Lee, S., Kang, C.S., Kim, I., Kim, S. and Kim, H.: Single-layer 2nd-order SQUID gradiometer and fabrication of YBaCuO nanobridges as the Josephson elements. *J. of Phys.: Conference Series*, , no. Series 43, pp. 1203–1206, 2006.

[68] Davidson, B.A., Redwing, R.D., Nguyen, T., Ocallaghan, J., Siegal, M. and Phillips, J.: Magnetic Field Sensitivity of Variable Thickness Microbridges in TBCCO, BSCCO, and YBCO. *IEEE Transactions on Applied Superconductivity*, vol. 4, no. 4, pp. 2409–2412, December 1994.

[69] Barholz, K., Kupriyanov, M.Y., Hubner, U., Schmidl, F. and Seidel, P.: An alternative explanation of the *"long-range proximity effect"* in HTS junctions. *Physica C*, vol. 334, pp. 175–184, March 2000.

[70] de Nivelle, M.J., Gerritsma, G.J. and Rogalla, H.: Thermally activated coherent vortex motion in YBaCuO thin film microbridges. *Phys. Rev. Lett.*, vol. 70, no. 10, pp. 1525–1528, March 1993.

[71] Abrikosov, A.A.: On the magnetic properties of superconductors of the second group. *Sov. Phys. JETP*, vol. 5, pp. 1174–1182, 1957.

[72] Schneider, J., Muck, M. and Wordenweber, R.: DC SQUIDs based upon YBaCuO nanobridges. *Appl. Phys. Lett.*, vol. 65, no. 19, pp. 2475–2477, 1994.

[73] Faucher, M., Fournier, T., Pannetier, B., Thirion, C., Wernsdorfer, W., Villegier, J. and Bouchiat, V.: Niobium and niobium nitride SQUIDs based on anodized nanobridges made with an atomic force microscope . *Physica C*, vol. 368, pp. 2475–2477, 2002.

[74] Lam, S.K. and Tilbrook, D.L.: Development of a niobium nanosuperconducting quantum interference device for the detection of small spin populations. *App. Phys. Lett.*, vol. 82, no. 7, pp. 1078–1080, 2003.

[75] Schneider, J., Hart, A. and Wordenweber, R.: Superconducting flux-flow transistors based upon YbaCuO nanobridges. *IEEE Transactions on Applied Superconductivity*, vol. 5, no. 2, pp. 3393–3396, 1995.

[76] Blank, D.H., Booij, W., Hilgenkamp, H., Vulink, B., d Veldhuis and Rogalla, H.: YBaCuO nano-bridge junctions and dc SQUIDs made by focused ion beam milling. *IEEE Transactions on Applied Superconductivity*, vol. 5, no. 2, pp. 2786–2789, 1995.

[77] Mourachkine, A.: *High-Temperature Superconductivity in Cuprates*. Kluwer Academic Publishers, 2002.

[78] Wu, M., Ashburn, J., Torng, C., Hor, P., Meng, R., Gao, L., Huang, Z., Wng, Y. and Chu, C.: Superconductivity at 93 K in a new mixed-phase Y-Ba-Cu-O compound system at ambient pressure. *Phys. Rev. Lett.*, vol. 58, no. 9, pp. 908–910, 1987.

[79] Wasa, K., Kitabatake, M. and Adachi, H.: *Thin Film Materials Technology*. William Andrew Publishing, 2004.

[80] Smith, D.: *Thin Films Deposition: Principles and Practice*. McGraw Hill, 1995.

[81] Ohring, M.: *The Materials Science of Thin Films*. Academic Press, 1992.

[82] Markov, I.V.: *Crystal Growth for Beginners*. World Scientific, 1994.

[83] Philips, J.M.: Substate selection for high-temperature superconducting thin films. *Journal of Applied Physics*, vol. 79, no. 4, pp. 1829–1848, February 1996.

[84] Wang, L., Yu, H., Yang, H. and Horng, H.: Optimum sputtering conditions on the in-situ growth of superconducting YBCO films with an off-axis RF sputtering configuration. *Physica C*, vol. 256, pp. 57–63, 1996.

[85] Avci, I., Tepe, M. and Abukay, D.: Effect of deposition conditions on YBCO thin films by inverted cylindrical magnetron sputtering and substrate effects. *Solid State communications*, vol. 130, pp. 357–361, 2004.

[86] Wellstood, F., Kingston, J. and Clarke, J.: Thin-film multilayer interconnect technology for YBCO. *J. Appl. Phys.*, vol. 75, pp. 683–702, 1994.

[87] Eidelloth, W., Oh, B., Robertazzi, P., Gallagher, W. and Koch, R.: YBCO thin-film gradiometers: Fabrication and performance. *Appl. Phys. Lett.*, vol. 59, no. 26, pp. 3473–3475, 1991.

[88] Kamm, F., Plettl, A. and Ziemann, P.: Superconducting YBCO nanobridges prepared by a self-limiting wet chemical etching process. *Supercond. Sci. Technol.*, vol. 11, pp. 1397–1400, 1998.

[89] Graser, F.W.: *A Reproducible Design and Manufacturing Process for SQUID Magnetometers*. Master's thesis, Electronic Engineering, University of Stellenbosch, Stellenbosch, South Africa, 2005.

[90] Binnig, G., Quate, C. and Gerber, C.: Atomic force microscope. *Phys. Rev. Lett.*, vol. 56, pp. 930–933, 1986.

[91] Bottomley, L., Coury, J. and First, P.: Scanning probe microscopy. *Analytical Chemistry*, vol. 68, no. 12, pp. 185–230, 1996.

[92] Giessibl, F.: Advances atomic force microscopy. *Rev. Mod. Phys.*, vol. 75, no. 3, pp. 949–983, 2003.

[93] Wendel, M., Irmer, B., Cortes, J., Kaiser, R., Lorenz, H., Kotthaus, J. and Lorke, A.: Nanolithography with an atomic force microscope. *Superlattices and Microstructures*, vol. 20, no. 3, pp. 349–356, 1996.

[94] Nyffenegger, R. and Penner, R.: Nanometer-scale Surface Modification Using the Scanning Probe Microscope: Progress since 1991. *Chem. Rev.*, vol. 97, pp. 1195–1230, 1997.

[95] Song, I., Kim, B. and Park, G.: Fabrication of a Josephson junction using an atomic force microscope. *Appl. Phys. Lett.*, vol. 76, no. 5, pp. 601–603, 2000.

[96] Yamamoto, S., Kawaguchi, A. and Oda, S.: Anomalous current-voltage characteristics along the c-axis in YBCO thin films prepared by MOCVD and AFM lithography. *Physica C*, vol. 293, pp. 244–248, 1997.

[97] Du, J., Gnanarajan, S. and Bendavid, A.: Influence of MgO surface conditions on the in-plane crystal orientation and critical current density of epitaxial YBCO films. *Physica C*, vol. 400, pp. 143–152, 2004.

[98] Ekin, J. and Clickner, C.: Oxygen Annealing of Ex-Situ YBCO/Ag thin-film interface. *IEEE Transactions on Applied Superconductivity*, vol. 5, no. 2, pp. 2400–2403, 1995.

[99] Born, D.: Fabrication of high-Tc microbridges. Personal conversation, Email: `mail@d-born.de,asc08@d-born.de,Phone:39-339-490-0519`, August 2008.

[100] Conductus: *Mr. SQUID User's Guide.* Conductus INc, 969 West Maude Avenue, Sunnyvale, California, USA, 1992.

[101] Fistul, M. and Giuliani, G.: Theory of finite-size effects and vortex penetration in small Josephson junctions. *Phy. Rev. B*, vol. 51, no. 2, pp. 1090–1095, 1995.

[102] Pompeo, N., Muzzi, L., Galluzzi, V., Marcon, R. and Silva, E.: Measurements and removal of substrate effects on the microwave surface impedance of YBCO films on $SrTiO_3$. *Supercond. Sci. Technol.*, vol. 20, no. 10, pp. 1002–1008, 2007.

[103] Aslamazov, L.G. and Larkin, A.I.: Superconducting contacts with nonequilibrium electron distribution function. *Sov. Phys. JETP*, vol. 43, pp. 698–703, 1976.

[104] Kupriyanov, M., Likharev, K. and Maslova, L.: The Js(φ) relationship, Abrikosov vortices, and Josephson vortices in variable thickness bridges. *LT 14*, vol. 4, pp. 104–107, July 1975.

[105] Li, Z., Xuan, Y., Tao, H., Luo, P., Ren, Z., che, G., Zhao, B. and Zhao, Z.: Josephson tunneling in MgB_2 break junctions. *Physica C*, vol. 370, pp. 1–5, 2002.

[106] Hilgenkamp, H., Mannhart, J. and Mayer, B.: Implications of symmetry $d_{x^2-y^2}$ and faceting for the transport properties of grain boundaries in high-Tc superconductors. *Phys. Rev. B*, vol. 53, no. 21, pp. 14586–14593, June 1996.

[107] Eisenmenger, J., Kamm, F., Plettl, A. and Ziemann, P.: Matching in YBCO nanobridges due to surface barrier effects. *Physica C*, vol. 411, pp. 136–142, 2004.

[108] Monaco, R., Aaroe, M. and Mygind, J.: Magnetic Field Modulation of Critical Currents in YBaCuO Co-planar Josephson Junctions using Focused Ion Beam. *Journal of Applied Physics*, vol. 102, no. 093911, pp. 093911–1–093911–4, June 2007.

Appendix A

ICM Operation Procedure

- Close the valves of the roughing and diffusion pumps. Then vent the chamber.
- Remove all the cables on ICM head and put it a side.
- Make sure the heater is mounted on the water cooled based. Center the heater to yield better film uniformity.
- Place silver paste on top of the heater element.
- Load the substrate on the heater and apply slight pressure to the sample edges so that the silver paste covers all the substrate underneath.
- Place ICM head ontop of the deposition chamber.
- Wait for 5 minutes for the silver to dry.
- Close the side valves on the argon and oxygen gas cylinders and open the gas inlet valves on the workbench.
- Turn the roughing pump valve to roughing. Wait for the background pressure to reach desire value. This should take about 40 minutes if no vacuum leaks exist on the system.
- Close the gas inlet valves on the workbench and open the valves at the gas cyliners.
- Open the argon inlet valve on the bench and adjust the gas pressure to 150 . Wait for the pressure to stabilize.
- Close the argon inlet valve and open the oxygen inlet valve. Adjust the oxygen pressure to 150 .
- Open both inlet valves and the total pressure in the system will be around 220 .
- Set your deposition profile (temperatures and durations) by the temperature controller.

- Switch on the water cooling to the magnets and heater while checking that there are no water leaks.
- connect the negative terminal of the sputtering power supply to the ICM cathode and the positive terminal to the ICM anode. Connect the anode to the ground.
- When the temperature reaches to the deposition temperature, switch on the power supply to deliver 400 mA.
- After a suitable amount of deposition time, switch off the power supply.
- Close the argon gas inlet valve on the workbench and the valves at the argon cylinder.
- During the cooling down, increase the oxygen flow into the chamber slowly by adjusting the oxygen inlet valve.
- At 460 the annealing process will commence. Close the roughing pump valve. The chamber pressure should now be around 1 bar.
- After following a desired anneal profile, wait for the temperatrue to cool down below 100 .
- Remove all cable connections from ICM and remove ICM head.
- Remove the sample with a sharp scalpel. Make sure to remove the sample without breaking it.
- Place the ICM head again and turn on the roughing pump.
- Switch off the water cooling pump. keep the chamber under vacuum.

Appendix B

Supplementary Results

The appendix shows extra results, such as the Josephson effect, critical current versus temperature, and magnetic field effects on critical current on different weak link stuctures, fabricated using AFM nanolithography.

B.1 Josephson Effect in Micro-Bridges

A micro-bridge, with a width of 2.8 μm, fabricated on a YBCO track with a thickness of 110 nm, is shown below.

The critical current versus temperature response of the bridge shows a quasi-linear behaviour. This behaviour is typical for S-$\acute{S}$-S structures.

The bridge responded well to the applied RF signal. We observed Shapiro steps on the I-V curve. As the RF power increased, the critcal current was reduced, and current spikes at constant voltage steps became more clear on the I-V curve.

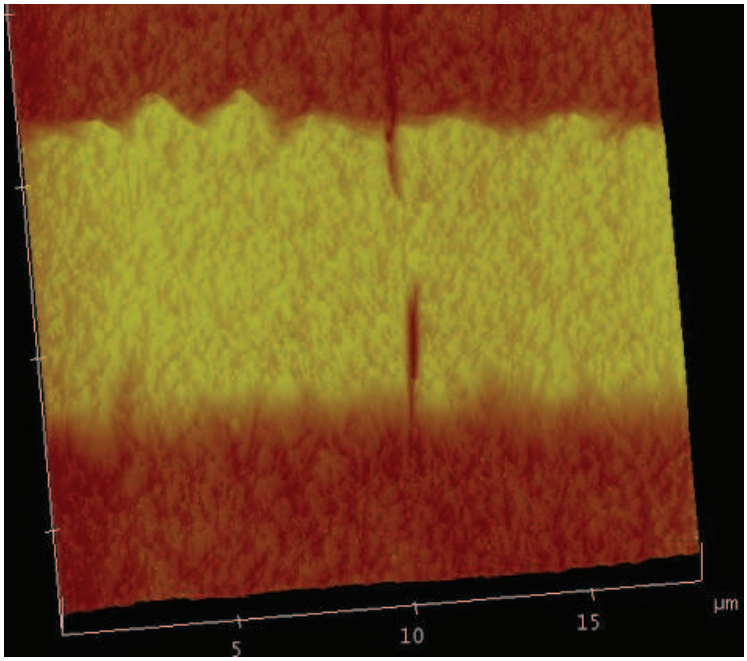

Figure B.1: AFM image of a 2.8 μm width micro-bridge junction.

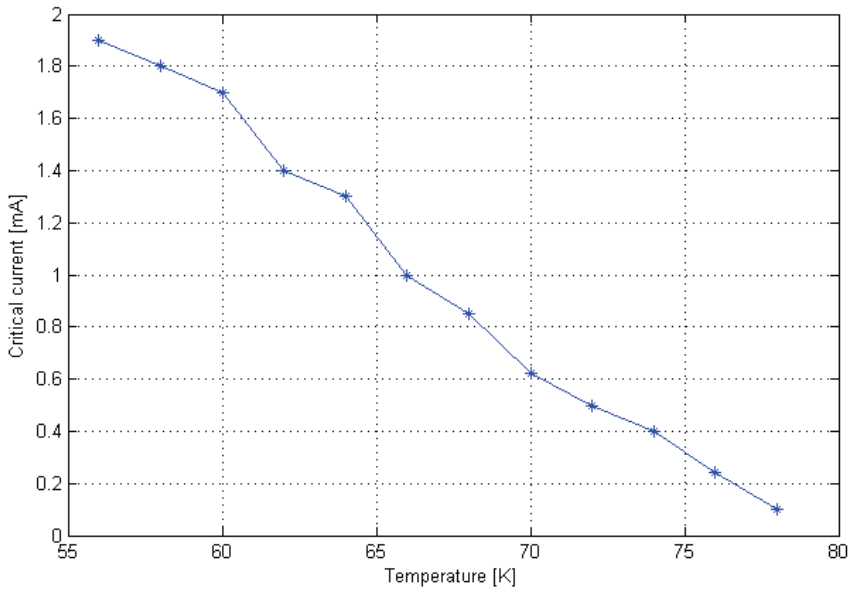

Figure B.2: Measured I_c versus temperature relationship of the 2.8 μm width microbridge.

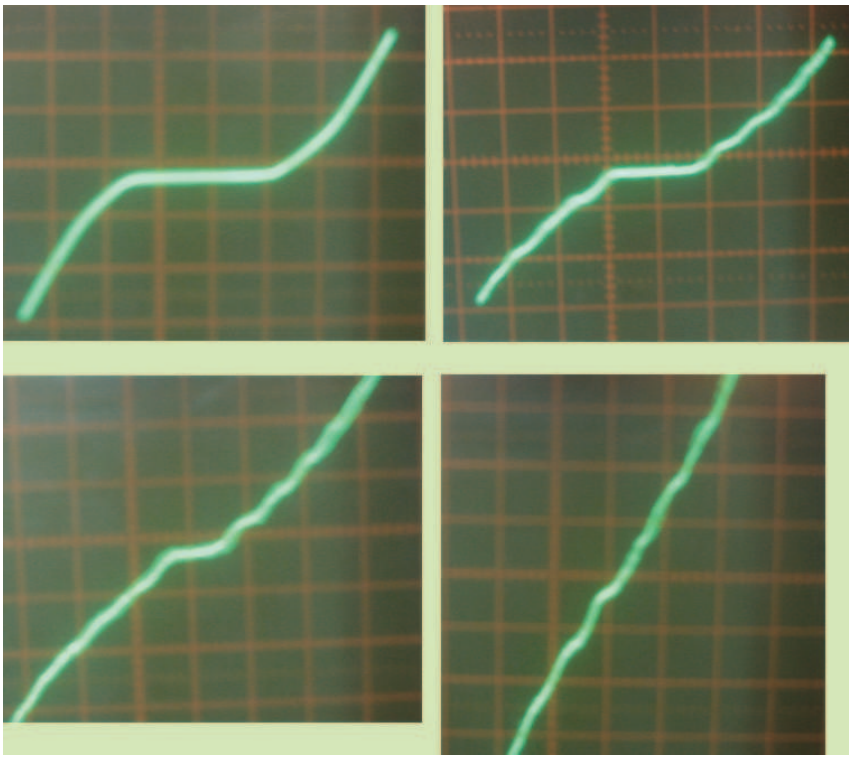

Figure B.3: Measured I-V curve for the 2.8 μm width micro-bridge without (top left), and with an applied microwave signal at different power levels.

B.2 Magnetic Field Effect on Micro-Bridge

This measurement was done on another micro-bridge with a width of 3.2 μm.

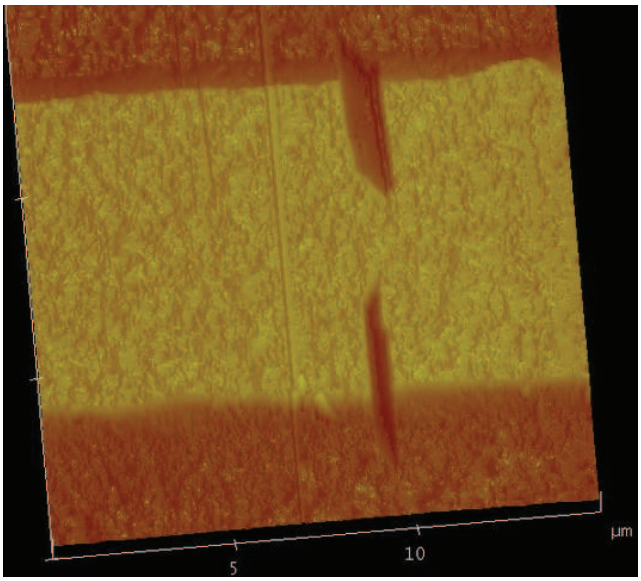

Figure B.4: AFM image of a 3.2 μm width micro-bridge.

The junction has a critical current of 2.4 mA at 57 K.

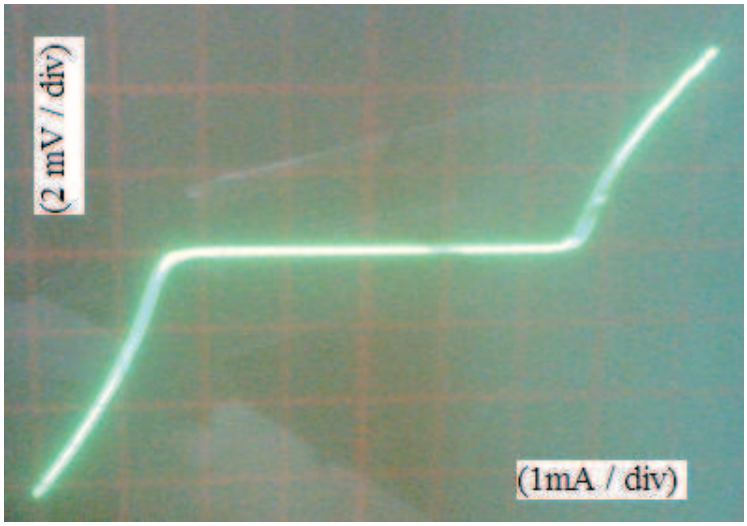

Figure B.5: Measured I-V curve for the 3.2 μm width micro-bridge at 57 K.

The critical current versus temperature shows quasi-linear behaviour near T_c.

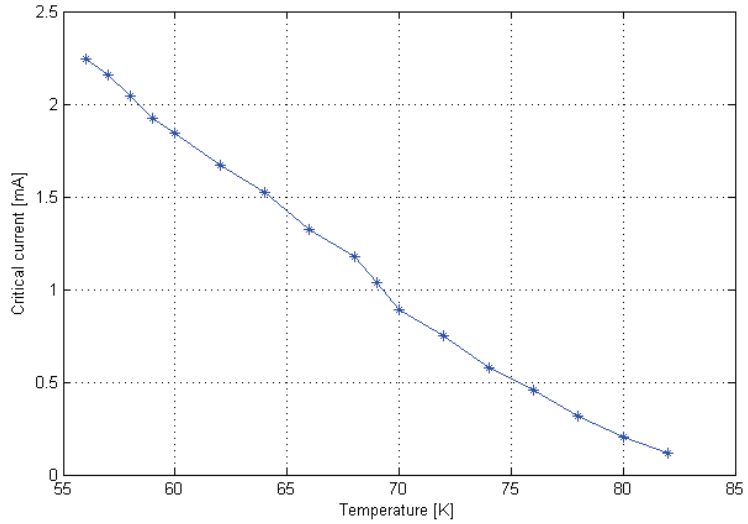

Figure B.6: Measured I_c versus temperature relationship for the 3.2 μm width micro-bridge.

The external magnetic fields modulated and suppressed the critical current of the junction.

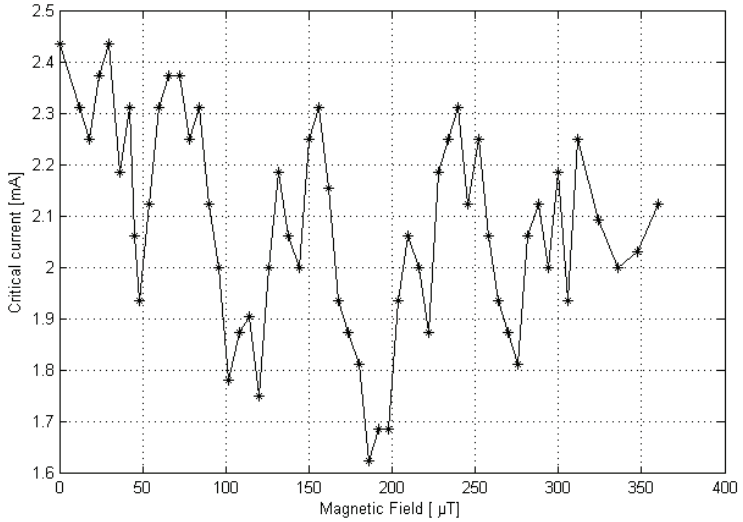

Figure B.7: Measured magnetic field modulation of the critical current in the 3.2 μm width micro-bridge.

B.3 Magnetic field modulation I_c in Variable Thickness Bridge

These measured results were performed on a VTB bridge with a thickness of 37-49 nm.

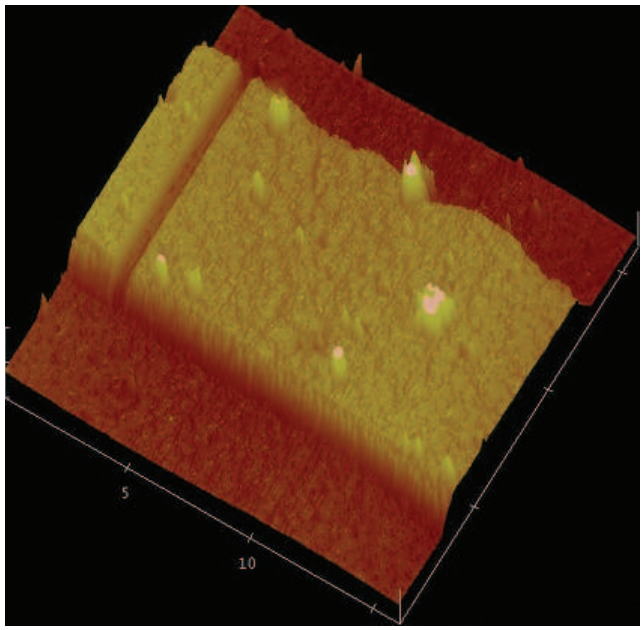

Figure B.8: AFM image of a 37 - 49 nm thickness VTB bridge.

The I_c versus T curve shows a quasi-linear response.

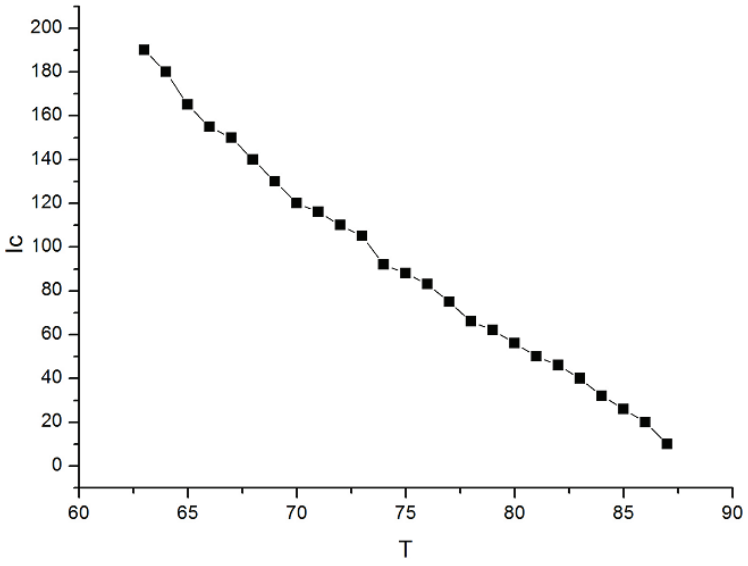

Figure B.9: Measured I_c versus temperature relationship for the 37 - 49 nm thickness VTB bridge.

The VTB bridge has a critical current of 170 μA at 65 K.

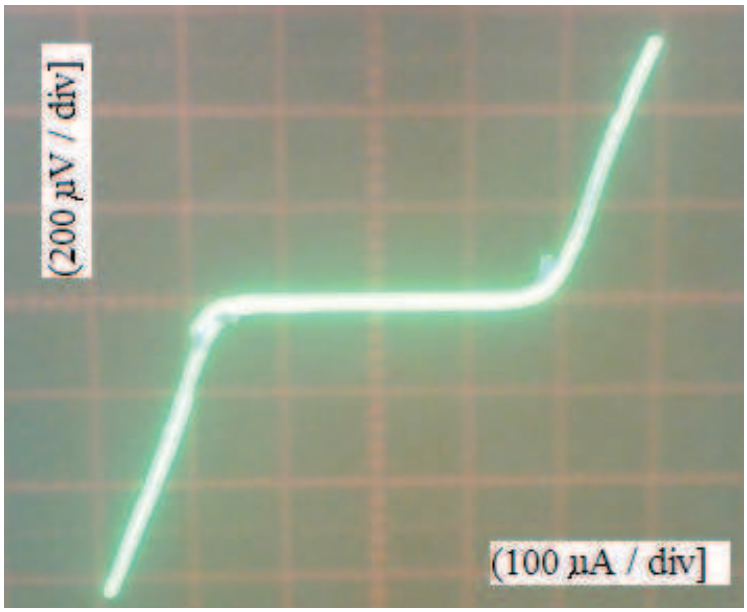

Figure B.10: Measured I-V curve for the 37 - 49 nm thickness VTB bridge at 65 K.

Modulation and suppression of the critical current in the presence of external magnetic fields were observed. However, it deviates from the ideal Fraunhofer-like diffraction pattern.

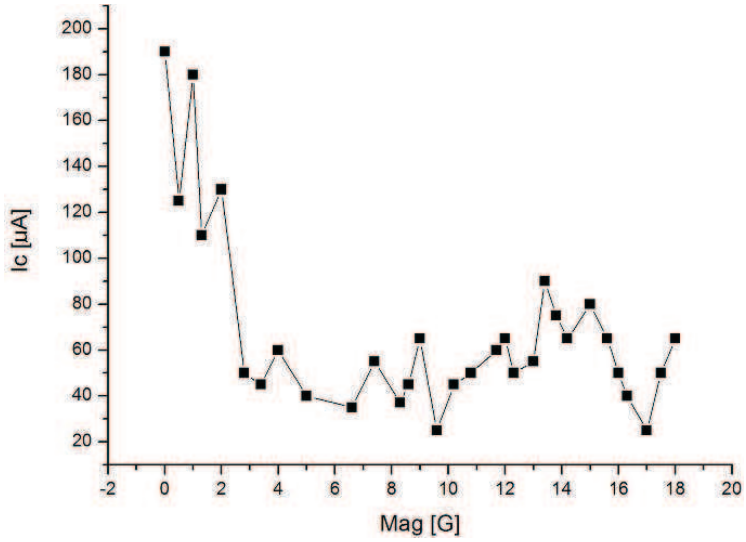

Figure B.11: Measured magnetic field modulation of the critical current in the 37 - 49 nm thickness VTB bridge.

B.4 Destroyed Bridges

We lost many planar stuctures during the test, most of them became open-circuit. The AFM image below shows two bridges before and after they have been tested.

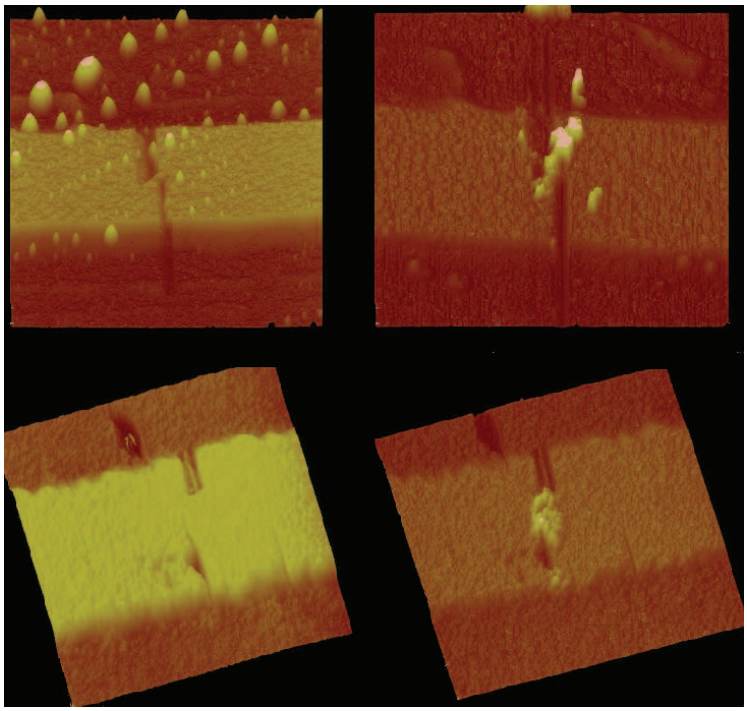

Figure B.12: AFM images of destroyed micro-bridges. The image on the left was taken before the test, and the one on the right afterwards.

B.5 Calculating the Tip Loading Force

Given the spring constant, K, of the cantilever (37-59 N/m in our case), the contact force is defined by the cantilever spring equation $F = K(\Delta Z)$, where ΔZ is the Z distance from the control point to V_{CSmin} in nanometers.

First the deflation sensitivity is determined on a hard metal. Thereafter, the value of the deflation sensitivity is entered into the system.

For a spring constant of 53 N/m, and ΔZ taken from the image below (207 nm), the loading force of the tip can be calculated to be ≈ 11 μN.

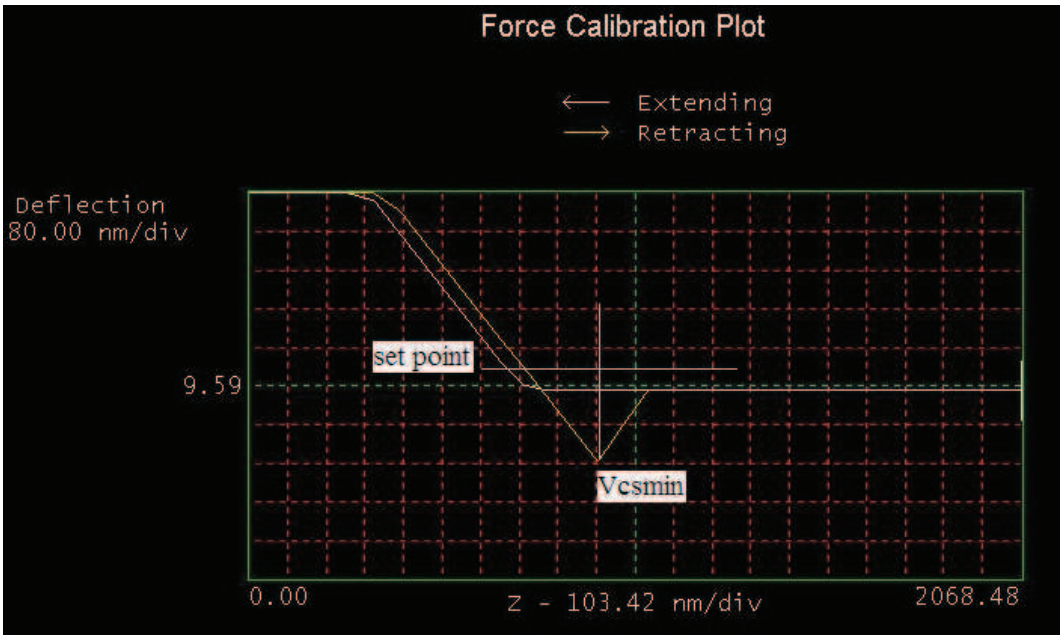

Figure B.13: Force measurement curve.

AFM Nanolithography Program Example

```
// diamond.cpp
// Example #1 - Writing a Lithography Program

#include <litho.h>

extern "C" __declspec(dllexport) int macroMain()
{
        LITHO_BEGIN

        LithoDisplayStatusBox();      // display litho status box

        LithoScan(false);             // turn off scanning
        LithoCenterXY();              // move tip to center of field

        double size = 10;             // 10 um from center of diamond to point
        double rate = 20;             // move the tip in X-Y at 20 um/s

        double depth = -0.020;        // push the tip in 20 nm to draw lines
        double z_rate = 0.040;        // move the tip down at 40 nm/s

        // move to left side of the line.
        LithoTranslate( size, 0, rate);      // move the tip 10 um in X-direction

        // push tip into surface
        LithoMoveZ(depth, z_rate);   // moving in Z turns off feedback

        // scribe four sides of the diamond
        LithoTranslate(0, size, rate);       // move the tip 10 um in Y-direction
        LithoTranslate(0, -size, rate);      // move the tip -10 um in Y-direction
        LithoTranslate(0, -size, rate);      // move the tip 10 um in Y-direction
        LithoTranslate( 0, size, rate);      // move the tip -10 um in Y-direction

        LITHO_END

        return 0;        // 0 makes the macro unload. Return 1 to keep the macro loaded.
```

Figure B.14: Example of AFM the nanolithography program.

Appendix C

Research Contributions and Publications

C.1 Publications

1. Elkaseh, A.A.O., Srinivasu, V.V. and Perold, W.J.: Observation of Shapiro-steps in AFM-plough micron-size YBCO Planar Constrictions, *IEEE Transactions on Applied Superconductivity*, vol. 19, pp. 187-190, 2009.
2. Elkaseh, A.A.O., Srinivasu, V.V. and Perold, W.J.: AFM nano-plough planar YBCO micro-bridges: Critical currents and magnetic field effects, *Journal of Nanoscience and Nanotechnology*, vol. 10, pp. 6510-6513, 2010.
3. Elkaseh, A.A.O., Büttner, U, Srinivasu, V.V. and Perold, W.J.: AFM Plough YBCO Microbridges: Substrate effects, *Proceedings of SACSST 2009* (ISBN 978-0-620-43865-0).
4. Elkaseh, A.A.O., Srinivasu, V.V. and Perold, W.J.: AFM Plough YBCO nano Josephson constrictions, *Journal of Applied Physics*, vol. 108, pp. 053914, 2010.

C.2 Conferences

1. Elkaseh, A.A.O., Büttner, U, Srinivasu, V.V. and Perold, W.J.: Fabrication of Micron and Nano plough constriction type Josephson Junctions using an Atomic Force Microscope, *IEEE Applied Superconductivity Conference*, Chicago, Illinois, 17-22 August 2008.
2. Elkaseh, A.A.O., Perold, W.J. and Srinivasu, V.V.: Critical Currents and Magnetic Field Effects in AFM plough Planar YBCO Microbridges, *NanoAfrica 2009*, Pretoria,

1-4 February 2009.

3. Elkaseh, A.A.O., Perold, W.J. and Srinivasu, V.V.: AFM Plough Variable-Thickness Nanobridges: Josephson effect and critical current density, *NanoAfrica 2009*, Pretoria, 1-4 February 2009.

4. Elkaseh, A.A.O., Büttner, U, Srinivasu, V.V. and Perold, W.J.: AFM Plough YBCO Micro-Bridges: Substrate effects, *South African Conference on Semi- and Superconductor Technology (SACSST2009)*, Stellenbosch, 8-9 April 2009.